Challenges for energy dispersive X-ray absorption spectroscopy at the ESRF: microsecond time resolution and Megabar pressures

Giuliana Aquilanti

To cite this version:

Giuliana Aquilanti. Challenges for energy dispersive X-ray absorption spectroscopy at the ESRF: microsecond time resolution and Megabar pressures. Other [cond-mat.other]. Université de Grenoble, 2002. English. NNT : . tel-00828730

HAL Id: tel-00828730
https://theses.hal.science/tel-00828730

Submitted on 31 May 2013

Challenges for energy dispersive X-ray absorption spectroscopy at the ESRF: microsecond time resolution and Megabar pressures

Giuliana Aquilanti

Thèse
présentée par
Giuliana Aquilanti

Pour obtenir le titre de
Docteur de l'Université Joseph Fourier - Grenoble I

Challenges for energy dispersive X-ray absorption spectroscopy at the ESRF: microsecond time resolution and Megabar pressures

Soutenue le 12 décembre 2002

Composition du jury:

Dr. Alain Fontaine	President du jury
Prof. Settimio Mobilio	Rapporteur
Dr. Jean Paul Itié	Rapporteur
Prof. John Evans	Examinateur
Dr. Jean Louis Hodeau	Examinateur
Dr. José Goulon	Directeur de thèse
Dr. Sakura Pascarelli	Directrice de thèse

Thèse préparée au sein du laboratoire
European Synchrotron Radiation Facility
BP 220 - 38043 Grenoble Cedex - France

Abstract

This Thesis concerns the development of two different applications of energy-dispersive X-ray absorption spectroscopy at the ESRF: time-resolved studies pushed to the microsecond time resolution and high-pressure studies at the limit of the Megabar pressures. The work has been developed in two distinct parts, and the underlying theme has been the exploitation of the capabilities of an X-ray absorption spectrometer in dispersive geometry on a third generation synchrotron source. For time-resolved studies, the study of the triplet excited state following a laser excitation of $Pt_2(P_2O_5H_2)_4{}^{4-}$ has been chosen to push the technique to the microsecond time resolution. In the high-pressure part, the suitability of the energy dispersive X-ray absorption spectrometer for high-pressure studies using diamond anvils cell is stressed. Some technical developments carried out on beamline ID24 are discussed. Finally, the most extensive scientific part concerns a combined X-ray absorption and diffraction study of InAs under pressure.

Résumé

La Thèse s'articule en deux parties distinctes, autour de l'exploitation des caractéristiques exceptionnelles d'une ligne de lumière d'absorption X en géométrie dispersive dans un synchrotron de troisième génération. La première partie décrit la possibilité d'effectuer des études de spectroscopie d'absorption X résolues en temps avec une résolution temporelle de l'ordre de la microseconde. L'étude de la structure de l'état excité du composé $Pt_2(P_2O_5H_2)_4{}^{4-}$ a été choisi pour mettre au point cette technique. Dans la deuxième partie, l'adéquation entre les possibilités offertes par une ligne d'absorption X en dispersion d'énergie et les expériences à très hautes pressions obtenues dans les cellules à enclumes de diamants est mise en évidence. Outre les développements instrumentaux, cette dernière technique est illustrée par une étude combinée par diffraction et par absorption des rayon X du composé InAs sous pression.

Acknowledgements

It is a pleasure for me to thank several people for their essential contributions to the realization of this work.

First of all, I would like to thank Sakura Pascarelli. During the time of this Thesis, she has always been available for guiding me in the scientific and technical tasks. I thank her for having transmitted to me her experience, enthusiasm and ideas, decisive for the accomplishment of this work. I thank her for having taught me an efficient method and way of working. I regret if I was not always able to follow her at her speed! I thank her for her *everytime and everywhere* help. Her corrections and suggestions for the last pages of this manuscript, even at those "extreme conditions", have been very important to me.

I acknowledge José Goulon who has always encouraged my efforts, and for his support during these years.

I acknowledge the two *rapporteurs* whose remarks have tremendously improved the quality of the manuscript: Settimio Mobilio who has shown interest in this work, and Jean Paul Itié for the useful discussions and advises.

I am grateful to Alain Fontaine; I was honoured to have him as the *president du jury*.

Thanks to Jean Louis Hodeau for accepting to be *examinateur* and to John Evans for his comments on the first part of the Thesis.

Thanks to Thomas Neisius with whom I took my first steps on the operation of the beamline and for his helpful advises and ideas on how to improve my work.

I also want to thank Sofía Díaz-Moreno for her time and tenacity during the time-resolved experiments, for her chemistry lectures during these years, especially for the one the day before the defence!

A special thank you goes to the people working on ID24: the engineers Trevor Mairs, Marie-Christine Dominguez and Pierre Pinel. A thought goes to Ralf Weigel for his exceptional contribution to the mysterious business of electronics. A particular

thank you to Sebastien Pasternak for his work on the different sample holders for the time-resolved experiments, for his enthusiasm in preparing high-pressure experiments and for his kindness.

I am grateful to Gloria Subías-Peruga for the EXAFS measurements of $Pt_2(P_2O_5H_2)_4{}^{4-}$ on BM29 during her own in-house-research beam time and to Tristan Le Bihan for the InAs measurements using Nitrogen on ID30. I acknowledge also Bernard Canny for the information about the material of the heated diamond anvil cell.

Un grand merci to my office mate Olivier Mathon for his suggestions on the first part of the manuscript, for his help with the French, and for putting up with me during my "office-cleaning manias" attacks.

Ta to Wilson Crichton for many things: for having taught me everything I know about diffraction except, maybe, for the Bragg's law; for having read the manuscript several times and corrected my English, for his help during the XAS/XRD experiments on ID24, and for his enormous support and patience during the last few weeks before the submission of the manuscript.

I would like to thank Roberto Barocci to whom this work is dedicated.

Finally, I want to thank Sara Susini because during her first days of life allowed her mum to correct the last pages of this manuscript.

List of abbreviations

ADXRD	Angle Dispersive X-Ray Diffraction
BL	Beamline
BPM	Beam Position Monitor
CCD	Charge Coupled Device
DAC	Diamond Anvil Cell
EDXAS	Energy Dispersive X-ray Absorption Spectroscopy
EDXRD	Energy Dispersive X-ray Diffraction
ESRF	European Synchrotron Radiation Facility
EXAFS	Extended X-ray Absorption Fine Structure
FWHM	Full Width at Half Maximum
HP	High-Pressure
HT	High-Temperature
PSD	Position Sensitive Detector
PTM	Pressure Transmitting Medium
RT	Room Temperature
SR	Synchrotron Radiation
TR	Time-Resolved
XAFS	X-ray Absorption Fine Structure
XANES	X-ray Absorption Near Edge Structure
XAS	X-ray Absorption Spectroscopy
XRD	X-Ray Diffraction

Contents

List of Figures

List of Tables

Introduction

The X-ray beam delivered by third generation synchrotron sources is characterized by having high brilliance, a large spectral band, a small source size and divergence, a polarization and a temporal structure. All these properties have allowed research to advance in several scientific domains: physics, chemistry, geology, biology, medicine. Among the experimental techniques that use synchrotron radiation, X-ray absorption spectroscopy has recently experienced a renaissance; undergoing important theoretical and experimental developments over the past three decades also thanks to the increased worldwide availability of synchrotron sources. Besides the conventional scanning X-ray absorption technique, the interest for energy-dispersive X-ray absorption has been growing steadily from the early 80s. Nonetheless, the tantalizing idea of dispersive optics being used to generate the full energy bandpass needed to collect X-ray absorption spectra has been alive for a long time. Indeed, Cauchois [1] has pioneered various aspects of X-ray absorption spectroscopy using this scheme at the end of the 40s.

Historically, energy-dispersive spectrometers were developed for time-resolved studies. The possibility of collecting the data at once makes the dispersive scheme particularly suited for monitoring dynamical processes [2, 3]. Moreover, compared to the conventional point-by-point approach, recording X-ray absorption spectra in a dispersive mode has several features that make this method advantageous for high-pressure studies [4]. In fact, the absence of mechanical movements during the acquisition of the spectra and the focusing properties of the polychromator yield the spot stability and dimensions respectively required for extremely small samples contained in diamond anvil cells. Beamline ID24 is the ESRF's energy-dispersive EXAFS beamline. It is the only beamline of its kind to be installed on an undulator source [5–7], exploiting the high brilliance and flux of a third generation synchrotron source.

This Thesis deals with topical challenges that are currently facing experiments using an energy-dispersive X-ray absorption spectrometer coupled to a third generation synchrotron source in two different scientific domains: time-resolved studies down to

10^{-6} s and high-pressure studies up to 10^6 bars. Therefore, the manuscript is divided in two distinct parts.

Time-resolved studies This first part includes the first three chapters of the Thesis.

Chapter 1 contains an introduction to time-resolved studies using synchrotron radiation. Some examples of time-resolved studies using XAS are reported. A particular emphasis is given to those time-resolved experiments whose goal is to determine the structure of matter in its metastable excited state. We focused on this class of experiments because of the scientific case we chose to assess the microsecond time-resolved XAFS technique using the detection system of ID24.

Chapter 2 illustrates the characteristics of beamline ID24 for time-resolved studies. In particular, the detection system is described together with different acquisition methods. We describe the principle of the synchronization method whose performance is essential for the time resolutions we want to achieve.

Chapter 3 concerns the time-resolved X-ray absorption experiment performed on beamline ID24 on a system of choice: $Pt_2(P_2O_5H_2)_4{}^{4-}$. We underline the experimental requirements for a photoexcitation time-resolved experiment and explain why $Pt_2(P_2O_5H_2)_4{}^{4-}$ is potentially suitable for the investigation of an excited structure using X-ray absorption spectroscopy. We review previous studies on this system using different techniques and in particular an experiment using X-ray absorption spectroscopy performed in 1993 by Thiel *et al.* [8] that determined the structural modifications in $Pt_2(P_2O_5H_2)_4{}^{4-}$ following a laser excitation. We then describe in detail the time-resolved experiment we performed on this system at ID24. We illustrate the result we expected to obtain by simulating the excited state EXAFS signal and report the effective result of our experiment. The result of our experiment was “negative”, in the sense that it is not in agreement with the previous EXAFS experiment nor with our simulations, i.e. we did not observe any structural change on the sample between before and after the excitation. We then summarize further experiments we have performed on $Pt_2(P_2O_5H_2)_4{}^{4-}$ to explain the negative results obtained. A paragraph is devoted to the discussion of the effect of the X-ray beam on $Pt_2(P_2O_5H_2)_4{}^{4-}$. Finally, a discussion and an interpretation of all our experimental evidences are given.

High-pressure studies This part includes the last five chapters of this Thesis.

Chapter 4 is a very general introduction to high-pressure studies.

Chapter 5 surveys some high-pressure apparata. In particular, the diamond anvil cells and related equipment.

In Chapter 6, after a brief review of selected X-ray absorption studies at high-pressure, the following sections all deal with more technical aspects and mainly serve as framework for the topics developed in Chapter 7. We give a brief survey of the most active synchrotron radiation beamlines in high-pressure X-ray absorption spectroscopy. After this introduction, the topic concentrates on high-pressure X-ray absorption spectroscopy using diamond anvil cells, focusing on the main experimental prerequisites necessary for such studies. Finally, the principle of the energy dispersive spectrometer is briefly described (a more complete description is given in Appendix A), pinpointing the advantages of this setup for experiments using diamond anvil cells.

Chapter 7 describes the optical scheme of beamline ID24 and some technical improvements carried out in the last two years. The implementation of the local feedback to damp the motion of the electron beam (described in detail in Appendix B) and of a third vertically refocusing mirror together with the high X-ray brilliance, provided by a third generation source, have opened new opportunities for X-ray absorption spectroscopy at high-pressure. Section 7.2 is devoted to some of these new opportunities whose development has been part of the technical work of this Thesis, mainly:

i. the feasibility tests of X-ray absorption measurements in the low energy domain ($E < 8$ keV) at high-pressure and the application to the scientific case of the study of hematite up to 100 GPa,

ii. the commissioning of a new setup for the combined acquisition of energy-dispersive X-ray absorption spectra and angle-resolved X-ray diffraction patterns at high-pressure,

iii. the commissioning of a new heated diamond anvil cell for high-pressure/high-temperature studies.

Chapter 8 deals with the scientific application developed in the second part of the Thesis and concerns a study of the structural properties of binary compounds $\mathrm{A}^N\mathrm{B}^{(8-N)}$ under pressure. The traditional understanding of the structure and bonding of $A^N B^{(8-N)}$ octet semiconductors and of their behaviour under compression is based on the notion that at the increase of pressure, the low density four-fold coordinated structures are transformed into denser phases of increased coordination: four-fold → six-fold → eight-fold [9]. Based on these expectations, *ab initio* calculations have found the zincblende → NaCl → β-Sn → CsCl transition sequence. However, recent experiments have surprisingly revealed a *systematic absence* of the NaCl/β-Sn phase for the more covalent/ionic compounds [10]. This pattern has been successfully explained in terms of dynamical phonon instabilities of such structures [11]. Using the same methods, recent works predict that the CsCl phase is dynamically unstable for the more ionic III-V semiconductors and suggest candidate structures replacing CsCl [12]. We have examined this prediction for the InAs compound [13–15]. Combining X-ray diffraction and absorption measurements we fully described the high-pressure phases of InAs and thereby obtained the first experimental verification of the inclusion of phonon instability effects in the theoretical description of the high-pressure behaviour of III-V semiconductors. The results of a high-pressure/high-temperature study on InAs using energy-dispersive X-ray diffraction are also reported [16].

Part I

Time-resolved studies

Chapter 1

Why time-resolved experiments?

This chapter introduces the first part of this work, it concerns time-resolved studies. The determination of the structure of matter in its metastable excited state is of crucial importance for the understanding of chemical and biological processes. In chemistry, for example, the problem of the relationship between electronic and molecular structure can be solved by comparing the structure of a single molecule in different electronic states. The development of synchrotron radiation sources offers an important tool for the study of transient phenomena. In particular time-resolved X-ray absorption spectroscopy provides a powerful approach to monitor transient molecular structures in disordered media, as shown by the reported studies.

1.1 Introduction

The phenomena of time and temporal changes have been one of the most fundamental concepts of science from the origins to the modern physics. Temporal changes investigated by scientific methods occur on time scales of more than 30 orders of magnitude, as shown schematically in Figure 1.1 [17]. The study of the kinetics of time-evolving systems has become feasible thanks to the availability of probes that offer both shorter data collection times and the opportunity to apply new experimental techniques. SR, with its unique properties, offers a tool to extend X-ray measurements from the static to the dynamic regime. The most straightforward application of SR to the study of tran-

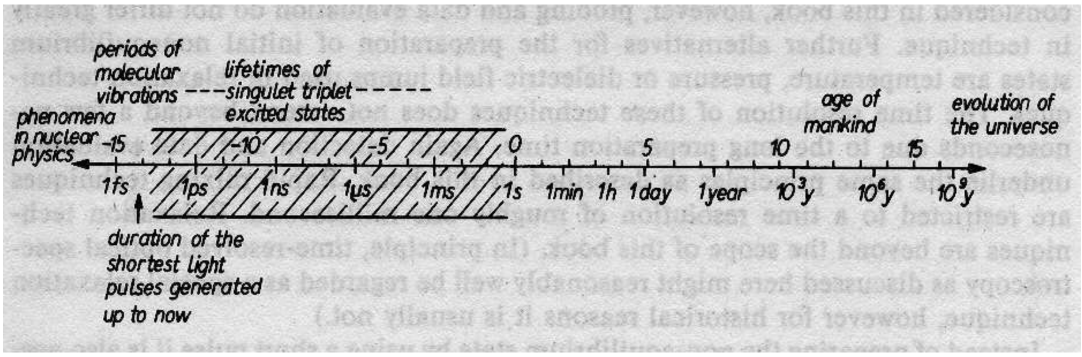

Figure 1.1: Timescale of phenomena investigated by scientific methods.

sient phenomena is directly through the possibility of decreased data collection times via the enormous increase in flux over that available from a laboratory X-ray system. For example, an approach that uses the continuous spectral nature of SR to decrease data collection times is the “parallel data collection” method. Using this method, intensities as a function of X-ray energy are recorded simultaneously for all energies rather than sequentially recording data at each energy, allowing a decrease in data collection time.

All TR experiments use some sort of *pump/probe* technique to investigate the time evolution of transient or short-lived states. The word pump is used in the most general sense and can include mixing, mechanical stressing, thermal excitation, photon excitation, electromagnetic excitation, etc. As the time-scales decrease, the ability to excite the sample both rapidly and uniformly becomes increasingly critical. The time necessary to fully excite the sample can be, in some circumstances, the determining factor in the temporal resolution. To increase the speed and the uniformity with which the sample can be excited, larger pumps and/or small samples are used. The move towards smaller samples puts further demands on the brilliance of the source and the focusing properties of X-ray optics.

TR experiments can be divided into two categories:

i. those experiments involving irreversible processes that must be studied on a one shot basis, and

ii. those experiments involving processes that can be cyclically pumped and hence signal averaged over many excitation periods.

1.2 Reported TR studies using XAS in photochemical reactions

Molecular structures are the bases of understanding photochemical reaction mechanism and molecular reactivity. Although many aspects of photochemistry can be well understood based on the ground state structures, the understanding of the processes often remains incomplete due to unknown structures of transient molecular species such as the excited states. Because many photochemical reactions occur in disordered media, X-ray techniques that do not rely on the long-range order of the structure have been developed for TR studies.

The first TR-XAS measurements with a time resolution of 300 μs were carried out to monitor the recombination of carbon monoxide with myoglobin after laser photolysis. Changes in the pre-edge structure and in the position of the iron edge were detected as a function of time [18]. Although this first work exploited the time structure of SR, transient molecular structures generated by light-induced processes were mainly captured in the past without this peculiarity of SR sources. These include the structural study of a photogenerated electron transfer of cyclopentadienylnitrosylnickel (CpNiNO) produced by a reversible photochemical reaction [19], or the study of structural changes in a Fe(II) complex associated with thermally activated spin state transitions [20].

The development of TR-XAS methods have been relatively slow, due to the difficulties both in finding the chemical systems of interest and in collecting data with the high signal-to-noise ratio necessary for detailed structural analysis. Nevertheless, other studies using TR XAS were published. In the work of Thiel *et al.* [8], the excited state of an inorganic Pt complex was structurally characterized by XAS (see Chapter 3). In a subsequent work, the structure of the initial photoproduct of five-coordinated base-off Co(III) methylcobalamin [21], and the structural change following photoinduced electron transfer within bis-porphyrin heme protein model [22] were determined. More recently, TR XAS techniques have been increasingly exploiting the time structure of SR. A TR EXAFS study with 14 ns resolution was reported at APS (*Advanced Photon Source*, Argonne National Laboratory, Chicago, USA) [23]. In this work Chen *et al.* measured the ligand dissociation of Ni-TPP, a Ni complex with 6 ligands in an octahedral configuration, via Ni K-edge EXAFS, photostimulated by a UV picosecond laser. A change of 18 pm in nearest-neighbour distance was resolved in this photochemical process.

The selection of works mentioned above show that the laser pump/X-ray probe XAFS, using or not the temporal structure of third generation SR, provides a powerful approach to monitor transient molecular structures in disordered media. For many metal-containing photoactive molecules, one of the most important electronic transitions that govern reactivity is the metal-to-ligand-charge-transfer (MLCT) transition, which involves moving electrons from the metal ion to ligands, producing a transient change in the oxidation state of the metal ion. This electronic change can be, in principle, detected by XAFS spectroscopy. Inevitably, such transient oxidation changes could cause atomic displacements as well, which can also be detected by XAFS.

Chapter 2

Time-resolved studies at ID24

This chapter describes the special characteristics of beamline ID24 that make it suitable for time-resolved studies. The CCD camera detector together with different acquisition methods allow to have different time-resolution up to a maximum of 100 μs per spectrum. The principle of the synchronization method (triggering) of the pump and the probe in time-resolved experiments is described.

2.1 Detection system

Thanks to the parallel acquisition mode that allows data for all energies to be collected simultaneously, XAS using dispersive optics is particularly suited to the study of dynamical processes. The dispersive XAS beamline of ESRF, ID24, has been specifically designed to benefit from the high brilliance of its undulator source, in order to reach a time resolution of the order of 100 μs. This is achieved through a position sensitive detector, consisting of a scintillating screen coupled to a CCD camera with a fast analog buffer [24]. The CCD camera (1152 pixels (V) × 1242 pixels (H)), in fact, presents an unexposed part used as a buffer to store successive spectra and 64 lines are exposed (Figure 2.1). After the exposure, the obtained image ("stripe") is shifted into the remaining part of the CCD that is shielded against exposure. This operation is repeated until the CCD is filled up with successively recorded images, 18 in the case of the CCD presently installed on the beamline ID24. We define "cycle" the sequence of 18 stripes

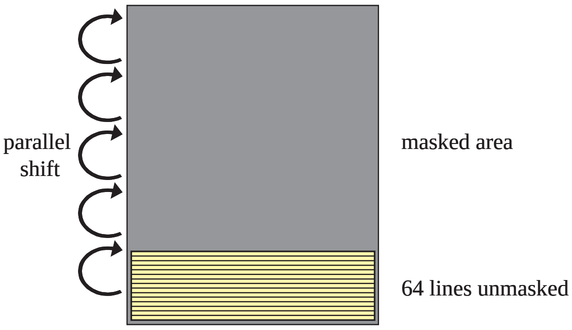

Figure 2.1: Scheme of the CCD camera of beamline ID24. The unexposed part is used as a buffer.

acquired between serial readouts. Each image is then binned, meaning that the charges in the exposed lines are summed up into a single line (which corresponds to 1 spectrum), which is then read out serially. The dead time for the serial readout of each image is ∼ 250 ms.

Two different scintillating screens can be coupled with the CCD camera: P43 (Gd_2O_2S:Tb) and P46 ($Y_3Al_5S_{12}$:Ce). They differ in their absorption efficiency and their time response: that is to say, the first (P43) has a better efficiency but a slow time response and the second (P46) is less efficient but has a faster decay. Figure 2.2 refers to [24] whereas Figure 2.3 refers to recent tests done on ID24. The comparison between the time response of the two phosphor screens is summarized in Table 2.1. [1]

	lifetime τ ($A = A_0 e^{-t/\tau}$) (theoretical[1])	lifetime $A = 0.5\ A_0$ (measured)	lifetime $A = 10^{-2}\ A_0$ (measured)	lifetime $A = 10^{-3}\ A_0$ (measured)	Afterglow A/A_0 (after 1 min.) (theoretical[1])
P43	1 ms	820 μs	3600 μs	5.3 ms	10^{-6}
P46	300 ns	120 μs	350 μs	5 - 6 ms	10^{-3}

Table 2.1: Comparison between the time response of the two phosphor screens.

P46 is therefore to be preferred only for processes with timescale less than millisecond, since on the 10 ms and above scale its afterglow exceeds that of P43.

---

[1] From "Proxitronic" (phosphor coatings, Germany). These values are the decay times from 90% to 10% of the initial value.

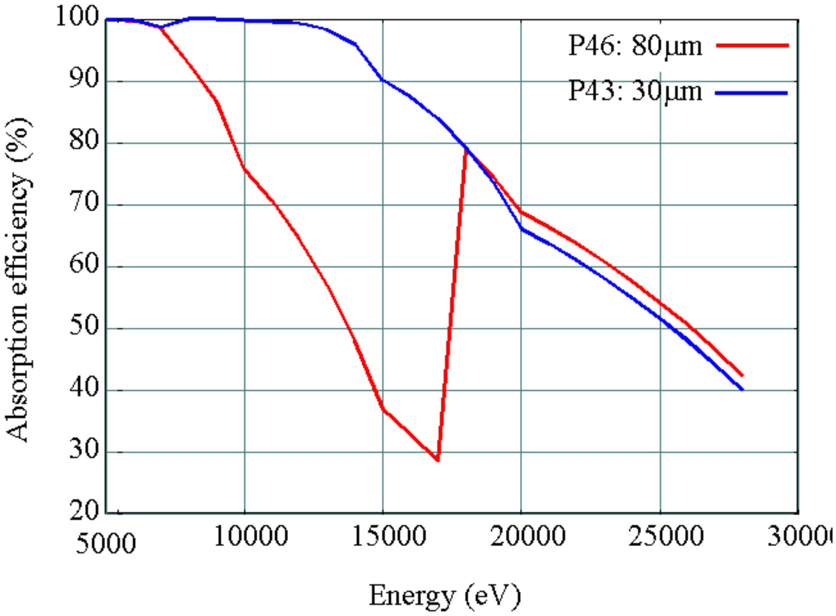

Figure 2.2: Absorption efficiency as a function of energy.

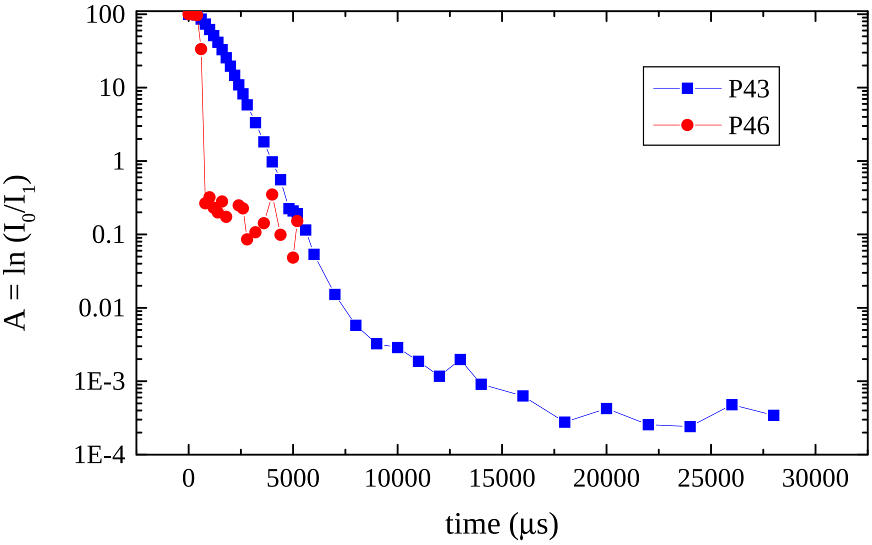

Figure 2.3: Measured temporal response: the shutter is closed at t = t_0 = 400 μs.

2.2 Acquisition methods for TR experiments

Two data acquisition methods are possible, depending on the desired time resolution.

Slow mode

This mode (Figure 2.4) allows to have a maximal time resolution of $\sim$ 300 ms. The transition from an initial state A to a final state B takes place between two different cycles, the transient process is supposed to be slow enough that all the spectra recorded within a cycle present the same average characteristics.

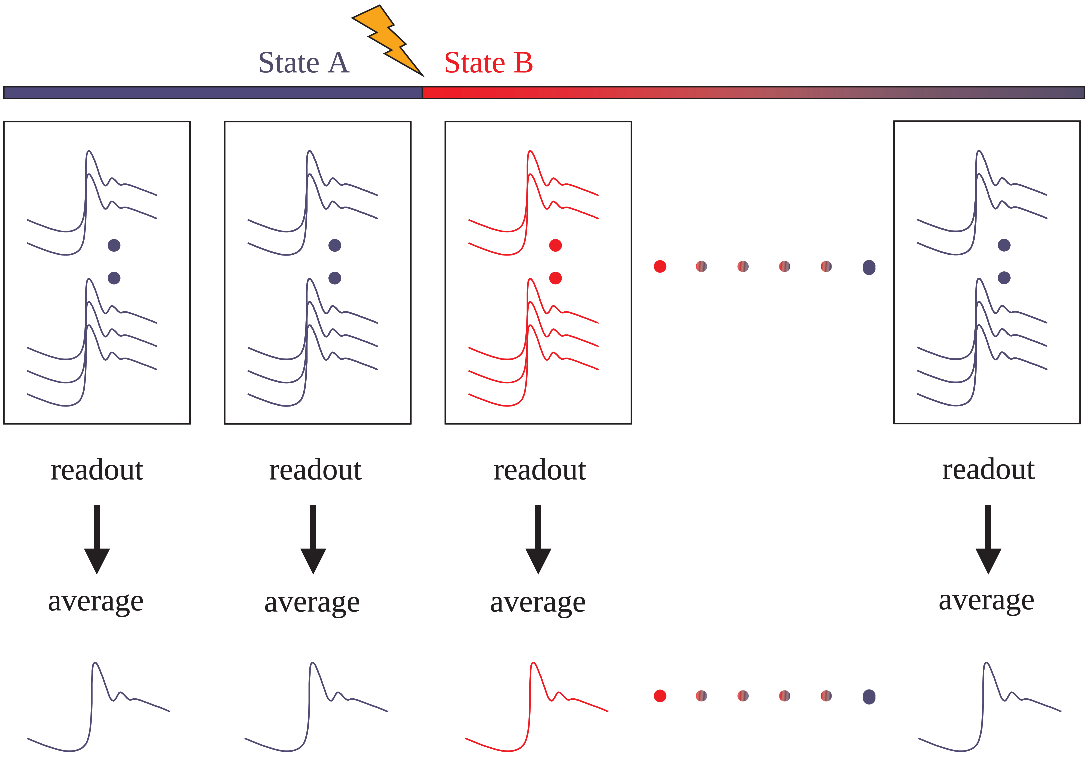

Figure 2.4: Slow acquisition method: the 18 spectra per each cycle are averaged.

Fast mode

This mode (Figure 2.5) allows to have a maximal time resolution of 100 μs, which corresponds to the minimum exposure time of a single stripe of the CCD. The transition from an initial state A to a final state B takes place between two different spectra within the same cycle. To improve statistics the transient process can be repeated. With an optimal synchronization, it is possible to have the start of the process always in the same spectrum of different cycles, allowing the possibility of averaging each corresponding set of spectra.

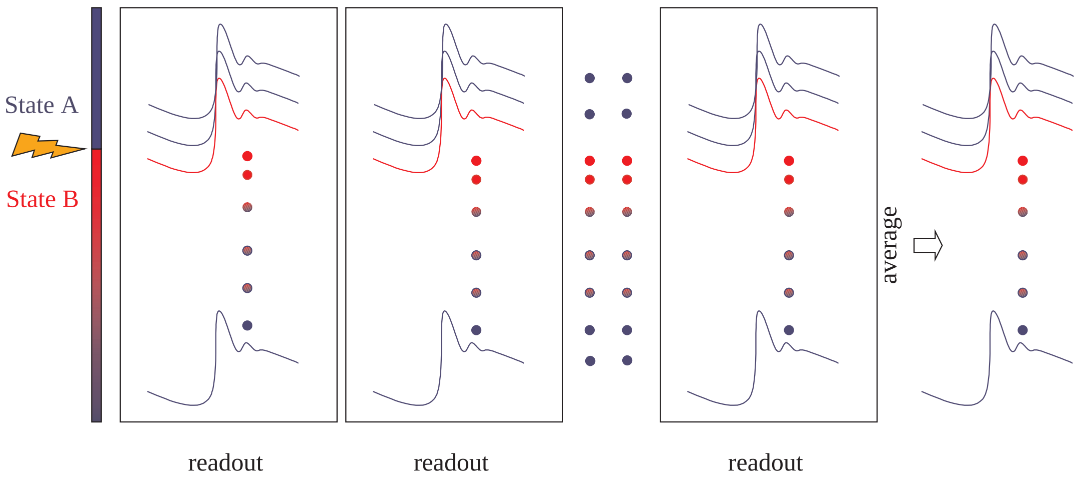

Figure 2.5: Fast acquisition method: the corresponding spectra of different cycles are averaged.

2.3 Triggering

For TR experiments, it is mandatory that the pump which triggers the reaction in the sample is synchronous with the X-ray probe, which monitors the response of the sample. In the *fast acquisition mode*, the timing sequence for the pump and data collection is shown in Figure 2.6. A starting signal from a VCT6 card, the *"T-signal"*, initiates the sequence and all the following events: start of the pump, start of the acquisition, opening and closing of a fast shutter, all with their corresponding delays are relative to this signal. The starting time of the acquisition t_i, the total acquisition time t_E, the exposure time of a single stripe t_e[2], and the waiting time t_w before the start of the next cycle are set by the acquisition program. The start of the pump pulse and the opening and closing of the fast shutter (t_{os} and t_{cs})[3].

---

[2] $t_E = 18 \times t_e$, as it is possible to record 18 spectra in one cycle before the readout of the CCD camera.

[3] Since the CCD is always exposed, a fast shutter is used to avoid the saturation of the CCD and to protect the sample from the radiation. The shutter is open only during the effective data acquisition, its opening and closing time are given by a delay generator connected to the T-signal. Since the opening and the closing of the fast shutter are relatively "slow" processes ($\sim$ 10 ms after open/close pulse signals are sent), generally its opening pulse signal has to precede t_i and its closing pulse signal can precede $t_i + t_E$.

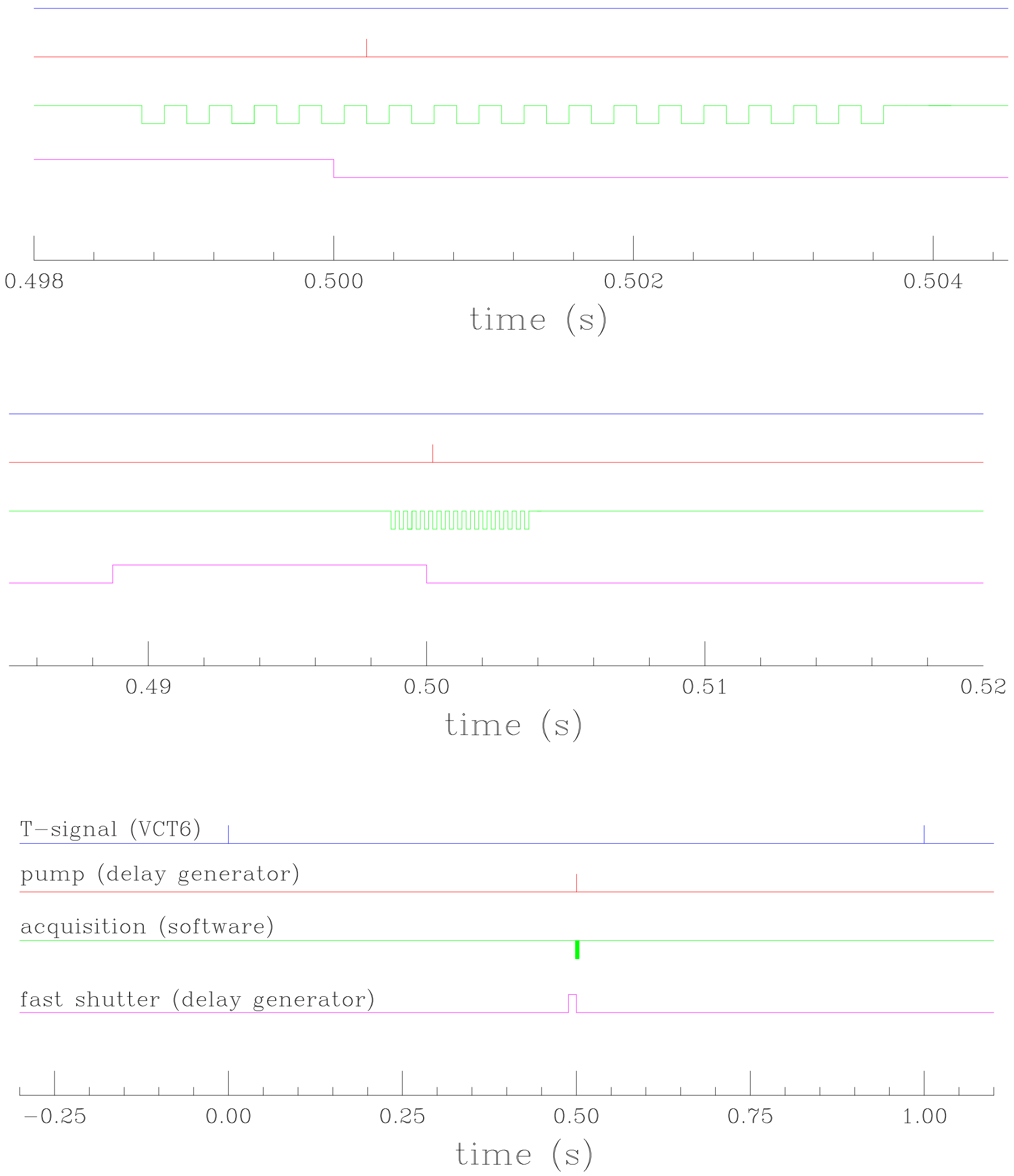

Figure 2.6: Timing sequence: from bottom to top the acquisition zone is expanded.

Chapter 3

Scientific case: $Pt_2(P_2O_5H_2)_4{}^{4-}$

This chapter concerns the time-resolved X-ray absorption experiment performed on beamline ID24 on a system of choice: $Pt_2(P_2O_5H_2)_4{}^{4-}$*. The experimental prerequisites for this kind of experiments made this system potentially suitable for the investigation of an excited state structure using X-ray absorption spectroscopy. The previous studies on this system using different techniques are reviewed and the experimental part is described in detail. Following the result obtained, that is in contradiction with an analogous previous study, other complementary experiments have been carried out. A possible explanation of our result is given.*

3.1 Experimental prerequisites for TR-XAS experiments

One of the key requirements for a photoexcitation experiment is a high number of photons per each laser pulse, because this directly influences the number of molecules that undergo photoexcitation. Therefore, the larger the fraction of the excited state molecules, the more likely it is to determine the transient structure. Another requirement is the synchronization of the laser pump pulse with the X-ray probe. However, the most critical point is the choice of the sample. The requirements are the following:

i. the sample must be robust, to permit the accumulation of the numerous individual measurements that comprise a complete data set. That is, the sample must withstand illumination by X-rays and laser without exhibiting significant radiation damage;

ii. the sample must be stimulated uniformly and rapidly by an intense laser pulse, to achieve the initiation of the transient process;

iii. as the time resolution of our setup is 100 μs, the lifetime of the excited state has to be long enough to be detected;

iv. the structural distortions of the excited state have to be large enough to be detectable on the XANES/EXAFS signal;

v. the sample must have edge energies compatible with the beamline.

3.2 Why $Pt_2(P_2O_5H_2)_4{}^{4-}$?

The model system chosen to pinpoint our technique was Tetrakis(pyrophosphito)diplatinate(II) ($Pt_2(P_2O_5H_2)_4{}^{4-}$). The sample was provided by Prof. James Penner-Hahn from University of Michigan (USA) through collaboration on experiment CH760. It consists of two Platinum centers with four bridging pyrophosphite ligands as shown in Figure 3.1. The structure, optical characteristics and photochemistry of this molecule have been extensively studied [25–33]. Several of its characteristics make it a good subject for microsecond XAFS measurements. First, its triplet excited state has, at room temperature, a lifetime of 9 μs, this goes up to about 1 ms at 5 K. Second, this state can be significantly populated by laser irradiation because the ground state absorption is high ($\varepsilon = 33500$ M^{-1} cm^{-1} at 367 nm), and the quantum yield of formation is large (0.5). Third, a large contraction (~ 0.2 Å) of the Pt–Pt separation on excitation has been inferred from vibrational analysis. Fourth, it is possible to perform the measurements at the L_3–edge (11.564 keV) of Platinum, this is a suitable energy to be studied on ID24 using a Bragg symmetry monochromator.

3.3 Previous studies on $Pt_2(P_2O_5H_2)_4{}^{4-}$

The intense, vibronically structured, green phosphorescence observed from $Pt_2(P_2O_5H_2)_4{}^{4-}$ has provided a wealth of information regarding the structure and bonding of the low-lying excited state of this D_{4h} anion. Fordyce *et al.* [27] reported the observation of both a fluorescence and a phosphorescence on $Pt_2(P_2O_5H_2)_4{}^{4-}$. The

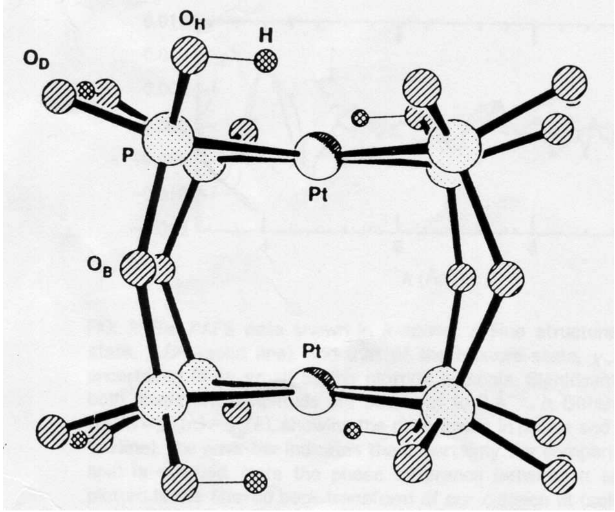

Figure 3.1: Perspective drawing of $Pt_2(P_2O_5H_2)_4{}^{4-}$. The subscript on the Oxygen atoms have the following meanings: B denotes a bridging Oxygen, H denotes an Oxygen that has a Hydrogen attached, and D denotes an Oxygen which is double-bonded to the Phosphorous.

absorption spectrum of $Pt_2(P_2O_5H_2)_4{}^{4-}$ in water at room temperature is characterized by four maxima at 452 nm (ε = 120 M^{-1} cm^{-1}), 367 nm (ε = 33500 M^{-1} cm^{-1}), 303 nm (ε = 849 M^{-1} cm^{-1}), and 270 nm (ε = 1360 M^{-1} cm^{-1}), where ε is the extinction coefficient. Two emissions are observed: an intense green band (phosphorescence) at 515 nm and and a much weaker band (fluorescence) at 403 nm. A simple molecular orbital model accounts for these spectroscopic data. In this view the two HOMOs (highest occupied molecular orbital) are the bonding $\sigma(d_{z^2})$ and antibonding $\sigma^*(d_{z^2})$ combinations of $5d_{z^2}$ orbitals centered on each Pt(II) ion. The two LUMOs (lowest unoccupied molecular orbital) result from the bonding $\sigma(p_z)$ and antibonding $\sigma^*(p_z)$ combinations of the Pt(II) $6p_z$ orbitals. The ground and lowest excited configurations of the complex are $[\sigma^*(d_{z^2})]^2$ and $\sigma^*(d_{z^2})\sigma(p_z)$, respectively. The resulting state assignments in D_{4h} symmetry, are diagrammed in Figure 3.2. Given that ${}^1A_{1g}$ is the ground state, the lowest excited configurations, the spin triplet (${}^3A_{2u}$) and the spin singlet (${}^1A_{2u}$), are derived from the $\sigma^*(d_{z^2})\sigma(p_z)$ configuration. The absorption peak at 367 nm is assigned to the ${}^1A_{1g} \rightarrow {}^1A_{2u}$ transition and the weak emission at 403 nm to the corresponding fluorescence. The weak absorption peak at 452 nm is assigned to the ${}^1A_{1g} \rightarrow {}^3A_{2u}$ transition and the intense emission at 515 nm to the corresponding phosphorescence. Coincidence of the peaks in the emission excitation verifies that both

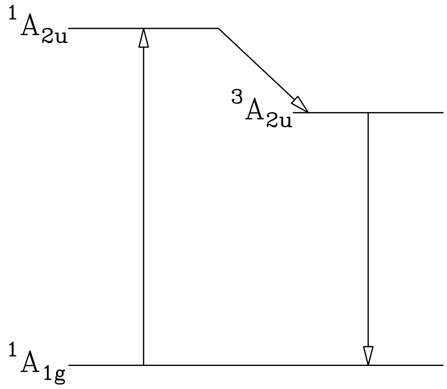

Figure 3.2: Energy level diagram of the lowest excited state of $Pt_2(P_2O_5H_2)_4{}^{4-}$ under D_{4h} symmetry.

emissions generate from $Pt_2(P_2O_5H_2)_4{}^{4-}$. Since the lowest energy transition involves promotions of an electron from an antibonding to a bonding molecular orbital, it should produce a contraction of the Pt(II)-Pt(II) bond distance. In another work [29], Rice and Gray determined the ground-state vibrational frequency to be 110 cm^{-1} and the vibrational frequency of the $^3A_{2u}$ excited term to be 155 cm^{-1} confirming the prediction that the 0.2 Å distortion [29] is indeed a contraction of the 2.92 Å ground-state Pt–Pt bond-length. The same conclusion was reached by using time-resolved resonance Raman measurements [30].

Besides Raman and infrared spectroscopy, that can provide only an indirect information about the bond distance of the two metal centers, in 1993 Thiel *et al.* [8] reported microsecond resolved XAFS measurements of the excited triplet electronic state $^3A_{2u}$ of $Pt_2(P_2O_5H_2)_4{}^{4-}$ in solution employing a new technique. This technique involved a circulation system, which allowed rapid flow of the solution under investigation, a laser with appropriate optics to excite the molecule, and a SR source with the required instrumentation for XAS. The solution was passed through a nozzle to form a free-standing jet (Figure 3.3). The sample was excited by focusing the laser beam on the jet, and the X-ray beam is subsequently directed at the jet downstream of the laser focus. If the pump and probe regions do not overlap, the time resolution is limited by time t for which the flowing molecules reside in the laser focus and the X-ray beam. This is given by $t = h/v$ where $h = h_1 + h_2$ is the combined height of the two beams. The optical probe showed that 18% of the molecules within the probed region were in

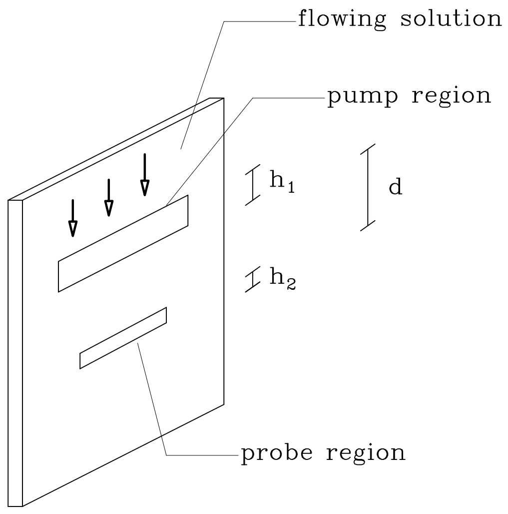

Figure 3.3: Schematic view of the sample holder. By varying d, the displacement between the laser beam and the X-ray beam, one can monitor the kinetics of the decay of the excited state. This parameter d provides the time delay Δt given as Δt $= d/v$ where v is the velocity of the flowing sample.

the triplet excited state. The Pt L_3 absorption edge was studied. As the sample was dilute (C = 0.7 mM), the X-ray absorption measurements were done in fluorescence. Following the standard data analysis, the functions $\chi_m(k)$ and $\chi_g(k)$ were extracted from the data, where $\chi_m(k)$ is a mixture of the ground state XAFS $\chi_g(k)$ and the pure excited state XAFS $\chi_e(k)$. The authors determined the values of three fitting parameters: $\Delta r_1 = -0.047 \pm 0.011$ Å, $\Delta r_2 = -0.285 \pm 0.065$ Å, and $\Delta r_3 = -0.06 \pm 0.05$ Å, corresponding to changes in radial separation between the absorbing Pt atom and the near P, the far P, and the bridging O, respectively. Statistical noise precluded the determination of any other XAFS parameters. Assuming that the Phosphorous atoms remain planar in the triplet state, by simple geometry the values of Δr_1 and Δr_2 translate into an inward movement of the P planes along the Pt–Pt axis by 0.52 ± 0.13 Å, with a smaller contraction of 0.047 ± 0.011 Å of the Pt–P bond within the planes on excitation. The contraction between the planes is roughly twice that previously found for the Pt–Pt bond.

3.4 TR XAS experiment

As already reported, one of the major experimental issue in performing experiments where the aim is to detect structural modifications of the excited states is the difficulty to have a detectable excited-state population in the volume of the sample probed by the X-ray beam. In a geometry in which the laser beam and the X-ray beam are perpendicular to each other (Figure 3.4), the penetration depth of the laser photons

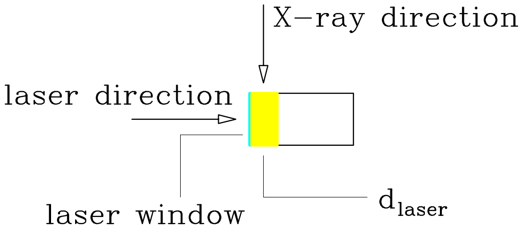

Figure 3.4: Geometry in which the laser beam and the X-ray beam are perpendicular to each other.

d_{laser} must match the depth of the sample probed by the X-ray beam d_{X-rays}:

$$d_{laser} \simeq d_{X-rays}.$$

d_{X-rays} is equal to the horizontal focal spot of the X-ray beam (~ 100 μm at the base of the distribution at Pt L_3–edge); d_{laser} can be quantified as the distance from the laser window which yields, for the given sample concentration, an optical density (OD) of 1:

$$d_{laser} = d_{OD} = 1,$$

with OD = ε C d_{laser}, where ε is the extinction coefficient and C is the concentration. For a given sample concentration, the penetration depth of the laser depends critically on the wavelength of the photons, through the ε of the system. The extinction coefficient is given for the system under study, so the choice of the concentration of the sample becomes a very important parameter.

3.4.1 Experimental details

A TR experiment has been performed on ID24, using a $K_4[Pt_2(P_2O_5H_2)_4]$ salt dissolved in an aqueous solution containing 76% glycerol by weight to obtain a concentration of 15 mM in Pt. We used a Nd:YAG laser (λ = 1064 nm), provided with two insertable modules containing non-linear crystals for the generation of the second (λ = 532 nm) and of the third harmonics (λ = 355 nm). The excitation wavelength chosen was λ = 355 nm, the pulse duration 4 ns and the energy per pulse E_{laser} 65 mJ. Given that the energy of a photon at 355 nm is

$$E_{\lambda=355} = h\nu = \frac{hc}{355 \cdot 10^{-9}} = 5.6 \cdot 10^{-19}\mathrm{J},$$

the number of photons per pulse $\mathcal{N}$ is

$$\mathcal{N} = \frac{E_{laser}}{E_{\lambda=355}} \backsimeq 10^{17}.$$

At 355 nm the extinction coefficient $\varepsilon \backsimeq 12000$ $\mathrm{M}^{-1}\mathrm{cm}^{-1}$ and with the concentration used, for OD = 1, the laser penetration depth d_{laser} is about 100 μm, comparable to the focal spot of the beam at the L_3–edge of Pt. The pathlength in the X-rays direction was 6 mm in order to have a jump of $\sim$ 0.2 in the absorption spectrum. Considering that the dimensions of the X-ray beam were H×V = 100 μm × 400 μm, the effective volume probed by the x-ray beam was 0.24 mm^3 corresponding to 10^{15} molecules of complex. The laser was focused in order to yield a focal spot of $\sim$ 6 mm × 0.4 mm (H×V). Since the number of photons per pulse is two orders of magnitude bigger than the number of molecules in the irradiated region, the requirement on the laser pulse power is fulfilled. The setup of the experiment is shown in the photograph (Figure 3.5).

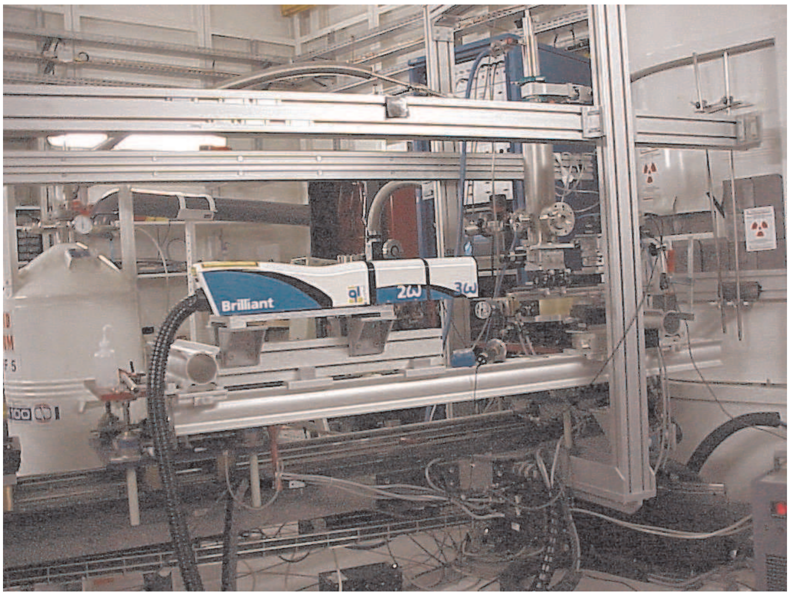

Figure 3.5: Setup of the TR experiment on $Pt_2(P_2O_5H_2)_4{}^{4-}$ performed on ID24.

In order to have an excited state lifetime long enough to be detected (700 μs), the sample was cooled down to 10 K in a cryostat borrowed from ID26 equipped with two kapton windows in the direction of X-ray beam and two optical windows in the perpendicular direction. The laser and the X-ray beams were perpendicular to each other and the laser beam was focused onto the sample by using an optical system sketched in Figure 3.6.

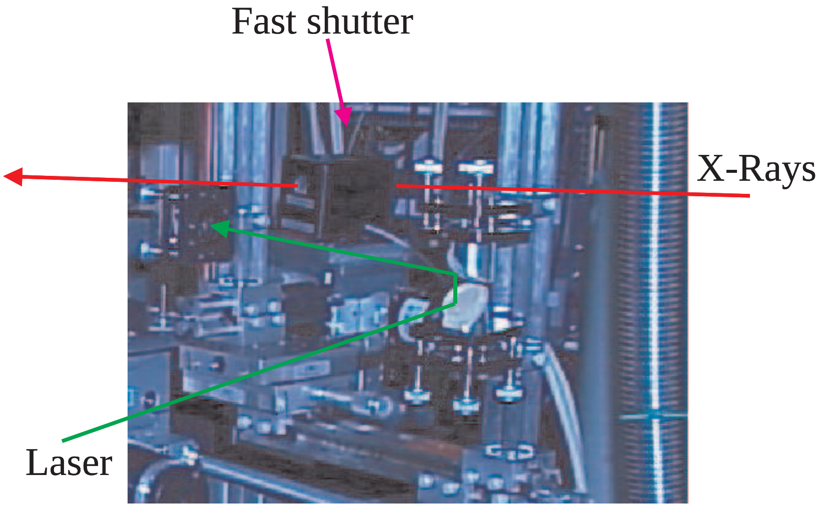

Figure 3.6: The laser beam, initially parallel to the X-ray beam is reflected in the vertical direction by a high-energy 45° incidence beam-steering mirror for UV-light, the beam is then reflected by a second mirror and focused by concave lens onto the sample.

The sample holder, shown in Figure 3.7, was made in Teflon and consisted of two compartments: one for the sample solution and one for the solvent for the I_0 acquisition. The thickness of 6 mm in the X-ray path was defined by two parallel kapton windows.

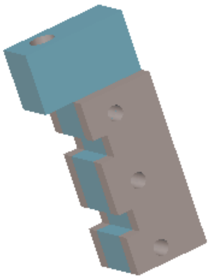

Figure 3.7: Sample holder used for TR X-ray absorption experiment. The laser and the X-ray beams are perpendicular to each other. The sample compartment is 6 mm thick in the X-ray path defined by two parallel kapton windows. In the laser direction no windows are present.

The sample was loaded in the cell using a syringe and was rapidly frozen by immersion in liquid Nitrogen prior to the insertion in the cryostat. No windows were used in the laser direction. The X-ray beam was positioned as close as possible to the laser irradiated side of the sample in order to match the part of the sample excited from the laser and the part of the sample probed by the X-rays. Since the integration time per spectrum was 300 μs the scintillating screen used was the P46. We saw in fact that the after 350 μs $A = 10^{-2}$ A_0 (see Table 2.1).

3.4.2 Synchronization of the measurements

The T-signal from VCT6 initiates the sequence and all the other delay times are relative to this signal. The electronic scheme is shown in Figure 3.8.

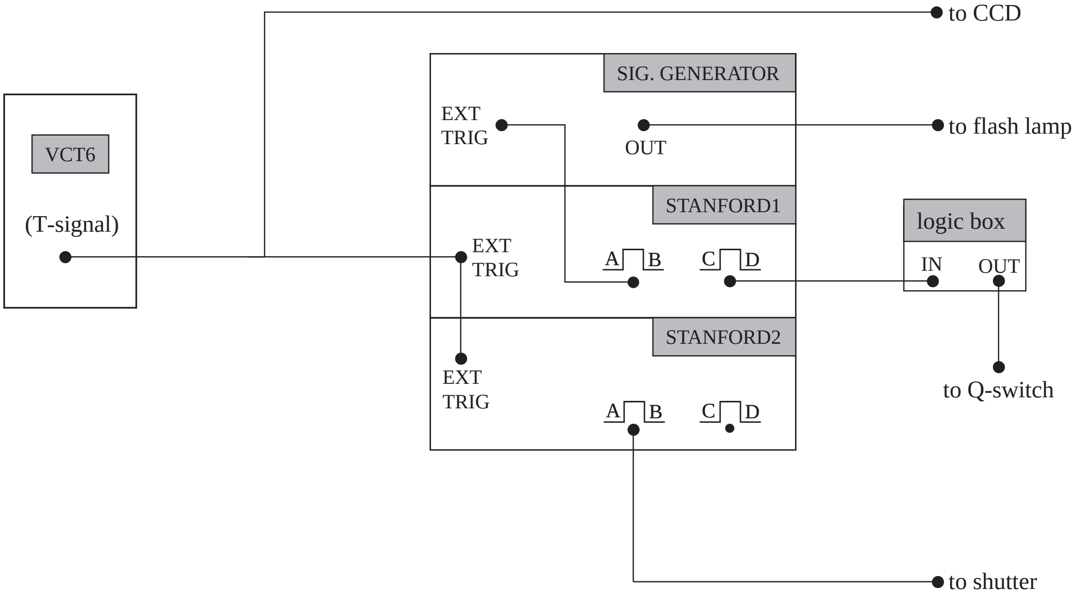

Figure 3.8: Schematic representation of synchronization setup for the TR-XAS experiment on ID24.

The VCT6 generates the T-signal that, divided by two, goes to the external trigger channel of the CCD camera, and to a delay generator STANFORD1 that controls the laser. From STANFORD1 the T-signal is sent to a second delay generator STANFORD2 that controls the fast shutter. The laser is fired every two acquisition cycles. This choice allows to improve the normalization of the data, by using the data in cycle $n + 1$ (no laser excitation) to normalize those in cycle n (with laser excitation). The flashlamp of the Nd:YAG laser is fired 20 times at 10 Hz at each acquisition cycle, i.e. every two T-signals, by means of a signal generator through channel A of STANFORD1. The signal to the Q-switch, delayed by 220 μs respect to that to the flash lamp (to guarantee the maximum laser power) is triggered to the n^{th} stripe of the acquisition cycle through channel C of STANFORD1 connected to a logic box that allows to fire the Q-switch every 2 acquisition cycles. Channel A of STANFORD2 is connected to the fast shutter, the values A and B determine the opening and the closing of the shutter in particular A = t_{os} and B = t_{cs} - t_{os}.

3.4.3 Data acquisition

Using the triggering system described in the previous section, we acquired two series of 4000 cycles to have good statistics with an integration time of 300 μs per spectrum. In the first series we fired the laser at the 6th spectrum of each odd cycle (Figure 3.9). In the second case we never fired the laser during the 4000 cycles (Figure 3.10).

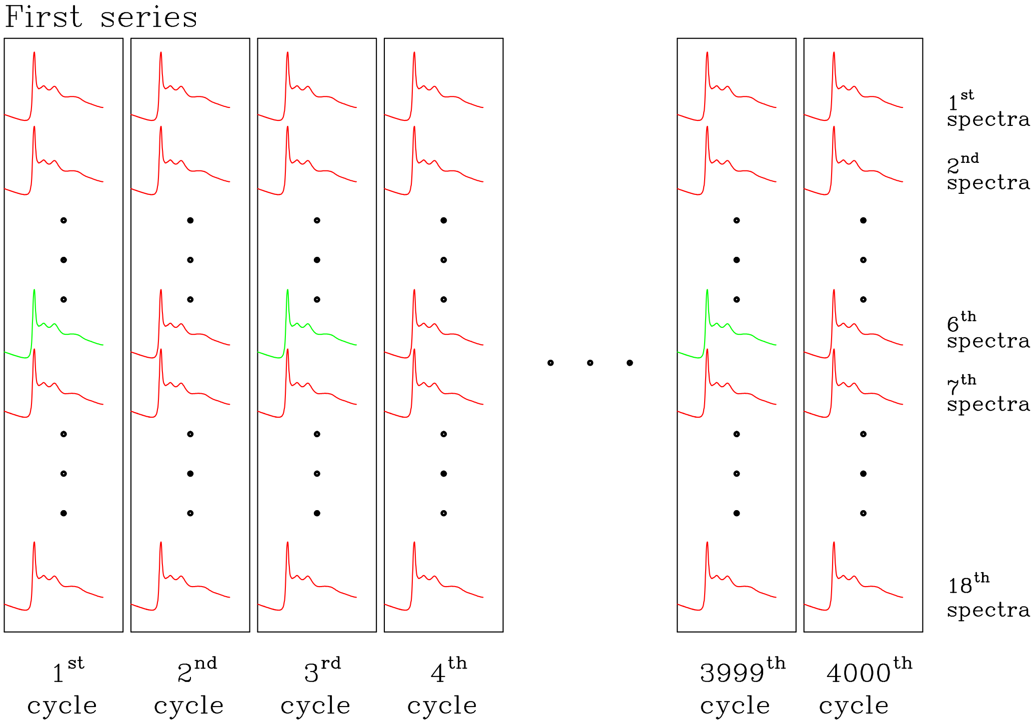

Figure 3.9: The acquisition strategy of the first series: the laser is fired at each 6^{st} spectrum of every odd cycle (green spectrum).

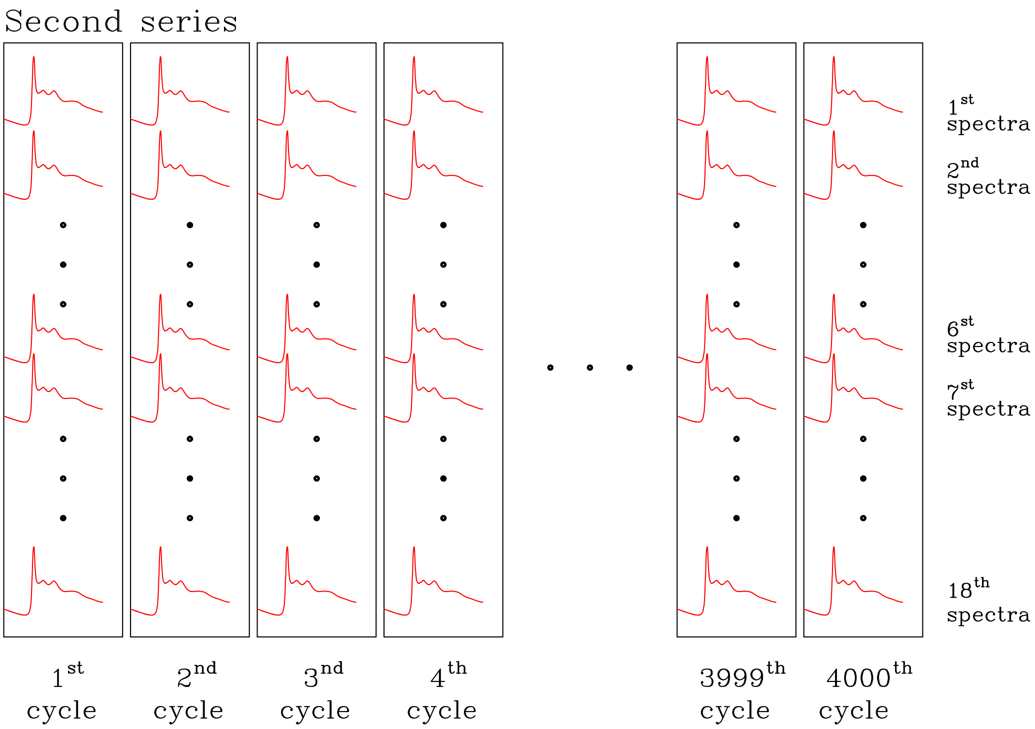

Figure 3.10: The acquisition strategy of the second series: 4000 cycles are recorded without firing the laser.

3.5 Expected and obtained results

On the basis of previous studies, the triplet state of $Pt_2(P_2O_5H_2)_4{}^{4-}$ undergoes a contraction in the Pt–Pt distance relative to the ground state. The amount of this contraction is controversial in the literature, it goes from a minimum of 0.21 Å [29] to a maximum of 0.52 Å [8]. To evaluate the entity of the difference signal that we were supposed to detect, considering a 100% photoexcitation yield, we compared the experimental XAFS signal $k\chi_{exp}(k)$ of the sample with the simulated signal in the ground state $k\chi_g(k)$ and the triplet excited state $k\chi_e(k)$. We recorded a Pt L_3–edge (E = 11.564 keV) EXAFS spectrum of an aqueous solution of $K_4[Pt_2(P_2O_5H_2)_4]$ with a concentration of 15 mM in Pt. This measurement was done on BM29 during a shift in single-bunch mode. The data analysis was performed first by calculating *ab initio* the EXAFS signals and then by performing a non-linear fitting of the ground state theoretical signal on the experimental signal (for details about the analysis method see [34]). The theoretical signals corresponding to the scattering of Pt–P(near), Pt–P(far), Pt–O(near), Pt–O(bridge), Pt–O(far), Pt–Pt, each multiplied by the correct multiplicity, were used to model the experimental signal. The value for the Pt–Pt distance was 2.92 ± 0.02 Å. The best fit of $k\chi_g(k)$ to $k\chi_{exp}(k)$ is shown in the left panel of Figure 3.11. The simulated signal of the triplet state was calculated considering a contraction of the

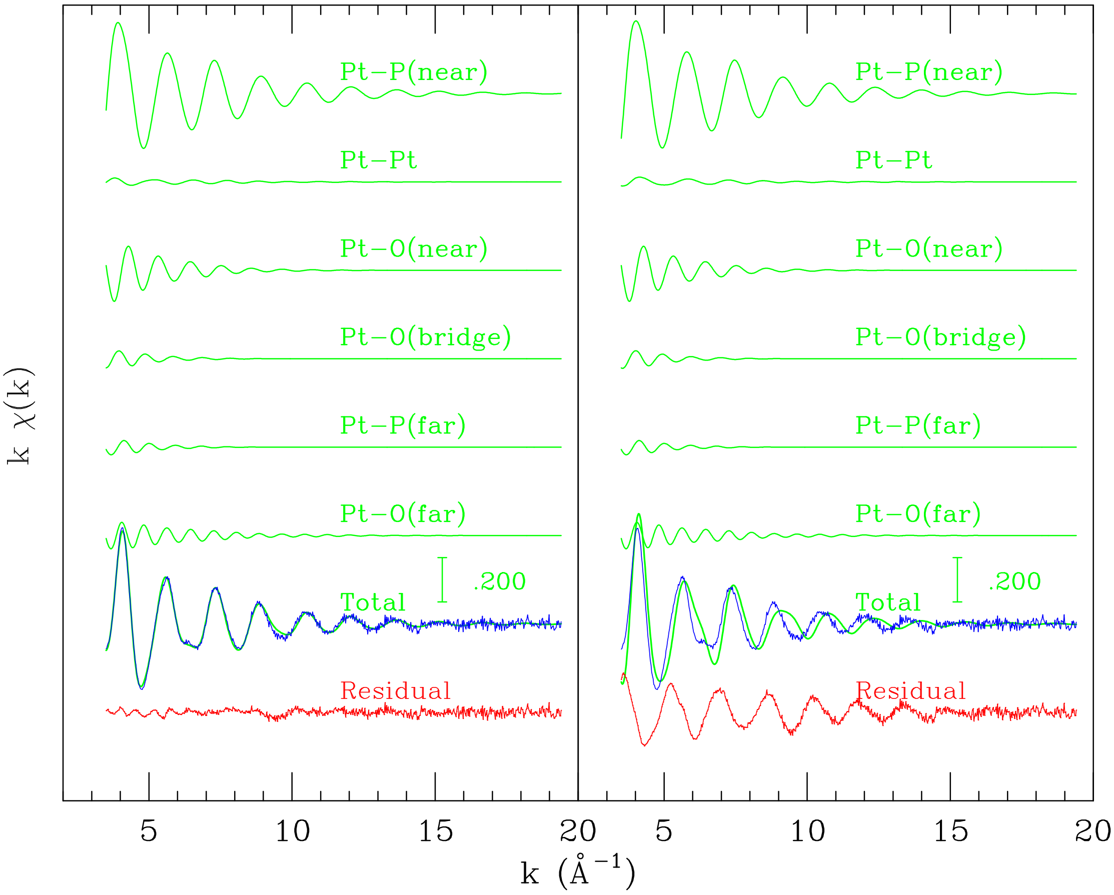

Figure 3.11: *Left Panel*: comparison of experimental and calculated best fit $k\chi(k)$ XAFS signal of $Pt_2(P_2O_5H_2)_4{}^{4-}$. *Right panel*: simulated XAFS signals of the triplet excited state of $Pt_2(P_2O_5H_2)_4{}^{4-}$.

Pt–Pt distance of ∼ 0.2 Å [29], assuming that the Phosphorous atoms remain planar in the triplet state, and a contraction of 0.047 Å of the Pt–P bond within the planes on excitation according to [8]. The right panel of Figure 3.11 shows the comparison between the experimental $k\chi_{exp}(k)$ and the 100% excited triplet state simulated $k\chi_e(k)$. Figure 3.12 shows, in the *left panel*, different linear combinations $k\chi_{m(x)}(k)$ of the best-fit $k\chi_g(k)$ signal and the simulated excited state signal $k\chi_e(k)$. $k\chi_{m(x)}(k)$ is defined as $k\chi_{m(x)}(k) = (1-x)k\chi_g(k)+xk\chi_e(k)$. From bottom to top, the $k\chi_{m(x)}(k)$ functions have an increasing weight of the $k\chi_e(k)$ term. The right panel shows the difference between

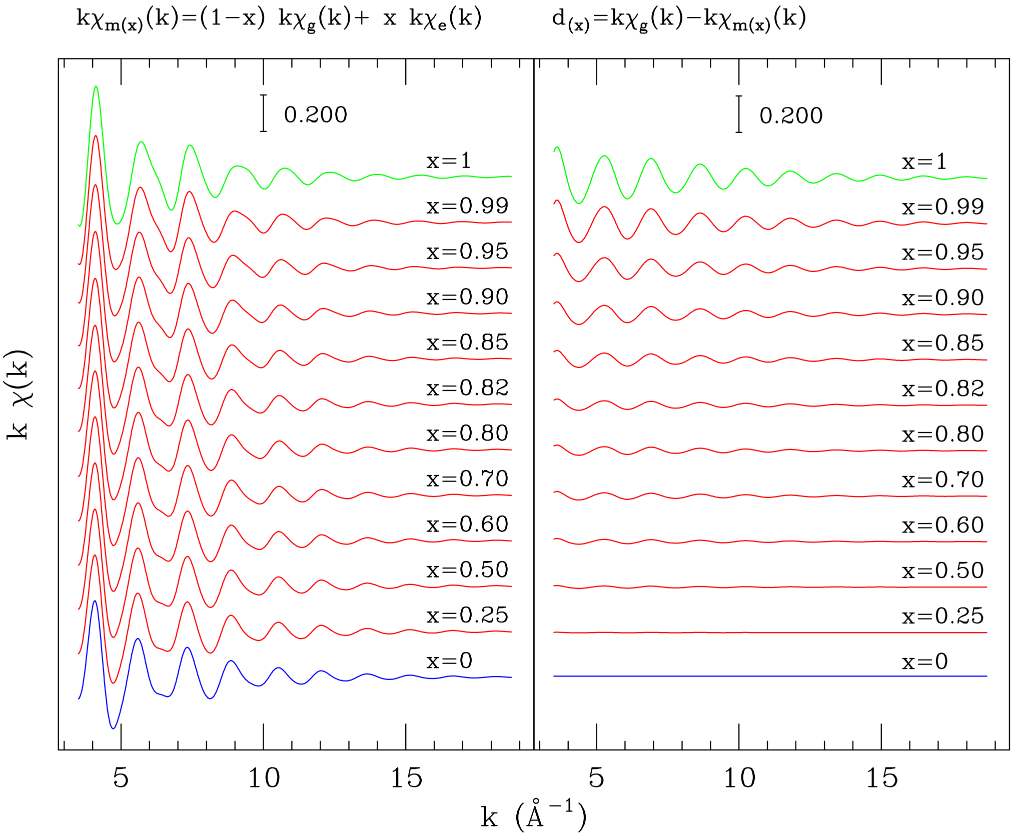

Figure 3.12: *Left panel*: different linear combinations $k\chi_{m(x)}(k)$ of the best-fit XAFS signal $k\chi_g(k)$ and the simulated XAFS signal $k\chi_e(k)$. From bottom to top, the $k\chi_{m(x)}(k)$ functions have an increasing weight of the $k\chi_e(k)$ term. *Right panel*: difference between $k\chi_g(k)$ and $k\chi_{m(x)}(k)$ with an increasing value of x from bottom to top.

$k\chi_g(k)$ and $k\chi_{m(x)}(k)$ with an increasing value of x from bottom to top. We observe that a minimum percentage of 15% of excited state molecules have to be present in the sample to distinguish the “difference signal” from the noise level of the measurements.

The data of the TR experiment performed on ID24 were analyzed in the following way: for the first series we summed all the corresponding spectra of all odd cycles and the corresponding spectra of all even cycles and made the difference. We did the same for the second series. We then end up with 18 summed spectra for each series. The Figure 3.13 shows “difference spectra” obtained by taking the difference between two spectra. From bottom to the top: (spectrum 5 - spectrum 6), (spectrum 5 - spectrum 7), ... (spectrum 5 - spectrum 11). We do not observe any significant difference between the first (with laser excitation) and the second series (no laser excitation).

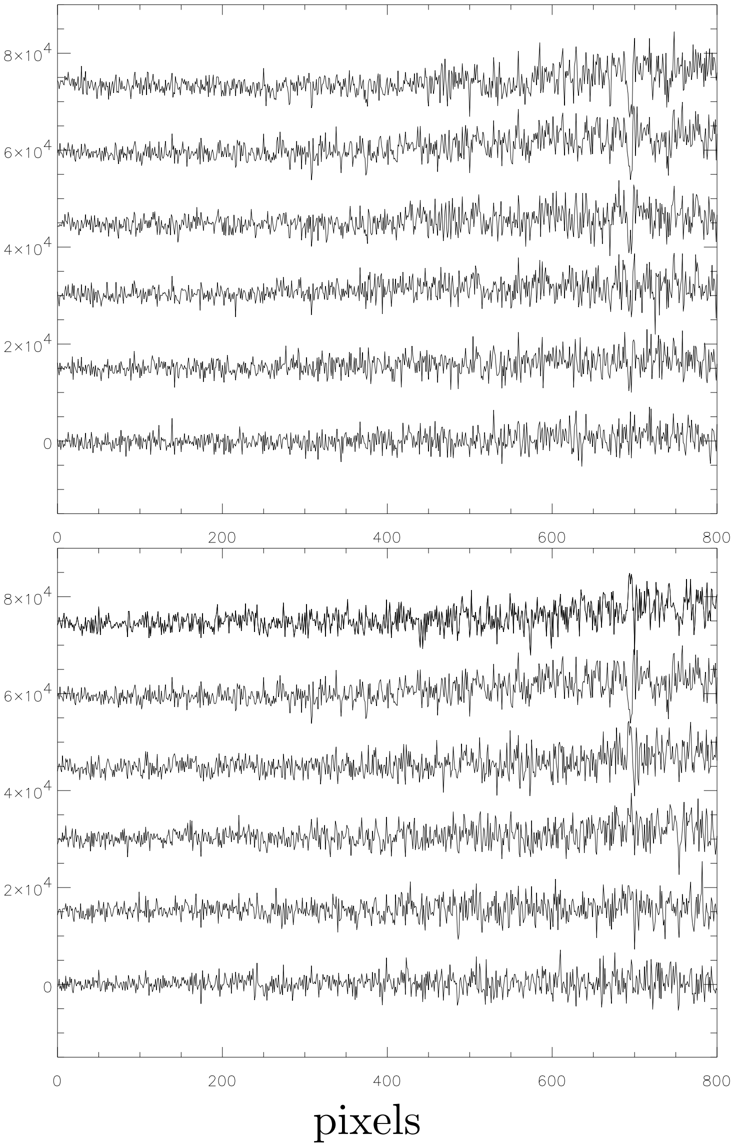

Figure 3.13: "Difference spectra" obtained by taking the difference between two spectra for the first series *(upper panel)* and for the second series *(lower panel)*. From bottom to the top: (spectrum 5 - spectrum 6), (spectrum 5 - spectrum 7), ... (spectrum 5 - spectrum 11).

3.5.1 Effect of X-rays on $Pt_2(P_2O_5H_2)_4{}^{4-}$

Following the negative results described in the previous section, other tests have been carried out. In particular, the effect of the X-ray beam on the sample has been considered. The first preliminary test consisted of simply focusing a normal camera at the sample contained in a transparent sample holder. A green phosphorescence was observed when the X-ray beam hit the sample. Following this preliminary result our task was:

i. to investigate if the X-ray beam excited the sample in its triplet state,

and in the affirmative case:

ii. how this effect was related to the intensity of the X-ray beam (number of photons),

iii. how this effect was linked to the excitation of the Platinum L_3–edge.

To answer to these questions we used a UV-VIS spectrometer in combination with the X-ray beam.

In this test we used a 15 mM solution in degassed water. The sample holder had a section of 6 mm × 10 mm with 4 quartz 200 μm thick windows (Figure 3.14).

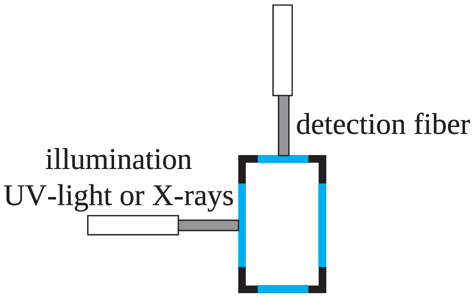

Figure 3.14: Sample holder for the experiment to verify the effect of X-rays on the sample.

The optic fiber of the spectrometer for the detection of the phosphorescence was placed perpendicular to the excitation source. In Figure 3.15 we see the emission spectra obtained following the excitation with photons at $\lambda = 367$ nm corresponding to the maximum of the absorption band and with photons at $\lambda = 355$ nm corresponding to the wavelength of the laser used for the TR experiment. Figure 3.16 shows the emission spectrum following the excitation with the X-ray beam. The emission bands induced by UV photons and by X-rays correspond to the same transition ${}^3A_{2u} \rightarrow {}^1A_{1g}$ as seen by normalizing the two emission bands (Figure 3.17).

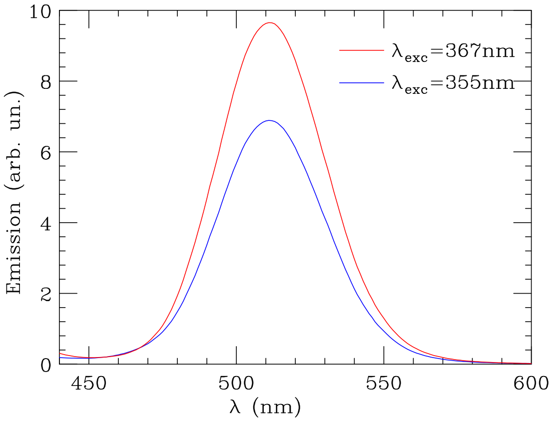

Figure 3.15: Emission band of $Pt_2(P_2O_5H_2)_4{}^{4-}$ under excitation with UV-light at 355 nm *(blue line)* and 367 mn *(red line)*.

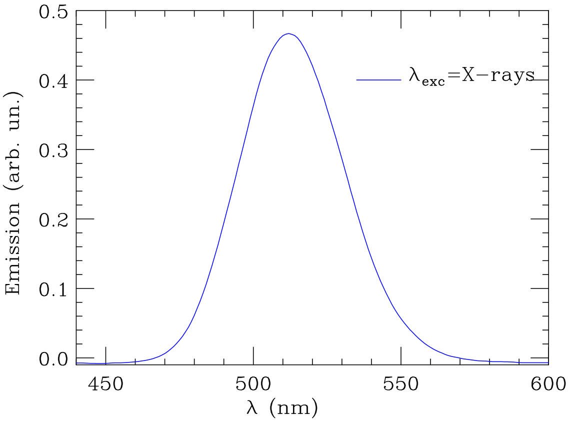

Figure 3.16: Emission band of $Pt_2(P_2O_5H_2)_4{}^{4-}$under excitation with X-rays.

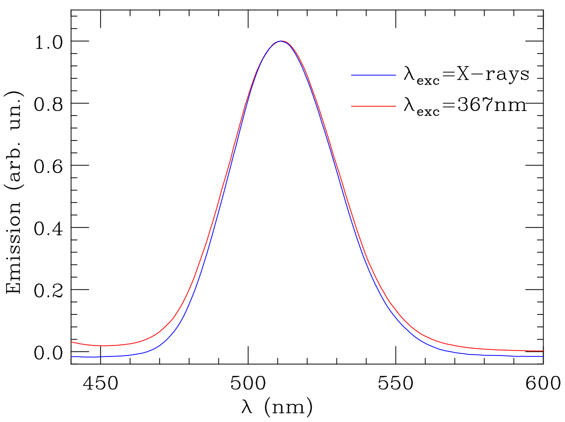

Figure 3.17: Emission band of $Pt_2(P_2O_5H_2)_4{}^{4-}$ under excitation with X-rays *(blue line)*, and 367 nm *(red line)*. The two emission band are normalized to the maximum of the intensity to show that they correspond to the same transition $^3A_{2u} \rightarrow {}^1A_{1g}$.

To see whether the phosphorescence varies as a function of the intensity of the X-ray beam we recorded the emission spectra both with and without filters that attenuated the polychromatic beam. From Figure 3.18 we see that if we calculate the integral of the two emission bands the phosphorescence is attenuated to ∼ 20% by putting 5 mm of Pyrocarbon. Considering that 5 mm of carbon in this energy range (11.400 - 11.990 keV) absorbs ∼ 80% of the intensity of the beam without filters, even though we cannot claim that the intensity of the emission is linear with the intensity of the beam, we can affirm that the more intense the polychromatic beam the more excited the sample.

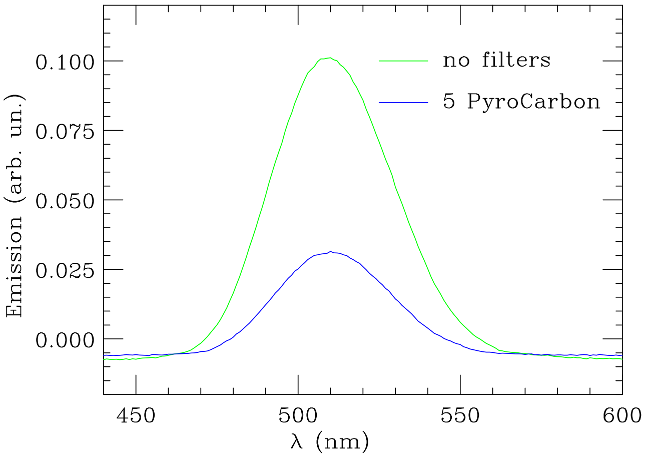

Figure 3.18: Emission band of $Pt_2(P_2O_5H_2)_4{}^{4-}$ under excitation with X-rays not attenuated by filters *(green line)*, and attenuated by 5 mm of Pyrocarbon (density: 2.26 gr/cm^3) *(blue line)*.

To check if the triplet excited state induced by X-rays depends on their energy, and in particular to verify whether or not the process that generates the green emission on the sample is due to the excitation of the Platinum core hole, we masked the energies below and above the absorption edge and recorded the emission spectra (Figure 3.19). From the central panels of Figure 3.19, we can observe an emission spectrum due to X-rays of energy less than the Platinum L_3–edge energy. Therefore, the effect of X-rays on $Pt_2(P_2O_5H_2)_4{}^{4-}$ does not seem linked to the excitation of the Platinum core hole. However, Figure 3.19 shows a relationship between the effect of the X-ray photons and their energy. In table 3.1 we indicate in the first row the values of the integrals IB (normalized to 1) of the total incident polychromatic beam, of the selected beam

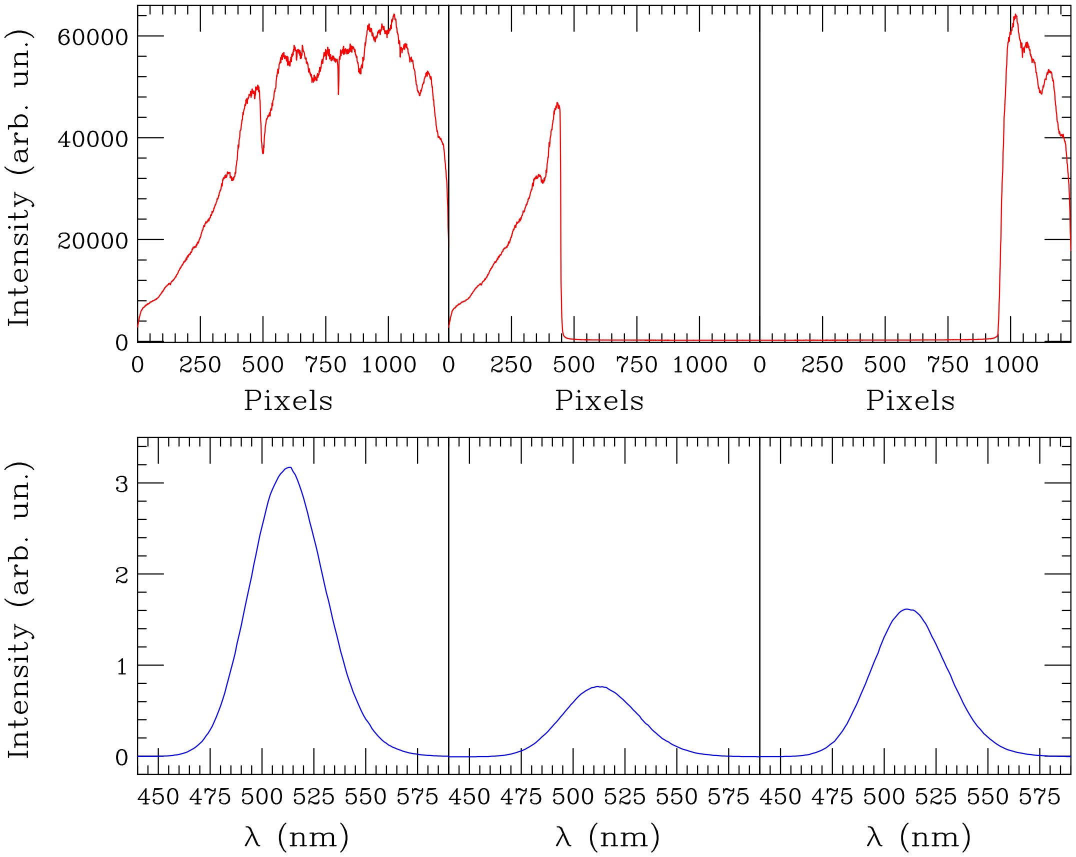

Figure 3.19: The three *upper panels* show the total polychromatic beam diffracted by the crystal in the energy range 11.400 - 11.990 keV (*left*), the beam below (*middle*), and above (*right*) the Pt L_3–edge, respectively. The three *lower panels* show the corresponding emission spectra.

below the edge and of the selected beam above the edge, respectively. In the second row we indicate the values of the integrals IP (normalized to 1) of the corresponding emission bands. In the third row we indicate the ratios IP/IB. If we assume that the phosphorescence depends *only* on the intensity of the X-rays without any correlation with their energy, then IP/IB should be constant in the three cases. Furthermore, assuming that the integrals of the emission band are additive, for the energy region included between below edge and above edge, which is the region just above the Pt L_3–edge, we should have that

$$IB(\text{all beam}) - [IB(\text{below edge}) + IB(\text{above edge})] =$$

$$IP(\text{all beam}) - [IP(\text{below edge}) + IP(\text{above edge})]$$

	all beam	below edge	above edge
IB	1	0.18	0.28
IP	1	0.24	0.51
IP/IB	1	1.3	1.8

Table 3.1: Values of the integrals IB, IP, and ratios IP/IB.

In our case the first term is equal to 0.54 and the second is 0.25 leading to the ratio $IP/IB = 0.46$. This could mean that for a given number of photons the intensity of the emission depends somehow on the energy of the photons, and in particular if the X-ray photons are in the energy region immediately above the core edge, the excitation of the triplet state process seems to be rather inefficient.

Following the negative results of the TR experiment on $Pt_2(P_2O_5H_2)_4{}^{4-}$ we investigated the effect of the X-ray beam on the sample. The conclusions are the following:

i. for a polychromatic X-ray beam the entity of the excitation of the triplet state depends on the intensity of the X-ray beam itself;

ii. the excitation of $Pt_2(P_2O_5H_2)_4{}^{4-}$ due to X-ray beam seems not depend on the core hole excitation;

iii. however, the triplet state depends somehow on the energy of the X-rays, but this experiment is not conclusive on this point.

The effect of the X-ray beam on the sample can be associated to the X-ray Excited Optical Luminescence (XEOL) phenomenon observed in a large number of optically acive systems that are luminescent under X-ray irradiation [35–37].

3.6 Discussion of the results

The result obtained in the TR experiment performed on $Pt_2(P_2O_5H_2)_4{}^{4-}$ was *negative* in the sense that we have not detected a "difference signal" between the excited and the ground state. The explanation of this result is not yet clear. In fact, it seems improbable that the percentage of the excited state was below the detectable threshold (15%) as all the experimental requirements have been fulfilled during the experiment. A possible and most reasonable explanation of this *negative result* could be linked to the effect of the

X-rays on the sample under study. The experiment described in the previous paragraph has shown that the X-ray beam excites the triplet state of $Pt_2(P_2O_5H_2)_4{}^{4-}$, therefore our probe (X-rays) acts as a pump itself, i.e. it is responsible for (or part of) the triplet excited state transition, to which the structural modifications are linked. The effect is dramatic for our task as the sample would be, according to this argument, always in the excited state during the measurements both before and after the laser firing, preventing us from detecting any "difference signal". At first glance, this explanation seems to be in contradiction with the results reported in [8] and with the Pt–Pt distance obtained from our best fit of $k\chi_g(k)$ to $k\chi_{exp}(k)$ (which is the distance reported for the ground state). In fact, if the X-ray beam acts like a pump on the sample, and excites it, there is no reason to find a value for the Pt–Pt distance of the sample in its ground state. Nevertheless, while we cannot compare our result with that in [8] as we do not have enough experimental details, we can claim that our result is not in contradiction with that obtained from the measurements carried out on BM29. In the previous paragraph we showed the effect of the X-ray on the $Pt_2(P_2O_5H_2)_4{}^{4-}$ and we demonstrated that the intensity of the phosphorescence depends on the intensity of the X-ray beam. The photon flux in BM29 in single bunch mode is 10^8 photons/sec whereas the polychromatic beam of ID24 in 2/3 fill mode provides a higher flux of, at least, 4 orders of magnitude. If we compare the two experimental signals $k\chi_{exp}(k)$ of the absorption spectra recorded on BM29 and ID24 (blue and green lines respectively) of Figure 3.20, we clearly observe

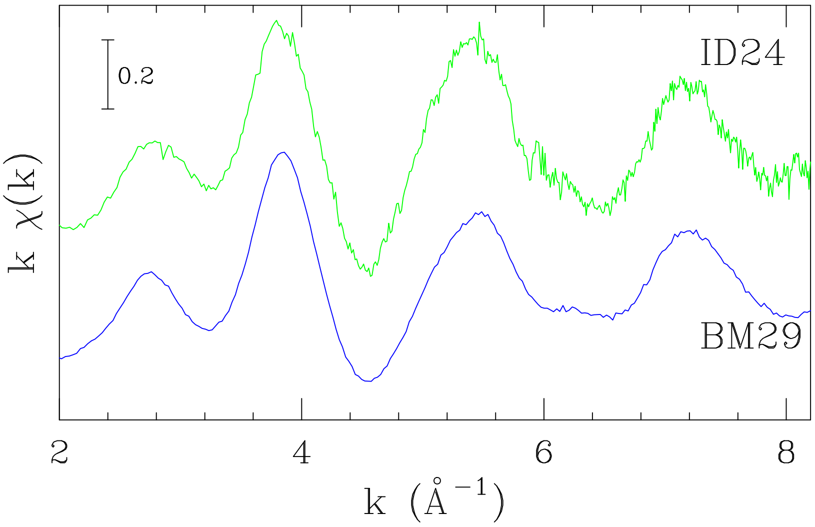

Figure 3.20: $k\chi_{exp}(k)$ signals of $Pt_2(P_2O_5H_2)_4{}^{4-}$ recorded on BM29 in single bunch mode *(blue line)* and recorded on ID24 *(green line)* in 2/3-fill mode.

that in the k region around 6 Å^{-1} the features of the two spectra are different and qualitatively the signal of the spectrum recorded on ID24 is comparable to the simulated $k\chi_{m(x)}(k)$ with x $\sim$ 0.7. This comparison strengthens our thesis according to which an intense X-ray beam excites the triplet state of $Pt_2(P_2O_5H_2)_4{}^{4-}$ and is not a suitable probe as it behaves as a pump itself. We therefore conclude that this effect prevented us to detect a structural modification in the sample before and after the laser firing in the TR experiment at ID24.

This explanation could be troublesome. In fact, we require high flux in order to be able to collect a complete dataset, with good statistics below the millisecond time resolution; yet, at the same time, we must consider the possibility that our probe can interfere with the sample. This effect, if present, must be minimized as much as possible.

Part II

High-pressure studies

Chapter 4

Why high-pressure studies?

This chapter introduces the second part of this work, and it concerns high-pressure studies. The reason why the study of condensed matter at high-pressure is a relatively new field is exposed, as is the motivation and importance of understanding the behaviour of matter under, so called, "extreme conditions".

4.1 High-pressure physics in the past

Of the common thermodynamic variables pressure and temperature, it is temperature that has played by far the most prominent role in probing condensed matter and in our fundamental understanding of it. HP studies have been considered in the past by physicists as a marginal field of investigation. HP conditions were often described as "exotic" or "extreme", and a very small community of physicists explored them, more for the technological performances than for the physical information. In fact, HP research was more the domain of geophysicists and solid state chemists. However, even as far back as 1660, Robert Boyle declared in his famous treatise commonly known as *Touching the Spring of the Air* that "perhaps the pressure of the air might have an interest in more phenomena that men have hitherto thought". Indeed, this lack of interest in the thermodynamic parameter pressure might seem strange, as one of the main goals of fundamental physics of condensed matter is the understanding of the properties of matter as it exists actually in the universe. Most of the condensed matter is inside the planets at pressures of several tens of GPa and the "ordinary" conditions are not at all ordinary. Furthermore, of all physical variables, pressure possesses one of the greatest ranges: over 60 orders of magnitude [38]. At the high end, the pressures are those of the interiors of neutron stars; at the other, they gauge conditions of the remotest vacua of outer space.

There is more than one reason for which HP studies are a relatively new field. The first reason, and maybe the least important, is related to the HP generation devices: heavy, difficult to use and expensive up until the end of the 60s. The second issue that has prevented the development of the HP physics was the quality of the results and the difficulty in monitoring the pressure conditions. The third reason was the poor agreement between theoretical calculations and experimental results. Nowadays, thanks to developments of different HP generation devices such as DACs and LVCs in combination with the availability of international facilities such as SR and neutron sources, it is possible to perform relatively easily high quality HP experiments exploiting different techniques. The theoretical methods as well, have experienced a remarkable improvement: *ab initio* calculation methods are able now to describe fairly well a system without any experimental input, allowing a closer interaction between theory and experience.

4.2 Matter under "extreme conditions"

It is through pressure, which is a special case of generalized stress, that one can change the volume of a system or the average particle density. The changes may be brought about in a quasi-static way, typically nowadays by the use of DACs, or they may be brought about dynamically, through the use of shock methods [39, 40]. In either case, the atoms in condensed forms of matter are driven closer together. As observed by Percy Williams Bridgman (Nobel Prize in Physics in 1946) of Harvard University in 1926, this compression offers a route to "breaking down" the electronic structure of the atoms themselves and to the possibility of creating entirely different bulk properties. Through application of pressure, we can bring about one of the most basic of all changes, the crossing of the "great divide" from insulators to metals (examples of recent works are [41,42]). Pressure-induced insulator-to-metal transitions have been documented in a long list of materials and over a broad range of pressures. One of the most well studied of these materials is Silicon, which transforms from the diamond-type semiconductor phase to the metallic β-Sn structure at 12 GPa [43–47].

If we hold macroscopic quantities of a pure element, for example, in a volume V, a consequence of this confinement boundary condition is that the stationary states of the fundamental Schrödinger equation

$$\mathcal{H}\psi(V) = E(V)\psi(V)$$

are clearly functions of volume V and hence alterable by pressure. In solids, described by the energy-band picture, pressure can alter both bandwidths and bandgaps [48], and offers a way to refine both—that is, pressure acts as a probe of band structure. Moreover, the stationary states of the Schrödinger equation can also be electronically ordered, exhibiting magnetic states or superconducting states, for example. Pressure can change the magnetic state [49], or the properties of superconductors [50], and is a revealing diagnostic tool.

Pressure induces myriad changes in materials. First, compression typically causes a tendency toward the closer packing of the atoms, ions and molecules. Although this is often assumed to mean a corresponding tendency toward simpler structures, sometimes quite the opposite is true. Indeed, pressure may induce order, but it also can bring out disorder [51]. Generally, a compression is followed by an increase of the local coordination number; this increase in turn is intimately linked to changes in electron hybridization. Such changes can be associated with major changes in electronic and magnetic states, including the formation of conductors or superconductors from materials originally possessing substantial bandgaps. Finally, in various ways such changes all affect chemical behaviour: pressure can induce chemical reactions that do not occur under more familiar conditions [52], and it can speed up or slow down known chemical reactions. Although many of these effects of pressure on condensed matter have been known for years, as already pointed out, it is only recently that the full potential of the pressure variable in the condensed matter sciences has begun to be realized. This change is mainly due to striking advances that have occurred in parallel in experimental HP techniques and in theoretical methods respectively.

Chapter 5

High-pressure experimental methods

This chapter briefly surveys the apparatus for high-pressure studies used in this work. It describes the principle of the diamond anvil cell and related equipment. It examines the issue of non-hydrostaticity and describes the most common pressure measurement methods.

5.1 Diamond anvil cells

Among the numerous HP cells now available, such as large volume cells, multi anvil cells, etc. (for an exhaustive review see [53]), the DAC allows to reach the highest static pressures. The first DAC was designed and constructed at the National Bureau of Standards [54]. The great number of results in the field of HP research is strictly related to the development of the DAC technique; see for example [55] for a review of early developments. This device, that can fit into the palm of the hand, can generate pressures of the order of magnitude of 500 GPa (5 millions times the atmospheric pressure) [56]. The DAC is very simple in principle. It consists of two gem-quality single crystal diamonds with flat surfaces to serve as anvil faces (Figure 5.1). The diamonds are mounted so that a sample can be squeezed between the anvil faces. The smaller the area A of the anvil faces, the higher the pressure P reached by the DAC for an equivalent value of applied force F, according to the well known relationship $P = \frac{F}{A}$. To apply pressure to the sample, the anvil faces must have a high degree of parallelism. One of the diamond anvil is usually mounted on the end of a sliding piston, while the other is

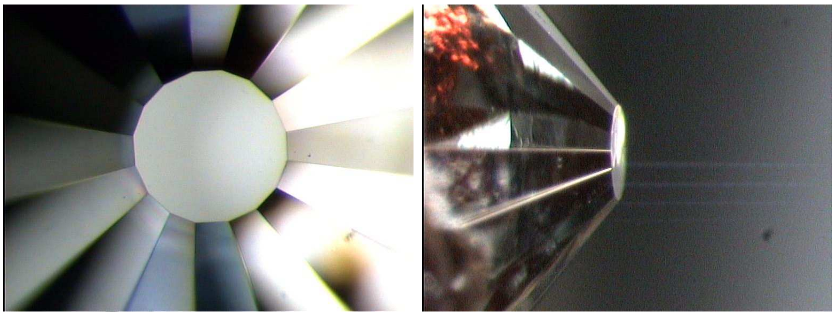

Figure 5.1: Diamond anvil from top and from side.

stationary. A cylinder guides the piston so that the anvil faces meet very precisely. The piston is pushed by a mechanical device such as a screw or a small hydraulic ram, thus driving the two anvils together. A rocker or a tilting plate directly under the diamond anvils allows orientation of the diamonds to be adjusted so that the faces are concentric and parallel. The adjustment procedure is made under the microscope: the concentricity is achieved moving the support of the piston diamond slightly to superimpose the two polygons corresponding to the faces of the anvils; the parallelism is checked by observing the interference fringes that appear when the two anvils are not parallel. Figure 5.2 shows the principle of DACs.

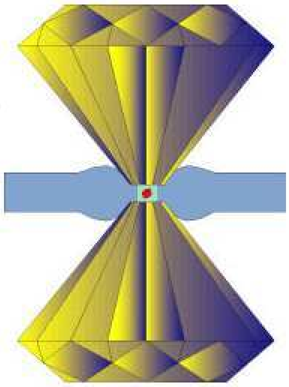

Figure 5.2: The principle of the diamond anvil cell.

A membrane DAC has been used for the experiments presented in this work. A picture of the cell is shown in Figure 5.3 [57]. In this type of cell the pressure on the sliding piston results from the deformation of a thin membrane by effect of a He pressure [58]. This allows a homogeneous distribution of the force applied on the membrane and a fine pressure control. This type of cell allows changing of pressure in small steps enabling, for

Figure 5.3: Chervin-type DAC.

example, careful observation of sample behaviour at a phase transition. Moreover, the possibility to change the pressure on-line without the need of moving the cell makes the Chervin-type DAC particularly suited for experiments using SR where the alignment of the sample is a delicate and sometimes long procedure.

While most of the experiments using DACs have been performed at RT, two heating techniques in the DACs have been developed to achieve simultaneous HP and HT conditions: resistive heating and laser heating. For the resistive heating two methods are possible: internal and external heating. In internal heating a furnace is placed in the cavity just around the diamond anvils. For external heating the most straightforward method is to place the DAC as a whole in a furnace, which can be typically a resistive heated metallic cylinder as the one shown in Figure 5.4.

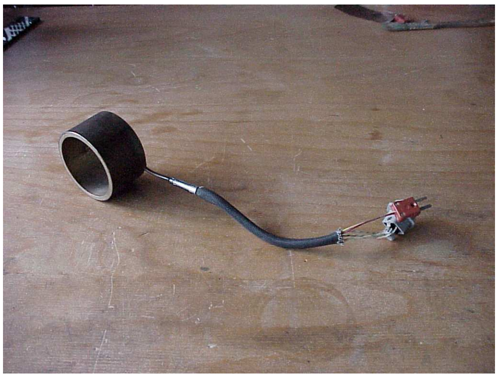

Figure 5.4: External heater for Chervin-type cell.

This method yields a very uniform temperature field and allows to reach temperatures up to 600 K. For higher temperatures, the whole system must be enclosed in a vacuum chamber to avoid graphitization of the diamonds. Higher temperatures can be reached combining internal and external heaters. Other methods consist in embedding heaters and temperature sensors on the bevel of diamond anvils. For more details about heating in DACs, refer to [53].

5.2 Gaskets

When the sample is placed between the anvil faces, as the anvils are forced together, the sample is trapped and develops a uniaxial pressure, whose distribution ranges from a maximum at the center to essentially zero pressure at the edge of the sample area [59,60]. In order to have an isotropic pressure distribution the sample must be embedded and confined in a PTM softer than the sample. To encapsulate the sample and the hydrostatic medium, both are placed in a small hole drilled in a metallic gasket (Figure 5.5).

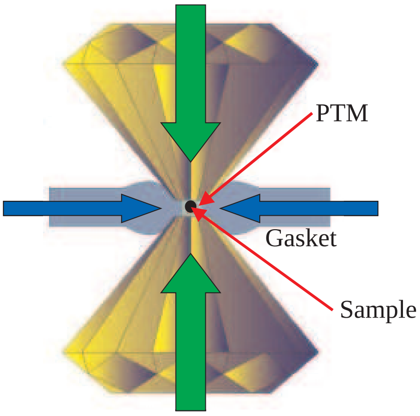

Figure 5.5: The use of a PTM and of a gasket to encapsulate sample and PTM allows to overcome the uniaxial pressure generated by the diamonds and to have an isotropic pressure.

The gasket consists of a metallic foil of typically 200 μm of thickness. To increase the hardness of the metal, the foil is placed between the two diamonds and is pre-indented to about 30-60 μm (Figure 5.6). The higher the pressure that has to be achieved during the experiment, the higher the pre-indentation pressure and the smaller the final gasket thickness (and sample volume). A hole in the pre-indented gasket is then drilled by electro-erosion. The diameter of the hole depends critically on the diameter of the diamonds, and it is typically one third the diameter of the flat of the diamond.

Table 5.1 shows typical values of maximum pressures to reach and corresponding values of diameters of anvils flats and gasket holes to use.

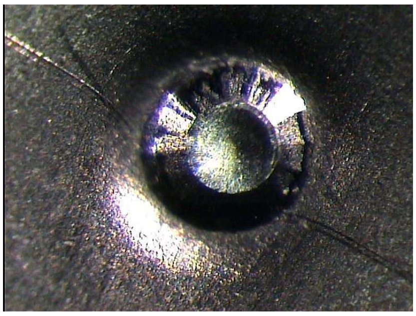

Figure 5.6: Pre-indented stainless steel gasket.

P_{max} (GPa)	Ø flat (μm)	Ø hole (μm)
30	600	200
60	300	100
100	150	50

Table 5.1: Typical values of maximum pressures to reach and corresponding values of diameters of anvils flats and gasket holes to use.

A second purpose of the gasket is to provide support at the edges and sides of the anvils thus preventing failure of the anvils at very HPs. In this work stainless steel and Rhenium have been used as gasket materials for RT and HT measurements respectively.

5.3 Hydrostaticity and pressure transmitting media

The uniaxial compression of diamonds acts directly on the media that transmit hydrostatic pressure to the sample. If the PTM solidifies, the hydrostatic conditions inside the cell volume are no longer achieved and the sample is subject to a pressure gradient: i.e. the stress is not uniform in all directions. The variation of stress conditions at different points in the sample depends upon the strength of the PTM. It is desirable to eliminate or reduce the pressure anisotropy and inhomogeneity in some HP experiments. This can be achieved by choosing a soft PTM. The hydrostatic limits of several PTM were determined [61] by using the ruby line broadening (see paragraph 5.4), or by measuring the pressure homogeneity with several ruby chips over the area of the gasket aperture. The PTM must not chemically react with the sample and must not interfere with the measurement of the sample. For example, in a XAS experiment, it must not have an absorption edge in the energy range of interest. In our experiments we have used different PTM depending on the type of measurements.

- **Silicone oil** Liquid up to 5 GPa and quasi-hydrostatic up to 13 GPa. Very easy to load. Contrary to other PTM, Silicone oil increases its viscosity gradually with increasing pressure.
- **Nitrogen** Cryogenically loaded, it is quite soft up to 16.5 GPa, at which it undergoes a phase transition.
- **4:1 Methanol-Ethanol** Liquid, and remains hydrostatic up to 10 GPa at room temperature [61], above which it undergoes a glass transition.
- **LiF** and **NaCl** These salts were used for XRD measurements at HT. In fact, these two solid PTM soften and reduce pressure anisotropy and inhomogeneity when heated. For XRD measurements these PTM can be used as pressure gauges as well by following their diffraction peaks as a function of pressure.

A more complete description of different PTM is given in [53].

5.4 Methods for measuring pressure

Several methods for measuring pressure have been developed. If the experimental technique is *in situ* XRD, then the diffraction pattern of an internal standard such as NaCl or Au, can be obtained along with that of the sample. The pressure is then determined from the lattice parameters calculated from the diffraction pattern. Another means of measuring the pressure is the ruby fluorescence method. This method is particularly well adapted to DAC technology since it exploits the high transparency of diamonds to visible light. Forman *et al.* in 1972 [62] first showed that the luminescence doublet of peaks R_1 and R_2 of Cr^{3+}-doped Al_2O_3 (ruby lines) shift linearly with hydrostatic pressure in the range of 1–22 kbar, and that the two lines broaden if the ruby experiences nonhydrostatic stresses. In this method [63] a tiny chip of ruby (5-10 μm in dimensions) is placed in the pressure medium along with the sample (Figure 5.7), and its luminescence is excited by a laser. The shift in wavelength is followed as a function

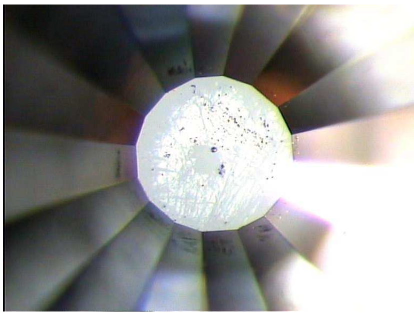

Figure 5.7: Ruby on a face of a diamond anvil.

of pressure. An important question with regard to the ruby scale is how far it is linear [64–68]. According to [69], the relationship between the pressure P (in GPa) and the ruby R_1 line wavelength shift $\delta\lambda$ (in nm) can be described by (5.1) (at 20 °C),

$$P = \frac{1904}{B}\left(\left(\frac{\delta\lambda}{694.24}\right)^{B} - 1\right). \tag{5.1}$$

where the parameter B is equal to 7.665 and 5 for quasi-hydrostatic and non-hydrostatic conditions respectively. Note that the position of the ruby luminescence lines varies with temperature, with a slope of 0.068 Å K^{-1}, which means that a ΔT of $\sim$ 5 K produces the same shift as the application of a pressure of 0.1 GPa. Therefore a variation of temperature from the standard 20 °C has to be taken into account for a precise determination of pressure. Temperature correction of the ruby pressure scale was systematically studied by Vos and Schouten [70].

The ruby gauge has some disadvantages: the luminescence spectrum exhibits a doublet instead of a single line that is desirable for exact pressure determination; rubies provide low accuracy in the low pressure region ($\sim$ 1 GPa) and their luminescence becomes weak at megabar pressures. These limits have motivated a search for other fluorescent compounds which would be more adequate for both very HP and HT studies in the DACs. $SrB_4O_7{:}Sm^{2+}$ is a very good candidate to serve as a substitute for rubies in both very high-pressure (in the megabar range) and high-temperature (up to 900 K) [71–73]. The main advantages are the following:

i. the singlet character of the fluorescent line which is conserved at above 100 GPa;

ii. the lower decrease of intensity under pressure.

Chapter 6

X-ray absorption spectroscopy and high-pressure

This chapter starts with a brief review of a selection of previous X-ray absorption spectroscopy studies at high-pressure. Essentially, three topics are surveyed: ionic systems, semiconductors, and combined high-pressure and high-temperature studies. The following sections all deal with more technical aspects of high-pressure X-ray absorption spectroscopy and mainly serve as framework for the topics developed in Chapter 7. First, a survey of the most active synchrotron radiation beamlines in high-pressure X-ray absorption spectroscopy is given, covering second and third generation sources, as well as planned synchrotron radiation sources. After this very general introduction, the topic concentrates on high-pressure X-ray absorption spectroscopy using diamond anvil cells, focusing on the main experimental prerequisites necessary for such studies. Finally, the principle of the energy-dispersive spectrometer is briefly described, pinpointing the advantages of this setup for experiments using diamond anvil cells.

6.1 Survey of XAS studies at HP

XAS is a common and powerful technique to investigate structural parameters such as the geometry of bonding, oxidation numbers, coordination state, and bond lengths in molecules and condensed matter. It has undergone important theoretical and experimental developments in the last years also thanks to the availability of SR sources. In particular the high-brilliance third generation SR sources have opened up new opportunities for the study of condensed matter under extreme conditions of pressure and/or temperature. Its possibility to give information on the local structure (EXAFS) and on electronic properties (XANES) makes it very complementary to XRD, which is by far the predominant HP technique for structural studies involving SR.

The first published XAS study at HP using SR took place at Stanford Synchrotron Radiation Laboratory and dates to 1978 [74]. The group of Ingalls presented HP measurements on bond compressibility and atomic spacing in FeS_2 and FeF_2, stressing particularly the wide applicability of the technique for studying the effect of pressure on chemical bonds.

In the succeeding years, in assessing the suitability of EXAFS for HP structural investigations, the same group examined the sensitivity of the technique to detect structural and/or electronic changes induced by pressure as well as the method of pressure generation itself. Simple materials whose bond compressibility was known, such as NaBr, Ge [75] and CuBr [76] were studied at HP. At that time, HP XAS experiments were performed using point-by-point energy scans, which did not allow the possibility of easily avoiding Bragg peaks in the absorption spectrum originating from diffraction by the diamond anvils commonly used for HP studies. For this reason, diamond anvils were replaced by boron carbide (B_4C) anvils. However, in so doing, the use of the state-of-the-art ruby fluorescence pressure calibration technique was precluded because boron carbide is not transparent to visible light. This prompted to search for pressure markers [76] that, mixed with the sample, could give a way of determining pressure (like, for example, Copper [77]).

By using the same technique the same group continued with the investigation of the behaviour as a function of pressure of alkali-metal halides: NaBr, KBr, and RbCl [78]. The interest of several group in these ionic compounds has more recently increased the number of works on these systems using EXAFS at HP [79–83], and in combination with HT [84, 85].

A substantial body of EXAFS studies at HP on semiconductors exists in the literature. This is probably due to the fact that the study of semiconductors at HP represents one the most fertile fields of HP research since the 60s. A brief overview of XAS applied to pressure-induced transformations of semiconductors can be found in [86]. Most of these studies were performed using the energy-dispersive optics setup at LURE (BL D11) [87, 88] and, more recently, at ESRF (BL ID24) [89]. All of these experiments were carried out in the transmission geometry with the X-ray beam going through the diamond anvils. One of the first works dates to 1989 and concerns the study of GaP [90] up to 36 GPa. The room temperature equation of state of phase I was determined and the transition from a four-fold to a six-fold coordination scheme was observed at 26 GPa. After this work other III-V semiconductors have been investigated (GaAs [91], GaN [92], GaSb [93], InAs [13]), as well as II-VI semiconductors (ZnTe [94], HgTe [95] and ZnSe [96]).

HP techniques based on the use of the Paris-Edinburgh large volume cell, originally developed for neutron scattering [97] and XRD experiments [98, 99], have been extended also to XAS [100]. This pushed many studies at combined HP and HT using XAS to examine the pressure and temperature effect on the anharmonicity of the pair potentials [84, 101], to extend the phase diagram in unexplored pressure-temperature regions [85, 102, 103], or to study the melting of semiconductors under pressure [86]. The unique short-range sensitivity of XAS and the setup using the Paris-Edinburgh large volume cell made the study of liquids under pressure a growing field of research [104–108].

6.2 HP XAS stations worldwide

SR provides a powerful high-energy beam for penetrating the strong wall of pressure vessels. The high-brilliance, low-emittance beams are ideal for focusing to micron-sized dimensions to probe minute samples at HP. Although XRD is the predominant HP technique involving SR, because it provides a means for identification of new HP phases, XAS applied to HP has been flourishing at synchrotron facilities. The development of HP XAS was hindered in the past by insufficient intensity and opaqueness of HP vessels below 10 keV. Many second generation SR sources however, have XAS stations devoted to HP studies, and the advent of third generation sources with their higher brilliance is opening the field of HP XAS:

i. at lower energies (below 8 keV),

ii. above 100 GPa,

iii. to dilute systems.

A brief survey of some of the most active SR beamlines at second and third generation sources is given below.

Second generation SR sources

At LURE (*Laboratoire pour l'Utilisation du Rayonnement Electromagnétique*, Orsay - France), the DCI storage ring delivers photons of energy range from 5 to 50 keV. The XAS station that has HP studies as an important research topics is D11. D11 is analogous to the ESRF beamline ID24, except for the fact that it is coupled to a bending magnet source. The setup of the optics has been described in detail in [88]. The smallest focus size achievable, $\sim 500\ \mu$m, limits the maximum pressure. Up to the present day, most of the HP XAS studies using DACs have been performed at this beamline [90–93, 103, 109–113].

At SRS (*Synchrotron Radiation Source*, Daresbury - UK), station 9.3 was built as facility for Materials Science experiments. The wiggler source enables experiments in the range of 6-40 keV. Thanks to the high flexibility of this station several setups are available. The energy dispersive optics setup gives a uniform and small focal spot size (150 μm). This setup is used to study fast chemical systems and has also been used for HP XAS studies [114]. This station has the possibility to combine EXAFS and powder diffraction measurements for HP studies [115].

At Photon Factory (National Laboratory for High Energy Physics, Tsukuba - Japan), at the bending magnet XAFS station BL-10B, the absorption spectra are recorded using a fixed exit double crystal monochromator. The beam size is 5 to 10 mm (H) × 0.5 to 2 mm (V) (FWHM). This station has been used for HP-HT experiments for the study of semiconductor-metal transition in As-Se mixtures [104] and for the study at HP of glasses [116, 117] using multi-anvil apparata. The other XAFS station BL-13B is a multipole wiggler beamline, the beam size is ~ 5 mm (H) × ~ 1.5 mm (V) (FWHM). HP and combined HP-HT experiments have been performed using multi-anvil apparata and after having slitted the beam size to typically 0.5×0.5 mm^2 [82, 83, 106, 118, 119].

Since the pioneering work of the Ingalls group in 1978 on HP studies using XAS, at the SSRL (*Stanford Synchrotron Radiation Laboratory*, Stanford - USA) the research in this field has continued until recently [75–77, 80, 81, 120–126]. All the referred experiments have been performed using boron carbide anvils at the wiggler side-stations 4-1 and/or 4-3. Both stations are standard scan EXAFS beamlines. The beam size at the sample is 2 mm (V) × 20 mm (H) (station 4-1) and 0.15 mm (V) × 20 mm (H)

(FWHM) (station 4-3).

Third generation SR sources

Recently, the third generation SR sources have greatly boosted the flux intensity and reduced spot sizes, allowing XAS to look into properties of matter at increasingly higher pressures.

The general purpose XAFS beamline (BM29) of ESRF (Grenoble - France) and the two XAFS spectrometers (BL01B1 and BL14B1) at SPring8 (*Super Photon ring-8 GeV*, Nishi Harima - Japan) have similar characteristics; all being built on bending magnets. At SPring8, two mirrors are used for harmonic rejection and for beam focusing (vertical beam size at the sample ~ 0.2 mm), whereas on BM29 the harmonic rejection is achieved by detuning the monochromator and the beam size is reduced by a slits system. The HP research in these stations is largely concerned with the structural studies of matter using multi anvil apparata at RT [127], and combined HP-HT conditions [84, 85, 101, 102, 107] using LVCs. At SPring8 HP experiments using DACs carrying anvils with 0.6 mm flats up to moderate pressures are performed as well [128, 129].

The spectrometer installed by the French Collaborative Research Group on the BM32 beamline at ESRF is also coupled with a bending magnet. The beamline setup includes a vertically focusing system and a sagittaly focusing double-crystal monochromator which provide a 0.2 mm × 0.2 mm X-ray beam. This setup has allowed XAFS experiments at HP [105, 130, 131].

Still to come SR sources

As far as the third generation SR sources to be built are concerned, the EXAFS beamline of DIAMOND (Chilton - UK) will be coupled with a bending magnet source, the focused beam size is foreseen to be 15 μm (V)× 1 mm (H) FWHM. Out of the wide and multidisciplinary research programme this beamline will support also a HP research programme using sample environments similar to the ones used at ESRF (BM29) and Spring8 (BL01B1) such as LVCs in order to investigate the structure of HP melts.

At SOLEIL (Orsay - France), the new French SR source, the energy dispersive EXAFS beamlime will be in operation in 2006. This beamline will be built on a dipole source, the focal point is foreseen to be 40 μm × 40 μm. This will allow to perform HP studies using LVCs and DACs.

6.3 Main requirements for HP XAS studies using DACs

The main requirements for HP XAS studies are the following:

1. **Small focal spot**

   Typically, the diamond anvil flats required to reach pressure of 50 to 100 GPa range between 300 and 150 μm respectively (see table 5.1) . Gasket hole diameters are typically one third the size of the diamond flat, i.e. 100 μm and 50 μm respectively and sample sizes range between 80 μm and 30 μm. The required focal spot dimensions for applications in the 100 GPa region are therefore limited to 20–30 μm.

2. **Position stability of focal spot in whole energy range**

   Contrary to XRD, a large energy range is required to collect a XAS spectrum. It is of paramount importance that the position and intensity of the focal spot remain stable throughout the whole acquisition process.

3. **High flux**

   The most common geometry for HP XAS measurements using DACs consists in the X-ray beam traversing the two diamonds. The thickness of a diamond anvil required to reach 100 GPa is of the order of 2 mm. This poses real problems for low energy XAS ($E < 8$ keV). The transmission of 4 mm of diamond falls below 2×10^{-3} for $E < 8$ keV, making measurements at 100 GPa rather prohibitive on bending magnet sources. In order to avoid this problem, several solutions are being attempted, with the development of exotic diamond anvils (with holes drilled in the central part to reduce effective diamond thickness) or by avoiding the path through the diamonds by orienting the cell perpendicular to the beam direction to exploit the lower absorption of low Z gaskets (i.e. Be) [132, 133].

4. **Absence of Bragg diffraction peaks in the energy range of interest**

   Bragg diffraction from the diamonds is inevitable, and leads to intense positive peaks superposed on the absorption spectrum, at energy values that match the Bragg condition on the intercepted crystalline planes of the 2 diamond anvils [134].

6.4 Dispersive XAS for HP

Historically, energy-dispersive spectrometers were developed for TR EXAFS studies to monitor dynamical processes. However, compared to the conventional point-by-point approach, recording X-ray absorption spectra in a dispersive mode takes advantage of several features that make this method ideal for HP studies. The energy-dispersive spectrometer in conjunction with the high brilliance X-ray beams of third generation synchrotron sources are particularly suited for HP studies using DACs, and fulfil all the technical prerequisites described in paragraph 6.3.

The dispersive XAS concept is illustrated in Figure 6.1. A quasi-parallel and polychromatic beam, supplied by a SR source, is dispersed and focused by an elliptically curved crystal [2, 3]. Because the incident X-rays strike the crystal at slightly different angles along its length, the bent crystal acts as a polychromator diffracting a different energy at each point. This energy-dispersed beam converges to a focal point at the

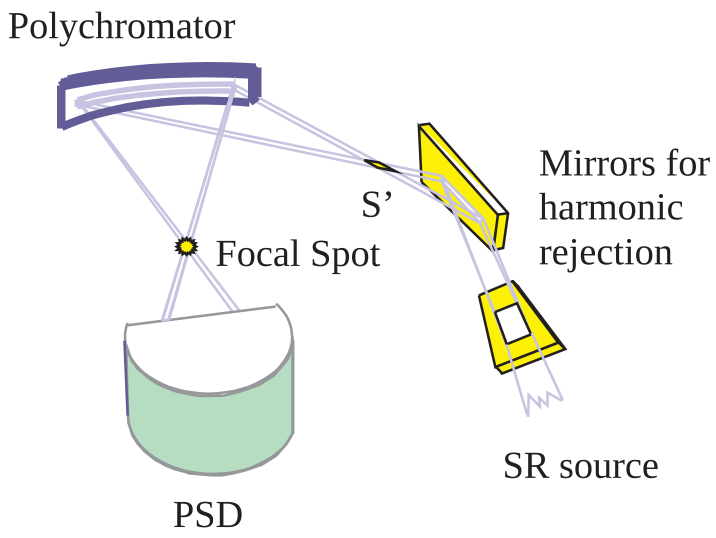

Figure 6.1: Scheme of the dispersive XAS concept.

sample position. The beam, transmitted through the sample position, then diverges towards a PSD. The position of the beam, incident in the detector, can be directly correlated to energy. The X-ray absorption spectrum is obtained by taking the logarithm of the ratio of I_0 data and I_1 data, where I_0 and I_1 are spatial X-ray intensity distribution in the absence and presence of the sample, respectively. Harmonic rejection, which is crucial for samples in highly absorbing environments, is achieved using a system of mirrors placed before or after the polychromator. In order to produce reliable, accurate structural data, the EDXAS optics must be capable of delivering a wide bandpass (ΔE) of radiation maintaining an adequate energy resolution δE/E. A more complete description of the principle of dispersive optics is given in Appendix A.

To summarize, the absence of mechanical movements of the energy-dispersive spectrometer during the acquisition of spectra and the strongly focusing polychromator crystal yield the required spot stability and dimensions respectively for HP studies using DACs. Instabilities of the energy scale and misalignment of the beam with respect to the aperture of the gasket are therefore strongly reduced. Residual effects are to be attributed uniquely to electron beam instabilities from the storage ring. Moreover, in the dispersive setup the transmitted spectrum in the whole energy range is visualized in real time on a PSD. This allows the detection of energy position of diffraction peaks from the anvils, and to shift them until they disappear from the energy region of interest by changing the orientation of the diamonds.

Chapter 7

Technical developments on ID24

This chapter starts with the description of the third vertically refocusing mirror recently implemented on ID24. This technical development, together with the implementation of a fast local feedback (described in Appendix B), have opened new opportunities for X-ray absorption spectroscopy at high-pressure. The section 7.2 concerns some of these new opportunities whose development has been part of the technical work of this Thesis: mainly i) the feasibility test of X-ray absorption measurements in the low energy domain ($E < 8$ keV) at high-pressure and the application to the scientific case of the study of hematite up to 100 GPa, ii) a newly commissioned setup for the combined acquisition of energy-dispersive X-ray absorption spectra and angle-resolved X-ray diffraction patterns at high-pressure, and iii) the commissioning of a new heated diamond anvil cell for high-pressure/high-temperature studies.

7.1 Third refocusing mirror

A third mirror has been added to the optical configuration in 2000. It is installed on the polychromatic beam between 0.3 and 0.6 m upstream the focal point [89]. It consists in a SiO_2 ingot of dimensions 170 mm × 30 mm × 8 mm mounted on a mechanical bender [135]. Figure 7.1 illustrates a photograph of the mirror on its bender. The mirror and its bender are installed in a vacuum chamber (Figure 7.2) which can be easily inserted and aligned on the beam for experiments that require a small vertical focal spot, such as HP experiments.

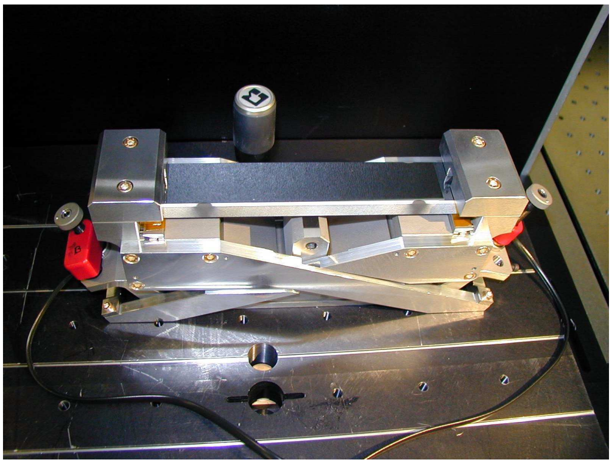

Figure 7.1: The third refocusing mirror mounted on its bender. The two picomotors are visible at the two extremes (in red).

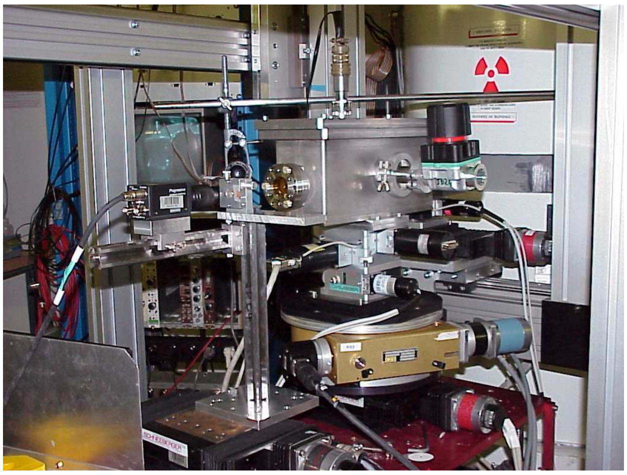

Figure 7.2: The vacuum chamber of the third refocusing mirror. The chamber is installed downstream the polychromator, at about 0.5 m from the sample.

The polychromatic fan is reflected downwards at a variable glancing angle (in general, between 3 and 4 mrad). Two identical mirrors (each with its bender and vacuum chamber) with different coatings – Pd and Pt – are available in order to cover the whole energy range available on ID24. Figure 7.3 shows calculated reflectivity curves for the two coatings with glancing angle of 3 and 4 mrads. The illuminated length of the mirror is 130 mm, allowing to intercept between 400 and 500 μm of direct beam. Measured

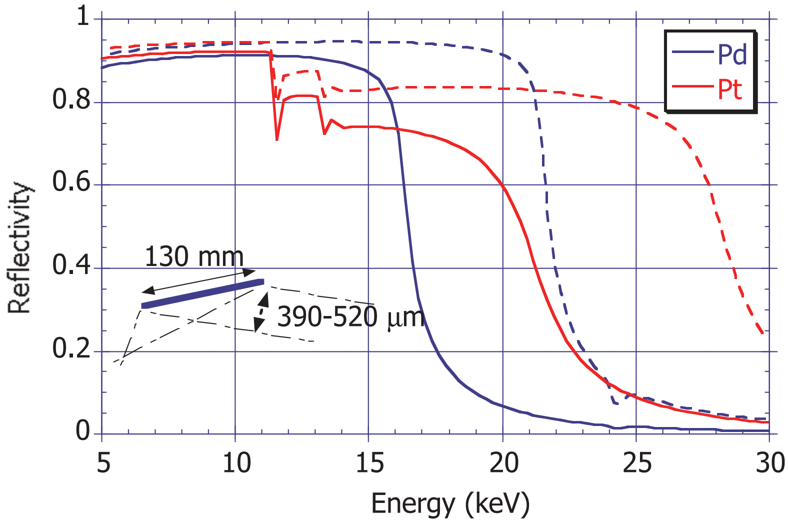

Figure 7.3: Calculated reflectivity curves for the Pd and Pt coatings for glancing angles of 3 (*solid line*) and 4 mrad (*dashed line*) respectively. The illuminated length of the mirror is 130 mm, allowing to intercept between 400 and 500 mm of direct beam with glancing angles of 3 and 4 mrads respectively.

slope errors and micro-roughness for the two coatings are of the order of 1 μrad and 1 Å respectively. The horizontal dimensions of the fan of radiation vary along the surface of the mirror, and are typically around 10-15 mm and 5-10 mm at the entrance and exit windows of the vacuum chamber respectively. An optimum alignment of the surface of the mirror in the direction perpendicular to the plane of reflection has to be performed in order to intercept the whole energy fan at the same glancing angle. An elliptical shape is obtained by applying two moments at the extremes of the mirror using a pair of picomotors. An X-ray camera positioned on the focal spot records images of the beam during the procedure of optimization of the shape of the ellipse. Figure 7.4 shows a typical example of the vertical profile of the reflected beam, compared to that of the direct beam. A Pd coating was used at a grazing incidence angle of 4 mrad and a distance from the focal spot of 0.5 m. The average energy of the beam was $\sim$ 7 keV. Figure 7.4 shows that a substantial reduction in spot size is achieved, from 300 μm to less than 20 μm in most cases. The gain in peak intensity is of the order of 10-20, depending on the shape of the direct beam and on the grazing incidence angle used.

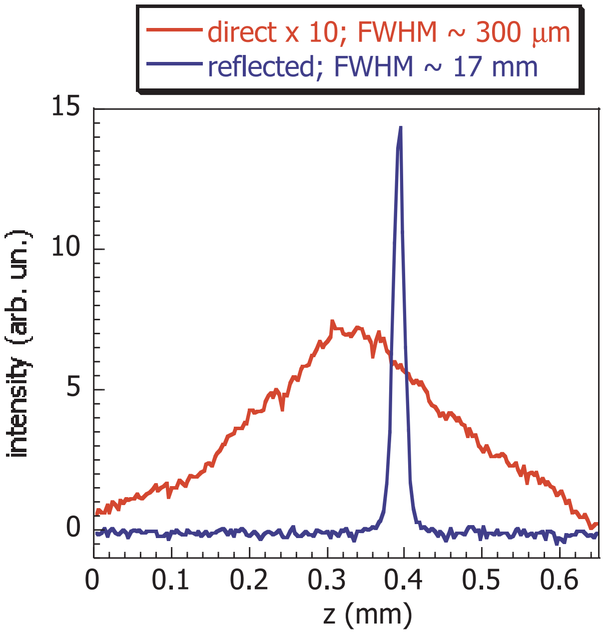

Figure 7.4: Example of the vertical profile of the reflected beam (*blue*), compared to that of the direct beam (*red*). A Pd coating was used at a grazing incidence angle of 4 mrad and a distance from the focal spot of $\sim$ 0.5 m. The average energy of the beam was $\sim$ 7 keV.

7.2 New opportunities for HP XAS

The implementation of the third mirror together with the local feedback (see Appendix B) have opened new important opportunities for HP studies.

- The improved stability has led to an improvement of the quality of the data. This is more evident on non-homogeneous samples (i.e. powder samples).
- The reduced vertical spot size has led to an important increase in flux. The presence of the third mirror has an indirect beneficial effect also on beam stability: the dimensions of the beam on the sample are not limited with the use of slits (as it was before the installation of the third mirror), which largely amplify instability effects.

7.2.1 XAS at high-pressure below 8 keV

The access to the absorption edges at energies below 8 keV is a non trivial problem, due to the strong absorption of diamonds at such energies. To reach pressures of the order of 100 GPa, it is necessary to use diamonds of thickness of ∼ 2 mm. Figure 7.5 shows the transmission of 4 mm of diamond. The transmission at the Fe K-edge is ∼ 10^{-4}.

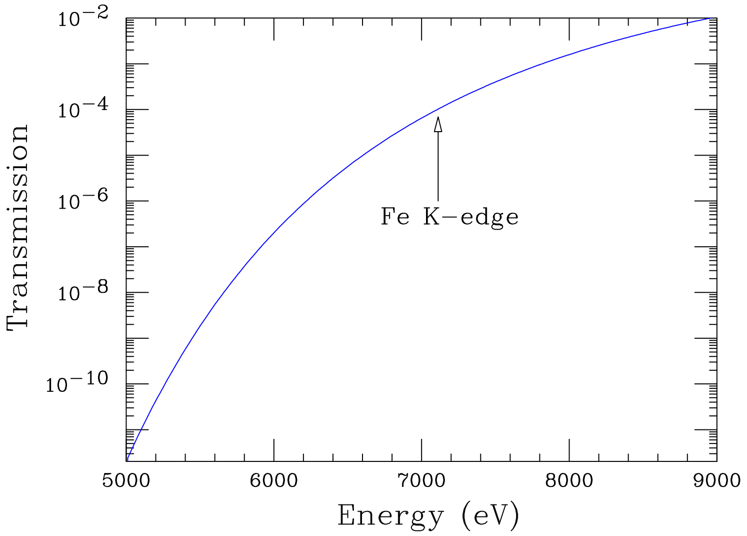

Figure 7.5: Transmission of 4 mm of diamond at energies between 5000 eV and 9000 eV.

XAS on hematite (Fe_2O_3) up to 100 GPa

Feasibility tests for HP XAS at the Fe K-edge were done on γ-Fe_2O_3. The sample consisted of powdered γ-Fe_2O_3 with an average grain size of ∼ 30 nm. It was loaded in a Chervin-type diamond anvil cell equipped with standard diamonds with 400 μm culets and 1.5 mm thickness with Silicone oil as PTM. The gasket thickness and the gasket hole diameter were 30 and 125 μm, respectively. Figure 7.6 shows the absorption spectra of γ-Fe_2O_3 recorded during feasibility tests.

It has to be stressed that the homogeneity of the sample is of capital importance. Figure 7.7 shows the horizontal and vertical scans through the beam of the gasket hole filled with the powder. The 4 plotted curves correspond to 4 pseudocounters, defined as the integral of the intensity measured by the CCD camera at each point of the scan in the pixel range [0 - 310], [311 - 620], [621 - 930], [931 - 1240] respectively. Therefore, each curve represents a different energy portion of the polychromatic fan: *low*, *medium-low*, *medium-high*, and *high* energies. We notice that the thickness is homogeneous throughout the gasket hole, as there is very little variation of the beam transmission in the sample region.

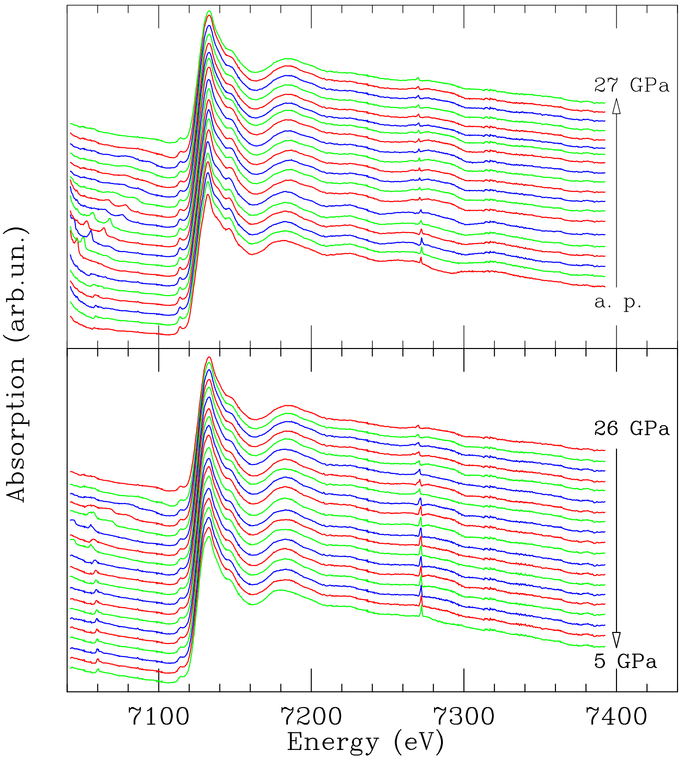

Figure 7.6: XAS spectra of γ-Fe_2O_3 from ambient pressure up to 27 GPa (*upper panel*) and from 26 GPa down to 5 GPa (*lower panel*).

After these successful feasibility tests, we performed the first HP XAS on hematite up to 100 GPa (Figure 7.8) in collaboration with a users group from the Laboratoire de Mineralogie-Cristallographie of the University of Paris 6 and 7. The HP behaviour of transition metal oxides and information on the valence of the metal ion as a function of pressure is of paramount importance to geophysicists. Fe_2O_3 hematite is considered as the model ferric iron (Fe^{3+}) mineral, hence its study important for both condensed matter physics and geophysics. Most investigations of the HP properties of ferric iron were made on the basis of the pressure behaviour of hematite. Yet, the exact nature of the HP phase of hematite remains undetermined. At 50 GPa, hematite undergoes a phase transition from the low-pressure corundum phase to a structure whose identification has generated very controversial reports [136, 137]. Among the proposed structures, one finds a distorted corundum structure which contains a single crystallographic site for Fe (Fe^{3+}) and a perovskite structure with two sites for Fe (Fe^{2+} and Fe^{3+}). XANES spectroscopy can give direct information of the valence of Fe, through the position of the absorption edge and by comparison of the shape of the edge and pre-edge features with state-of-the-art calculations [138]. Modifications of the pre-edge features and of the shape of the absorption edge are clearly detectable as a function of pressure from Figure 7.8. Together with the available information from XRD, Mössbauer and fluorescence spectroscopy, we hope to determine not only the electronic nature of the ions in the HP phase of hematite, but also the exact nature of the transition from the low-pressure insulating oxide to the HP metallic compound.

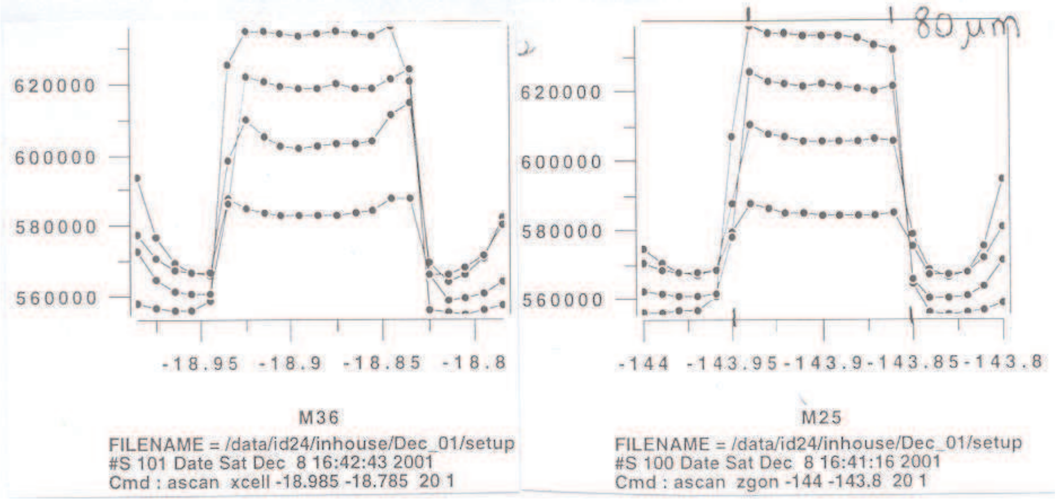

```
FILENAME = /data/id24/inhouse/Dec_01/setup
#S 101 Date Sat Dec  8 16:42:43 2001
Cmd : ascan  xcell -18.985 -18.785  20 1
```

```
FILENAME = /data/id24/inhouse/Dec_01/setup
#S 100 Date Sat Dec  8 16:41:16 2001
Cmd : ascan  zgon -144 -143.8  20 1
```

Figure 7.7: Horizontal and vertical scans through the beam of the gasket hole filled with Fe_2O_3. The scans refer to the experiment on hematite at 70 GPa.

7.2.2 Combined XRD and XAS measurements

XAS and XRD are two complementary techniques for the investigation of structural properties of matter. While XAS gives information about the local structure around the photoabsorber, XRD is essentially sensitive to the long-range order. The possibility of collecting in the same experimental setup both data sets is desirable since it is difficult to reproduce pressure and temperature conditions twice on different beamlines. Several efforts have been made to develop setups allowing the combined recording of XRD and XAS for different applications [115, 139–143]. For HP studies, it has been recently demonstrated that the combination of the two techniques is essential to fully describe the new phases [15, 114]. While XRD is able to identify the occurrence of new phases, its sensitivity to chemical ordering is reduced at very HP because of the inevitable increase in peak widths. XAS can play an important complementary role

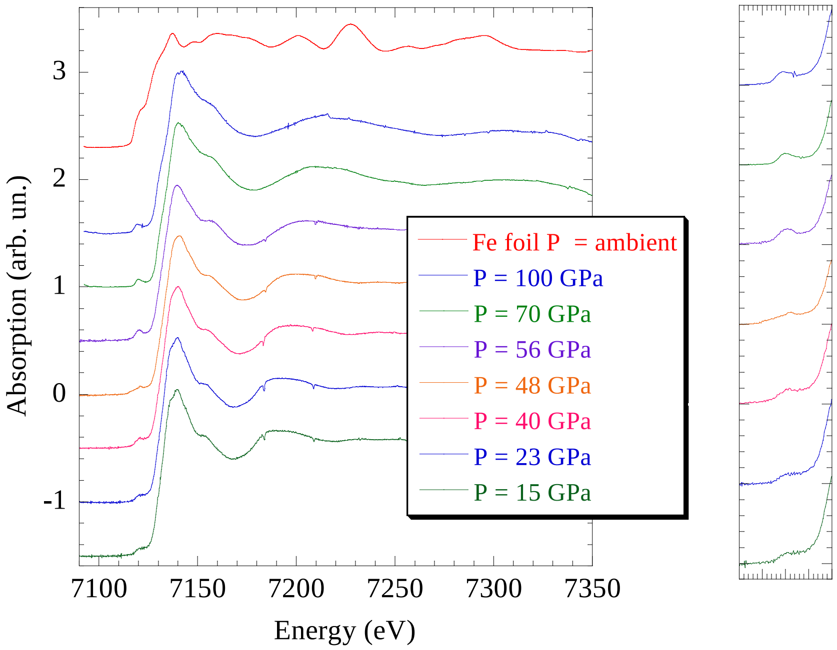

Figure 7.8: First HP XAS on hematite Fe_2O_3 up to 100 GPa (*left panel*). Modifications of the pre-edge features and of the shape of the absorption edge are clearly detectable as a function of pressure (*right panel*).

in identifying the local structure and the degree of short range chemical ordering in new phases, since it probes selectively the local environment of the absorber and it is less sensitive to non-hydrostaticity and uniaxial strain, measuring average bond distances directly. Usually XAS and XRD measurements are carried out at different SR beamlines, with different cell loading conditions, meaning that the sample in the two experiments is not subject to the same temperature, pressure and strain conditions. This frequently results in different values of, for instance, phase transition pressure, making interpretation more difficult. The combination of XRD and XAS measurements increases the reliability in data because the pressure (and temperature) evolution of the XAS data can simultaneously be followed with the angular displacement of diffraction peaks in the regions of phase stability in addition to the detection of new peaks at phase transitions. Furthermore, with use of an inert matrix (NaCl, LiF, for example) pressure and temperature conditions within the cell could be measured using internal diffraction measurements.

A new experimental setup for combined angle dispersive XRD and energy dispersive XAS measurements at HP has been successfully tested on beamline ID24 [144]. A schematic drawing of the setup is shown in Figure 7.9.

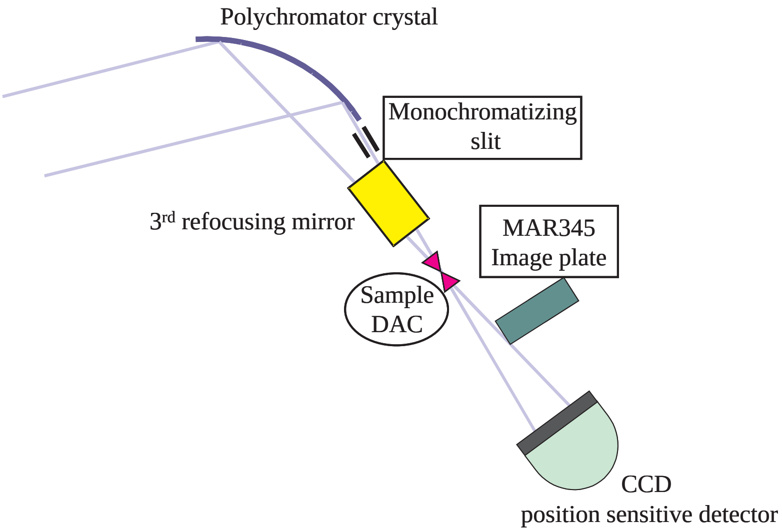

Figure 7.9: Schematic drawing of the combined angle-dispersive XRD and energy-dispersive XAS setup on beamline ID24. The slit selects a monochromatic beam out of the polychromatic fan during the XRD measurements. The MAR345 image plate, mounted in an offset position, intercepts the diffraction rings from the sample.

Besides the XAS data acquisition routinely performed, we recorded XRD data, using a narrow slit ($\sim$ 30 μm) to select a monochromatic beam (ΔE/E $\sim 2\ 10^{-4}$) from the polychromatic fan of radiation downstream the polychromatic crystal. The energy of the monochromatic beam was chosen in the pre-edge region in order to avoid resonance effects that can affect the XRD pattern, and to reduce absorption. The diffraction rings from the sample were intercepted by a MAR345 image plate detector with 150 μm pixel resolution mounted in an offset position. The DAC was rotated with respect to the X-ray direction to increase the angular range in order to have access to the smallest possible value of d (distance between successive lattice planes). The sample-detector distance was calibrated by an Al_3O_3-filled gasket at the same sample position. This new setup has been tested on two different systems: gallium phosphide (GaP) and zinc dichloride ($ZnCl_2$).

Combined XRD and XAS measurements on GaP at HP up to 35 GPa

The sample consisted of fine powdered GaP (Alfa Aesar, 99.999%) loaded with a mixture of methanol:ethanol = 4:1 as PTM in a Chervin-type DAC [57,58]. Two different loadings using different pairs of diamonds were used depending on the maximum pressure reached. For pressures up to 14 GPa we equipped the DAC with standard diamonds with 600 μm flats and thickness of 1.5 mm. The diameter of the gasket hole was 250 μm and the sample thickness $\sim$ 35 μm. For pressures up to 35 GPa we used standard diamonds with 320 μm flats and thickness of 1.5 mm. The diameter of the gasket hole was 125 μm and the sample thickness $\sim$ 30 μm. The pressure was measured using the ruby fluorescence method [62]. The XAS data were collected at the Ga K-edge (E = 10.367 keV). A bent Si (111) crystal horizontally focused a polychromatic fan of energy width ΔE = 480 eV onto the sample. The presence of diffraction peaks from the diamond anvils limited the energy range to $\sim$ 380 eV. The focal spot size was 17 μm (H) $\times$ 14 μm (V) (FWHM). For the XRD experiment we monochromatized the beam with a $\sim$ 30 μm slit choosing a wavelength of $\lambda = 1.1989$ Å. The energy resolution was ΔE/E $\sim 2 \times 10^{-4}$. The maximum 2θ values were 46 deg. and 42 deg. for the first and second loading respectively, determined by the size of the gasket hole and the thickness of the preindentation.

We chose GaP to test our new setup because, in spite of the number of studies carried out, there are still some controversies and unknowns in this system. As far as the phase transition from GaP-I to GaP-II is concerned, the most recent XRD measurements [145] have shown a phase transition from a zincblende structure to a site-disordered *Cmcm* structure. This is in contradiction with previous studies [146–148] where a transition to a β-Sn structure had been reported, even though the diffraction data contained extra reflections not accounted for. According to the previous XAS study at HP [90], GaP undergoes a phase transition from a four-fold to a six-fold environment, result which is consistent both with a β-Sn-like and with a *Cmcm*-like structure. In fact, the β-Sn structure would have six equidistant nearest neighbours if $c/a = \sqrt{(4/15)} = 0.5164$, otherwise the structure has four nearest neighbours and two neighbours slightly further away, as in the case of Sn at 298 K [149]. The *Cmcm* structure is an orthorhombic distortion of the NaCl structure and the way in which the coordination of the *Cmcm* structure differs from that of NaCl (which is six-fold coordinated) depends critically on the values of the lattice parameters and of the internal atomic coordinates. Therefore, it is difficult using EXAFS analysis to discriminate between the two structures, especially if the distortion is small. However, from the XANES analysis and the high sensitivity of multiple scattering paths to local bonding geometry and coordination, this uncertainty can be clarified. The data we recorded deserve a deeper analysis, and are shown in this Thesis as an example of application of our setup for combined XAS and XRD measurements. Figure 7.10 shows the raw absorption data at the Ga K-edge and the relative diffraction patterns up to 14 GPa. In this pressure range we do not observe any phase transition, as expected. The decrease of the frequency of the EXAFS oscillations in the XAS data indicates a shortening of the bond distances in agreement with the shift towards higher angles of the diffraction peaks of the zincblende structure.

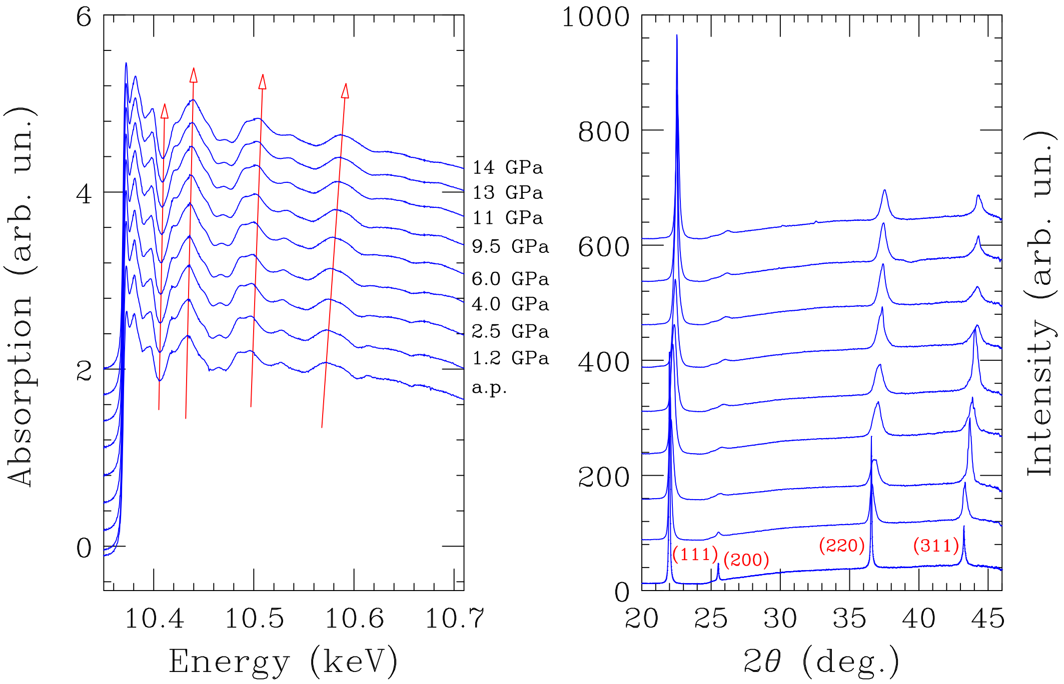

Figure 7.10: XAS spectra and relative XRD patterns of GaP up to 14 GPa.

Figure 7.11 shows the data recorded between 20 and 35 GPa. At 27 GPa the data show the onset of the transition to the phase GaP-II. The diffraction pattern shows clearly the existence of a mixed phase: the (200) reflection of the zincblende phase has disappeared and the (111) and the (220) reflections coexist with a new peak at $\sim$ 29 deg.. The modifications in the frequency and shape of the XAS signal reflect the difference in the local environment around the photoabsorber respect to the data at lower pressures. The data at 35 GPa reveal that the phase transition is complete and the sample is in the phase GaP-II. The XAS spectrum shows completely different features in both the

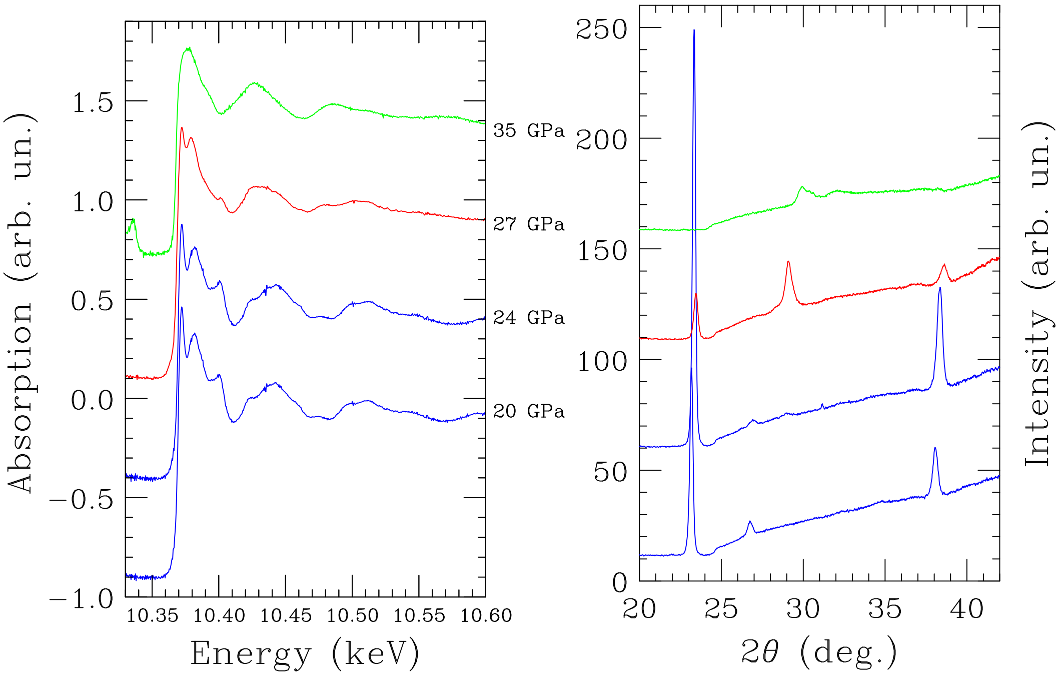

Figure 7.11: XAS spectra and relative XRD patterns of GaP from 20 to 35 GPa.

EXAFS and in the XANES regions and the reflections of the zincblende phase have disappeared in the XRD pattern.

Combined XRD and XAS measurements on $ZnCl_2$ at HP and HT up to 35 GPa and 623 K

These measurements have been performed as a continuation to those of C. Fillaux et al. (Project number: HS1634) where the first HP-HT XAFS spectra of $ZnCl_2$ in different phases including the glassy one had been obtained. The model sample consisted of dehydrated fine powdered $ZnCl_2$ (Alfa, ultra dry, 99.999%). It was loaded in a glove box to avoid moisture contamination. We used a heated Chervin-type DAC, equipped with standard diamonds with 300 μm culets and thickness of 1.5 mm without PTM. The diameter of the gasket hole was 120 μm and the sample thickness $\sim$ 30 μm. The pressure was measured with the ruby fluorescence method [62] and the temperature using a K-type thermocouple placed on the back of one diamond. The XAS data were collected at the Zn K-edge (E = 9.659 keV). A polychromatic fan of energy width ΔE = 470 eV was focused at the sample position. The focal spot size was 20 μm (H) × 17 μm (V) (FWHM). For the XRD experiment we selected a monochromatic beam of wavelength of $\lambda = 1.2858$ Å. The energy resolution was $\Delta E/E \sim 2 \times 10^{-4}$. The maximum 2θ value was 35 deg..

The structures of $ZnCl_2$ in the α, β and γ phases are all formed by a network of $ZnCl_4$ tetrahedra sharing their corners [150]. The structure of δ-$ZnCl_2$, the HP phase of $ZnCl_2$ still presents some unknowns. According to Sakai [151], the δ-$ZnCl_2$ has a $CdCl_2$-type structure. However, not all the calculated values of the interplanar spacings d, and the relative diffraction intensities I based on the hexagonal unit cell of the $CdCl_2$ structure have been observed in the diffraction pattern. Furthermore, the strong diffraction peak due to the lattice plane with $d = 2.51$ Å, which is assigned as the (104) reflection of the $CdCl_2$ structure, is not indexed by the JCPDS-International Centre of Diffraction Data because of the poor agreement between the reflections and the given cell. In such a case a combined XRD and XAS experiment could clarify this uncertainty. A possible strategy is to compare the XAS data with XANES simulations performed on a cluster built by using cell parameters and atomic positions obtained from the Rietveld refinements of the XRD data.

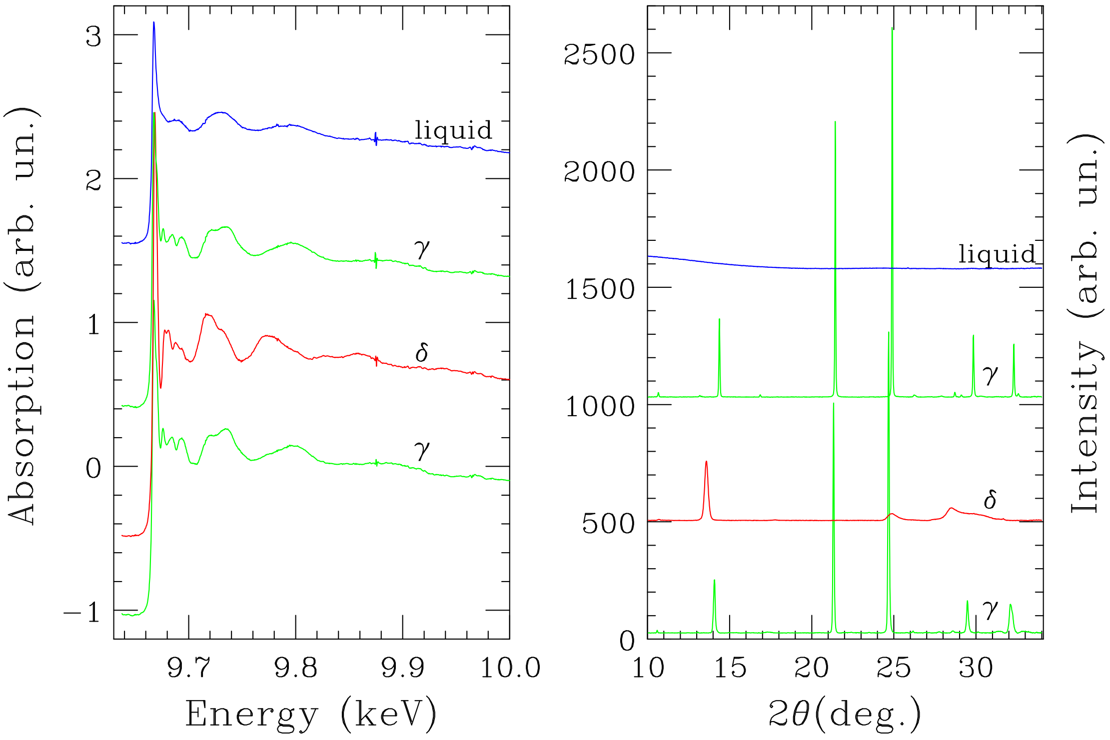

Figure 7.12: XAS spectra of $ZnCl_2$ at different pressure and temperature conditions and relative XRD patterns at the same conditions.

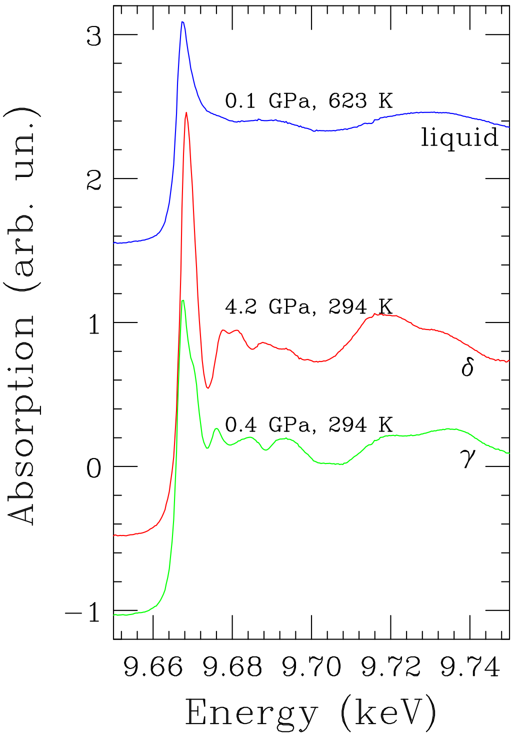

Figure 7.13: XANES spectra of the three observed phases of $ZnCl_2$. Large variations in the *4p* density of states above the Fermi level can be observed between γ-$ZnCl_2$ and δ-$ZnCl_2$.

Figure 7.12 shows combined raw XAS and XRD data of three different phases of $ZnCl_2$. At loading, T = 294 K and P = 0.4 GPa, $ZnCl_2$ is in the tetragonal γ-phase characterized by four-fold coordinated Zn (JCPDS 16-0850). On pressure increase and at constant temperature, at P = 3.2 GPa, the sample undergoes a phase transition to the δ-phase. Following Sakai's determination [151] the δ-$ZnCl_2$ in the $CdCl_2$-type structure (JCPDS 39-0887) is characterized by six-fold coordinated Zn. The differences in local coordination of Zn between the two phases are reflected by the large modifications of the frequency and amplitude of the XAS signals. At T = 363 K and P = 1.0 GPa back-transformation to the γ-phase is observed. At 0.1 GPa and T = 623 K the diffraction data do not show any evidence of Bragg reflections and the XAS spectrum shows that all high frequency contributions are damped out by a large degree of local disorder, indicating that the sample is in the liquid phase. In Figure 7.13 we plot the XANES relative to the three observed phases. The large variation in the intensity of the white line between the γ and the δ phase indicates that the change in local coordination in

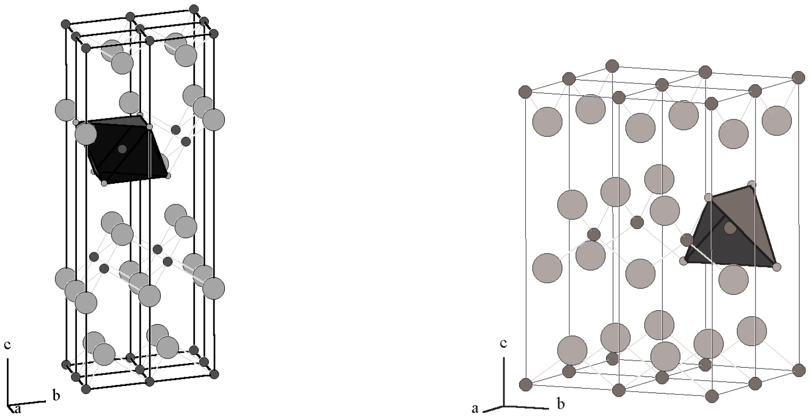

Figure 7.14: Drawings of δ- and γ-ZnCl$_2$ highlighting the tetrahedral and octahedral coordination polyhedra.

this system induces large variations in the *4p* density of states above the Fermi level.

All the diffraction data recorded are of good quality and can be analyzed using the Rietveld method [152]. The best refinement for the P = 0.4 GPa and T = 294 K pattern results in an tetragonal cell in space group *P42/nmc* with a = 3.6682(10) Å and c = 10.418(10) Å and atomic positions at [Zn (2a): 0, 0, 0] and [Cl (4d): 0, 1/2, 1/8]. Using Sakai's model, the best refinement for the P = 4.2 GPa and T = 294 K pattern results in an hexagonal cell in space group *R-3m* with a = 3.498 Å and c = 16.2 Å and atomic positions at [Zn (3a): 0, 0, 0] and [Cl (6c): 0, 0, 0.748]. Figure 7.14 shows the drawings of the two phases. However, for the latter phase there is large disagreement between calculated and observed XRD patterns.

The cell parameters and atomic positions have been used to build a cluster and to simulate the XAS spectra. We have performed a comparison of the data with full multiple scattering calculations using a self-consistent energy dependent exchange correlation Hedin-Lundqvist potential (FEFF8 package [153]). Self consistency was obtained by successively calculating the electron density of states, electron density and Fermi level at each stage of the calculation within a 4 shell cluster centered on the atom for which the density of states is calculated, and then iterating. Full multiple scattering XANES calculations were carried out for a 7 shell cluster centered on the absorbing atom: all multiple-scattering paths within this cluster were summed to infinite order. Figure 7.15 shows the simulated spectra of γ-ZnCl$_2$ and δ-ZnCl$_2$. No thermal damping effects are included in the calculation. While the simulated XANES of the γ-ZnCl$_2$ is in qualitative agreement with the experimental spectrum, besides perhaps a different behaviour of the atomic background, the proposed structure for δ-ZnCl$_2$ does not reproduce the features in the experimental data, in particular the double oscillations at 9.675 and 9.689 keV are not correctly simulated by the calculations. Increasing the size of the full multiple scattering cluster does not lead to an improvement in this energy region. From this result we can confirm the uncertainty regarding ZnCl$_2$ at HP whose structure deserves a further investigation. Measurements shall be performed in a dedicated XRD beamline. Moreover, it will soon be possible to perform structural fitting of the XANES region [154,155] leading to a higher exploitation of the XAS data with respect to the qualitative comparison with simulations available today.

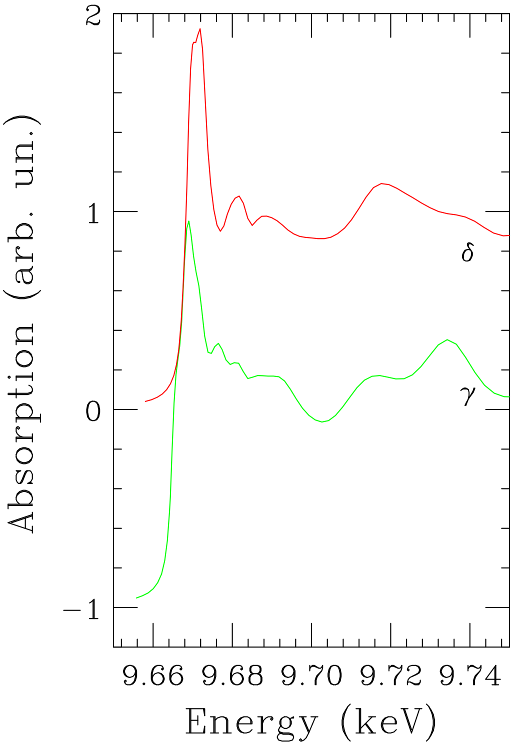

Figure 7.15: Simulated spectra of γ-ZnCl$_2$ and δ-ZnCl$_2$.

In conclusion, a new experimental setup for combined ADXRD and EDXAS measurements at HP has been successfully tested on two different samples on beamline ID24. Due to the inherent limitations of this setup (in particular the energy of the incident beam cannot be chosen arbitrarily, but is restricted by the value of the absorption edge), the XRD measurements cannot substitute a complete data set measured in a dedicated XRD beamline. However, most of the diffraction patterns collected are of good quality and can provide, through Rietveld refinement, many of the structural parameters required for modelling XAS data.

7.2.3 High temperature DAC

In order to be able to perform combined HP/HT studies to investigate the properties of matter in unexplored regions of P-T space, a new heated DAC has recently become part of the HP equipment of ID24. This cell has been developed from the Chervin model [57] at the *"Laboratoire Pierre et Marie Curie"* of the University of Paris 6. The body, the piston and the lid of the cell are made of *"super-alliage PER 72"* supplied by "Aubert et Duval" (Gennevilliers, France). This alloy, based on Ni, contains 18% of Cr and 15% of Co and is particularly suited for heated DACs thanks to its relatively low expansion coefficient: 14.8×10^{-6} mm/K at 1073 K. After being manufactured, each piece is thermally treated in order to achieve an adequate hardness (1500 MPa at room temperature and 1050 MPa at 1073 K). The diamonds are glued with a refractory amalgam. The HT conditions are achieved by external resistive heating. A picture of the external heater is shown in Figure 5.4. The temperature is set by a temperature controller (WATLOW 96) connected to the heaters by means of leads and a thermocouple. A first commissioning test has been done on this cell to check its correct behaviour at HP and HT conditions. In particular one of the common issues of these devices is the difficulty to decrease pressure at HT, because the large thermal expansion of the metal supporting the DAC prevents the normal behaviour of the piston during the decompression.

For the test we equipped the cell with standard diamonds of 300 μm flats and thickness of 1.7 mm. The hole diameter in the stainless steel gasket was 100 μm. The cell volume was loaded with a mixture of methanol:ethanol = 4:1, with a ruby chip to monitor the pressure values. The temperature was measured using a K-thermocouple placed at the back of the diamonds. We observed a $\Delta T \simeq$ - 10% between the temperature on the diamonds and the temperature of the heater. The maximum pressure reached was 20 GPa. The test was performed in air, so the maximum temperature reached was kept below 500 K (T_{max} = 494 K) to avoid graphitization of the diamonds. Figure 7.16 shows the evolution of pressure in the cell volume as a function of the membrane pressure and the pressure in the cell volume for different values of temperature on the diamond. First, at constant temperature of 293 K we increased the pressure on the membrane to 34.5 bar to have a pressure in the cell of $\sim$ 2 GPa. Increasing the temperature up

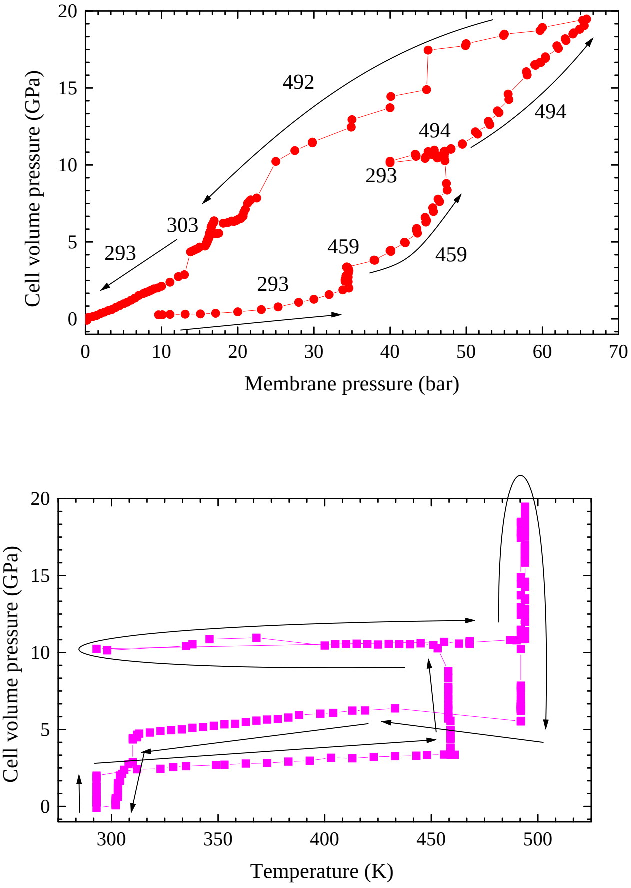

Figure 7.16: Pressure in the cell volume as a function of membrane pressure (*upper panel*) and the pressure in the cell volume for different values of temperature on the diamond (*lower panel*).

to 459 K and keeping constant the pressure on the membrane within the error of ± 0.3 bar we noticed an increase in pressure in the cell volume of ∼ 1 GPa. At constant temperature of 459 K we increased the pressure up to 9 GPa in the cell volume. At this point we quenched down to 294 K and then back to 494 K. During this temperature cycling, keeping constant the pressure on the membrane the pressure in the volume cell remained rather stable, with a slight increase up to 11 GPa. From this point, we increased the pressure up to 20 GPa and then down to ∼ 5 GPa, at constant T ∼ 494 K. During this pressure cycle at high-temperature, the pressure in the cell volume varied normally and the cell did not show any evidence of jamming due to the expansion of the metal. From this preliminary test we can conclude that the use of *"super-alliage PER 72"* overcomes the typical problems that affect external heated DACs. Other tests are foreseen for the future: namely the aim is to reach temperatures of 1000 K by enclosing the cell in a vacuum chamber and to add a second heater in the cavity around the anvils.

Chapter 8

Study of InAs under pressure

This chapter concerns the study of structural properties of binary compounds $A^N B^{(8-N)}$ at high-pressure. The traditional understanding of structure and bonding of $A^N B^{(8-N)}$ octet semiconductors and of their behaviour under compression is based on the notion that at the increase of the pressure, the four-fold coordinated structures with low densities are transformed to denser phases of increased coordination: four-fold (diamond, zincblende, wurtzite) → six-fold (β-Sn, NaCl) → eight-fold (CsCl). This structural sequence was partially confirmed by a large number of experimental works, that prompted many computational studies. A recent theoretical approach predicted the non-existence of the CsCl phase for the more ionic members of the octet family, and predicted possible alternatives structures: the InBi-type and the AuCd-type. In this scenario we examined this prediction for the InAs compound, because it has the lowest predicted transition pressure to the CsCl phase, performing a combined X-ray diffraction and absorption study. From diffraction data we determined the structural sequence as a function of pressure, from absorption data we determine the degree of chemical ordering of the new phases. By revealing the presence of a Pmma phase in InAs at high-pressure we proved that the combination of the two techniques is essential to fully describe the new phases. We demonstrate the power of recent theoretical calculations, not only able to identify dynamically unstable phases, but also to predict alternative structures.

8.1 $\mathbf{A}^N\mathbf{B}^{(8-N)}$ compounds

8.1.1 Introduction

The structure of the binary compounds $A^N B^{(8-N)}$ can be explained using bond language [9]. This chemical approach describes in a simplified way the three-dimensional energy bands of these compounds and how these vary from one material to another. The bonds that characterize these compounds are covalent bonds arising from overlapping tetrahedrally oriented hybridized sp^3 orbitals.

When the atoms form covalent bonds in a crystal, it is no longer appropriate to discuss their electronic configuration in terms of atomic orbitals $\phi_{nl}(\alpha)$ around each atom α, and we have to introduce a new set of states directed from one atom towards its nearest neighbours: the *hybridized orbitals*. A hybridized orbital, χ_n, is a linear combination of atomic orbitals ϕ_{nl}. For example, the hybridized orbital χ_{sp} is:

$$\chi_{sp}(r) = f_s(r) + (z/r) f_p(r). \tag{8.1}$$

A hybridized orbital is a *superposition* of two atomic amplitudes, and the associated probability density will exhibit interference effects. Thus (8.1) exhibits a maximum amplitude near the atomic radius $r = r_a$ when $\cos\theta = z/r = 1$, i.e. in the direction of $+z$ axis. The χ_{sp^3} hybridized orbital is given by:

$$\chi_{sp^3}(r) = f_s(r) + [(x/r) \pm (y/r) \pm (z/r)] f_p(r), \tag{8.2}$$

which points in the $(\pm 1, \pm 1, \pm 1)$ direction. The properties of the directed orbitals can be expressed in terms of bonding and antibonding orbitals:

i. a bonding orbital ψ_b consists of two directed orbitals $\chi_n(\alpha)$ and $\chi_n(\alpha')$ associated with nearest neighbour atoms α and α' combined in phase in such a way that ψ_b is large in the bonding region between the atoms, as shown in Figure 8.1;

ii. an antibonding orbital ψ_a is similar to a bonding orbital except that the phase has been reversed between atoms. Thus ψ_a has a node in the bonding region.

The nature of the hybridized orbitals associated with bonding and antibonding states is shown in Figure 8.2. The bonding states have lower energy, are centered predominantly on the more electronegative atom, and point towards the nearest neighbour atoms. The antibonding states have a higher energy and are centered predominantly on the less electronegative atom, and point away from the nearest neighbours. Therefore, the

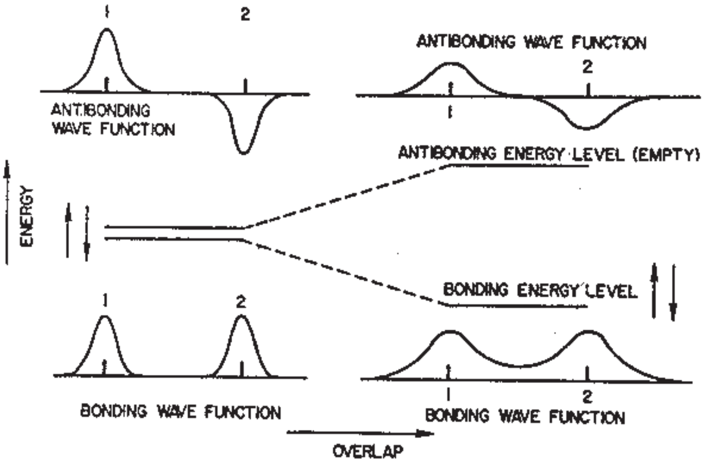

Figure 8.1: Formation of bonding and antibonding states on going from atom to crystal. In bonding states the wave function amplitude ψ_b associated with a directed orbital centered on atom 1 interferes constructively or in phase with a similar orbital centered on atom 2 in the bonding region between atoms 1 and 2. Similarly, the amplitude ψ_a of the antibonding orbital exhibits a node in the bonding region.

formation of covalent bonds leads to the appearance of an energy gap between bonding and antibonding states. Most III-V compounds have ambient pressure structures in which each atom is tetrahedrally coordinated, corresponding to χ_{sp^3} orbitals (8.2) with the product of the three ± signs positive on one atom and negative on the other.

8.1.2 Ionicity of the bond

All $\mathrm{A}^N\mathrm{B}^{(8-N)}$ compounds can be treated within the framework of a model which is described by particular values of certain parameters. In this way, with the correct choice of the parameters, the picture of semiconductor structures can be greatly simplified. One of the most important of these parameters is the ionicity of the bond. Using Phillips' definition [9], the ionicity of the bond is defined as the fraction f_i of ionic character in the bond compared to the fraction f_c of covalent character. By definition these fractions satisfies the relation:

$$f_c + f_i = 1. \tag{8.3}$$

In a crystal of formula $\mathrm{A}^N\mathrm{B}^{(8-N)}$, considering a unit cell centered on an origin halfway between the two atoms, and denoting by V_A and V_B the screened Coulomb potential seen by valence electrons outside the ion cores of atom A and B respectively, the potential

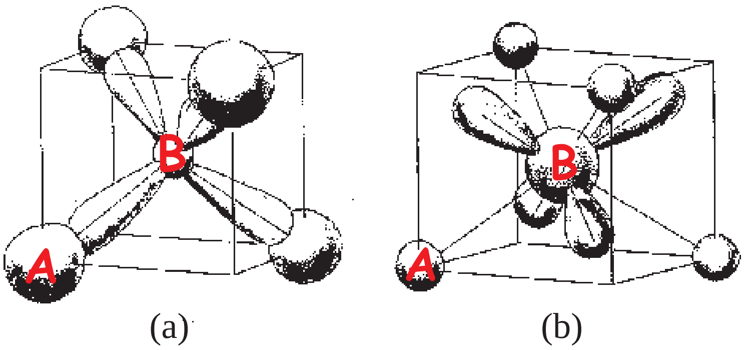

Figure 8.2: Directed (a) bonding and (b) antibonding orbitals. The A atoms are more electropositive, the B atoms are more electronegative.

of the crystal can be written as:

$$V_{crystal} = \sum_{\alpha} V_A(\mathbf{r} - \mathbf{r}_\alpha) + \sum_{\beta} V_B(\mathbf{r} - \mathbf{r}_\beta), \tag{8.4}$$

where $\mathbf{r}_\alpha$ and $\mathbf{r}_\beta$ refer to the lattice sites of the sublattices of A and B atoms respectively. Looking at only one cell, and only at potentials V_A and V_B associated with the atoms in that cell, we separate $V_{crystal}$ into the parts which are even and odd with respect to the interchange of A and B by means of inversion about the origin. These we call $V_{covalent}$ and V_{ionic} respectively:

$$V_{covalent} = V_A + V_B, \tag{8.5}$$

$$V_{ionic} = V_A - V_B. \tag{8.6}$$

f_c and f_i are related to average values of (8.5) and (8.6) calculated with respect to certain wave functions of the crystal. The average energy of an sp^3-hybridized state centered on atom A and B in terms of free-atom energies E_s and E_p are respectively:

$$E_A = \frac{E_s(A) + 3E_p(A)}{4}, \tag{8.7}$$

and

$$E_B = \frac{E_s(B) + 3E_p(B)}{4}. \tag{8.8}$$

For two atoms A and B, the difference between E_A and E_B will lead to a charge transfer when the two atoms are bonded together. When both atoms in the unit cell are the same, we have a completely covalent bond and the hybridized orbitals have the same energy E_A. The potential V_{ionic} is zero in this case, and the degeneracy of the overlapping sp^3

orbitals is removed by interaction with $V_{covalent}$. The levels are separated in energy by the average homopolar energy gap which we denote by E_h. When the two atoms in the unit cell are not the same, the average energies of an sp^3-hybridized state are different for the two atoms A and B so that even without taking into account $V_{covalent}$, there is an energy gap produced by V_{ionic}. Thus, the total energy associated with the A–B bond in the crystal can be expressed as [9]:

$$E_g = E_h + iC, \tag{8.9}$$

where E_h represents the average energy gap produced by $V_{covalent}$ and C represents the magnitude of the energy gap produced by V_{ionic}. Since the fractional ionic character of a covalent bond f_i depends on the magnitude of the antisymmetric potential V_{ionic} compared to the symmetric potential $V_{covalent}$, we can define the *ionicity phase angle* ϕ of $E_g = E_h + iC$ in the (E_h, C) plane (Figure 8.3) so that:

$$\tan\phi = C/E_h, \tag{8.10}$$

and from this we obtain:

$$f_i = \sin^2\phi = \frac{C^2}{E_g^2}, \tag{8.11}$$

$$f_c = \cos^2\phi = \frac{E_h^2}{E_g^2}. \tag{8.12}$$

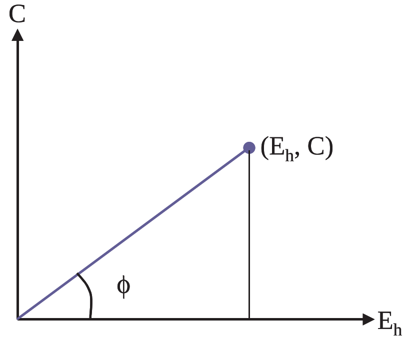

Figure 8.3: The phase angle ϕ in the (E_h, C) plane measures the ionic and covalent character of the $\mathrm{A}^N\mathrm{B}^{(8-N)}$ bonds.

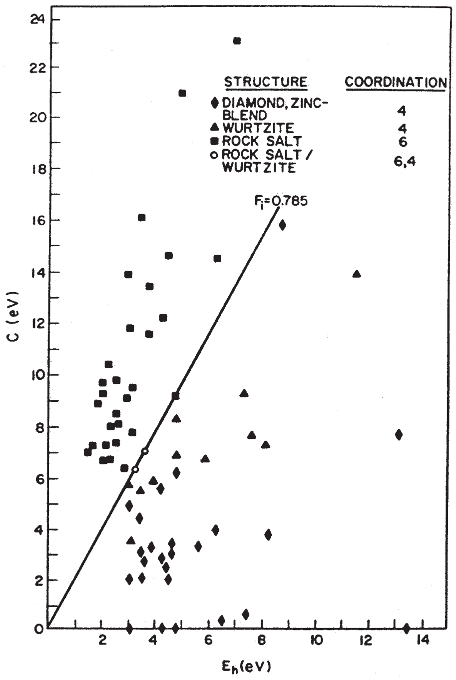

Figure 8.4: Values of E_h and C for crystals of the type $A^N B^{(8-N)}$. The coordination numbers are indicated. Note that $F_i = 0.785$ separates all four-fold from all six-fold coordinated crystals.

8.1.3 Crystallization of $A^N B^{(8-N)}$ compounds

The ionicity of the bond can be considered as a determinant factor in the phase transitions from four-fold to six-fold coordinated structures. In fact, while all the more covalent members of the $A^N B^{(8-N)}$ octet family crystallize at ambient pressure in four-fold tetrahedral structures, the more ionic members nearly all crystallize in the six-fold coordinated *rocksalt* (NaCl) structure. One can describe the cohesive energies, lattice constants, and bulk modulus of these six-fold coordinated crystals by a classical model based on closed-shell electronic configurations. Indeed, the cohesive energy here arises mainly from the Coulomb attraction between cation and anion, the charge transfer is nearly complete and there is little electron sharing. Bonds characterized by a larger ionicity will lead to structures with larger coordination numbers, driven by the greater Coulomb attractive energy. Thus when the bond is sufficiently ionic, i.e. when $f_i > F_i$ (where F_i is a *critical ionicity*) the crystal will have a structure in which each atom is more than four-fold coordinated. Values of E_h and C and the coordination numbers for crystals of the type $A^N B^{(8-N)}$ are indicated in Figure 8.4.

8.2 Structures at ambient pressure

This section briefly describes the principal structures found so far in the III-V semicondunctors at ambient pressure. The structures will be referred by space-group symmetry (*Fd3m, Fm3m,* etc.) or by name when the latter is more common (diamond, zincblende, etc.). The description of the structures and the atomic sites are taken from the *International Tables for Crystallography*, Vol. A (1983). The atomic positions are given as fractional coordinates. Lattice parameters are designated by a, b, and c, with angles α, β, and γ. The "reflection conditions", are those conditions on h, k, and ℓ that have to be satisfied for the $(hk\ell)$ reflection to be allowed.

8.2.1 Four-fold coordinated structures

Diamond and Zincblende

The diamond structure is found in Si and Ge at ambient conditions. The structure and the diffraction pattern are shown in Figure 8.5. It is cubic, space-group *Fd3m*, centrosymmetric with atoms on the 8(a) site at (1/8, 1/8, 1/8). The structure is tetrahedrally coordinated with four nearest neighbours at a distance of $\sqrt{3}a/4$. The general reflection conditions are h, k, and ℓ all even or all odd in $hk\ell$; and $k+\ell = 4n$, and k and $\ell = 4n$, in $0k\ell$, and likewise for cyclic permutations of $hk\ell$. The location of all atoms on the 8(a) special positions gives the further condition $h + k + \ell = 2n + 1$ or $4n$ in $hk\ell$.

Zincblende (ZB) is the dominant ambient pressure phase in the III-V semiconductors and is the binary analog of the diamond structure. It is cubic, space-group $F\bar{4}3m$ with one atom species on the 4(a) site at (0, 0, 0) and the other on the 4(c) site at (1/4, 1/4, 1/4), as shown in Figure 8.6. Each atom is therefore tetrahedrally coordinated with four *unlike* nearest neighbours. The reflection conditions are h, k, and ℓ all even or all odd in $hk\ell$. The diffraction pattern is very similar to that of diamond, but contains extra reflections (for example (200), (222) and (420)), which are the so called "difference reflections".

Wurtzite

The wurtzite structure (Figure 8.7) is adopted by GaN, AlN ... at ambient conditions. It is hexagonal, space-group $P6_3mc$. The "ideal" wurtzite structure has $c/a = \sqrt{(8/3)} =$ 1.633 and has one atomic species on a 2(b) site at (1/3, 2/3, 0) and the second on a 2(b) site at (1/3, 2/3, u), where $u = 3/8$. The structure is not centrosymmetric. The

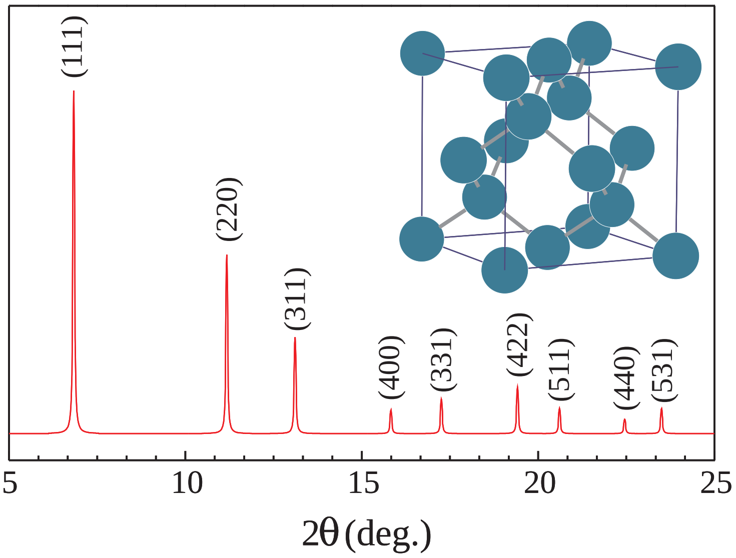

Figure 8.5: Drawing of the diamond structure and simulated diffraction pattern.

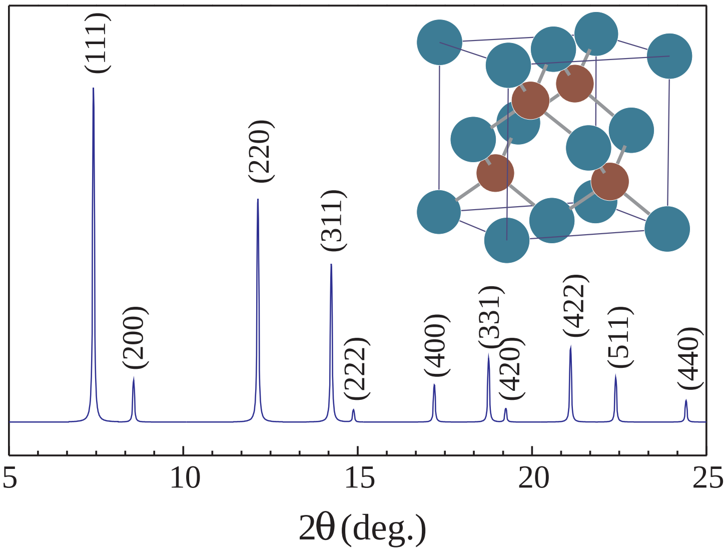

Figure 8.6: Drawing of the zincblende structure and simulated diffraction pattern.

only general reflection condition is $\ell = 2n$ in $hk\ell$. The location of all atoms on the 2(b) special positions gives the further condition that $\ell = 2n$ if $h - k = 3n$ in $hk\ell$.

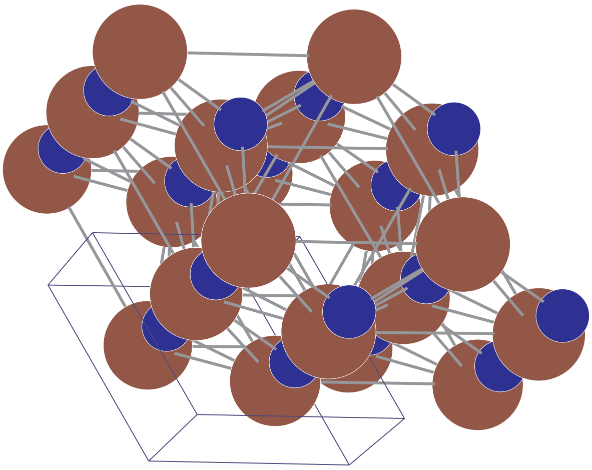

Figure 8.7: Drawing of the wurtzite structure.

8.2.2 Six-fold coordinated structures

NaCl or Rocksalt

The NaCl or rocksalt structure is found in the more ionic $A^N B^{(8-N)}$ compounds like CdO at ambient pressure. The structure and the diffraction pattern are shown in Figure 8.8. It is cubic and centrosymmetric, space-group *Fm3m* with atoms on the 4(a) and 4(b) sites at (0, 0, 0) and (1/2, /12, 1/2), respectively. The reflection conditions are h, k, and ℓ all even or all odd in $hk\ell$. Each atom has six *unlike* nearest neighbours at a distance $a/2$.

8.3 Behaviour under compression of $A^N B^{(8-N)}$ compounds

8.3.1 First studies

Structural studies of the group IV, III-V, and II-VI semiconductors start with the pioneering work of Jamieson in 1963 on Si and Ge and on the III-Vs AlSb, GaSb, InP, InAs, and InSb [156,157]. According to these studies the pressure has the effect of transforming the low-density tetrahedrally-coordinated structures in higher density ones with higher coordination numbers. In particular, Si and Ge undergo a phase transition from the diamond structure to the β-Sn structure, so do the more covalent AlSb, GaSb,

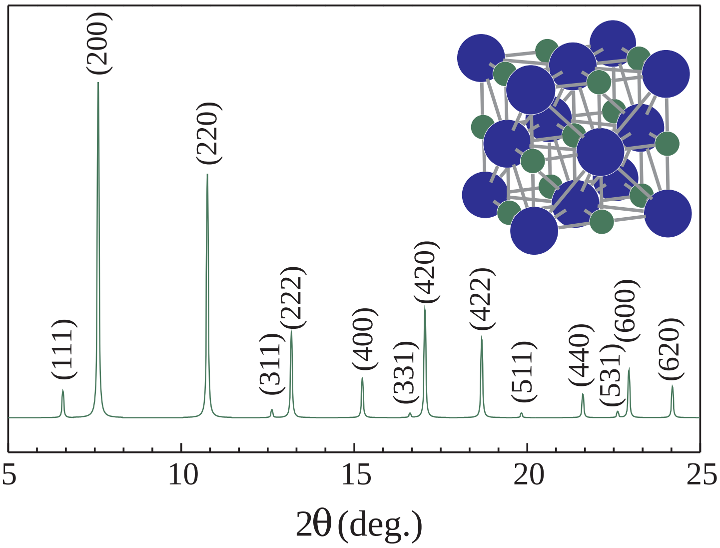

Figure 8.8: Drawing of the NaCl structure and simulated diffraction pattern.

whereas the more ionic III-V semiconductor InP and InAs, undergo a phase transition from a zincblende structure to an NaCl structure. These phase transitions are associated with a change in volume $\Delta V/V_t$ (where V_t is the molar volume of the tetrahedrally coordinated structure at the transition pressure P_t, and ΔV is the volume change at the transition) of about 20%. In contrast, phase changes for metals and insulators usually involve volume changes of only a few percent. Following these first studies, the behaviour under compression seemed to follow a structural sequence common to all $A^N B^{(8-N)}$ compounds. A preliminary conclusion was that the higher density structures to which tetrahedrally coordinated $A^N B^{(8-N)}$ compounds transform under pressure are structures that exist at zero pressures in more ionic $A^N B^{(8-N)}$ compounds. The possible higher-density structures are the β-Sn-type, NaCl-type, and CsCl-type structures. Once again the ionicity degree of the bond is a parameter that accounts for the behaviour of these compounds at HP. Phillips [9] classified the transitions in a plot, where the abscissa represents the ionicity of the bond f_i, and the ordinate the pressure P (Figure 8.9). It can be seen that:

i. if $f_i \lesssim 0.35$ the semiconductor transforms directly to a β-Sn type structure;

ii. if $0.35 \lesssim f_i \leq 0.785$ the semiconductor first transforms to a NaCl type structure, and transforms to an β-Sn type structure only at much higher pressures.

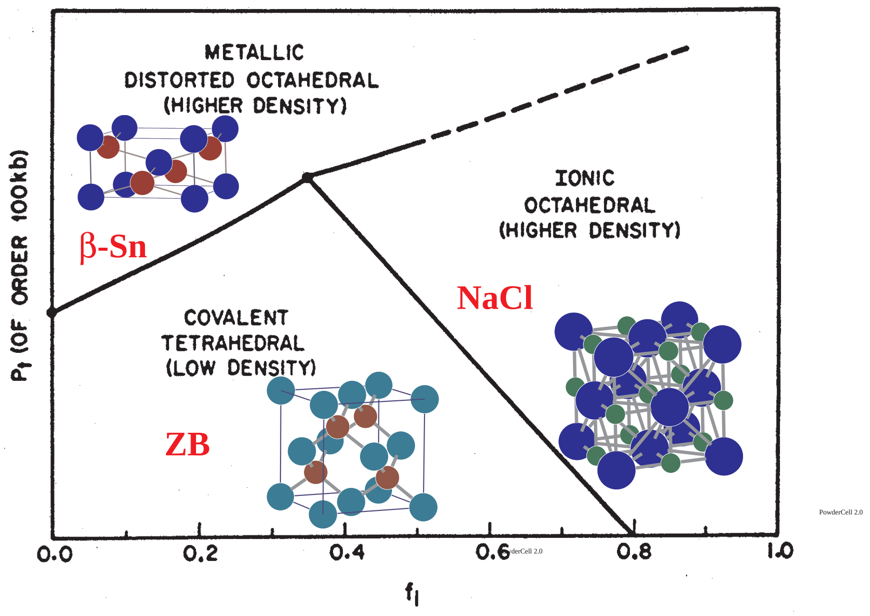

Figure 8.9: Schematic (f_i, P) phase diagram showing the covalent, ionic, and metallic structures of $A^N B^{(8-N)}$ compounds.

The structural sequence foreseen by Phillips [9] for these compounds under pressure is therefore: zincblende → NaCl → β-Sn → CsCl, where the CsCl like structure is the densest structure with a coordination of 8. For over 30 years this structural sequence has been partially confirmed by a large number of experimental works. The CsCl structure has been observed in InSb (site disordered), but not in the more ionic members. The mass of experimental data prompted many computational studies [158–163]. These theoretical studies were based on guessing a few candidate HP phases and then computing their total energies versus volume, from which the transition pressures P_t between phase α and β were obtained. This was achieved by setting the difference of the enthalpy of the two phases equal to zero. Having restricted the candidate phases, the total energy versus volume curves were calculated for the zincblende, NaCl, β-Sn, and CsCl phases of numerous compounds, and these calculations showed that a zincblende → NaCl → β-Sn → CsCl transition sequence is a general feature for most octet compounds.

8.3.2 Recent studies

However, in the 90s the advent of the HP ADXRD techniques brought a remarkable improvement in data quality [164], and these years saw a revolution in the picture of structural systematics of IV, III-V, and II-VI semiconductors. Many phases were found to have more complex, lower-symmetry structures than previously thought, many new phases were discovered and identified; conversely, some supposed transitions were shown to be mistaken interpretations of previous data [165–168]. The general trend of these new discoveries was the almost complete disappearance of the β-Sn structure that had played a prominent role in the previous systematics of these systems. In almost all cases the true structure was shown to be the orthorhombic phase *Cmcm*. These new structures were included in total energy calculations that effectively showed their possible stability [161–163]. On the other hand, these experimental discoveries exposed a weakness in the theoretical approach for predicting HP phases, based on guessing the candidate structures. Indeed, this method might miss unsuspected more stable structures whereas structures found statically stable could be *unphysical* due to the occurrence of dynamical instabilities. So, the theoretical approach was prompted for improvement, and among other optimization, phonon dynamics was included in the calculations. The principle of the “dynamical” approach consists in calculating the phonon dispersion curves of the HP phases, and following their evolution with pressure [169]. For the $\mathrm{A}^N\mathrm{B}^{(8-N)}$ octet family, in the low-pressure range these calculations found the systematic absence of the NaCl phase for more covalent members and the absence of the β-Sn phase for more ionic members [11], in line with the experimental findings of the 90’s. For the higher pressure range these theories predicted the non-existence of the CsCl phase for the more ionic octet compounds and proposed possible alternatives structures: the InBi-type and the AuCd-type [12].

8.3.3 Site (chemical) ordering

A site-ordered structure can be defined as a structure where different atomic species occupy distinct atomic positions with an average occupancy of 1 whereas in site-disordered structures different atomic species can occupy the same atomic position with a fractional occupancy. For example, in the site-ordered zincblende structure of InAs, Indium atoms are in atomic position 4(a) with an average occupancy of 1, and Arsenic atoms are in atomic position 4(c) with an average occupancy of 1 (Figure 8.10). In the site-disordered zincblende structure of InAs, both Indium and Arsenic could be in position 4(a) and 4(c) with an average occupancy less that 1 in order to conserve the right density (Figure 8.11). The disordered structure then is quite similar to a monoatomic structure. Therefore, the ordered structures are less symmetric and the diffraction patterns present

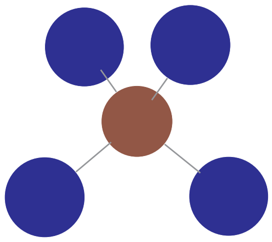

Figure 8.10: Drawing of the site-ordered InAs in the zincblende structure.

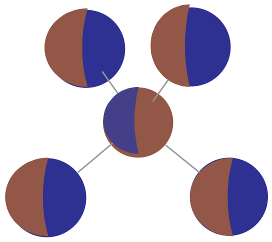

Figure 8.11: Drawing of a possible configuration of site-disordered InAs in the zincblende structure.

the so called “difference reflections”. These reflections are those in which the two different atomic species scatter in anti-phase, with the result that the reflection intensity depends solely on the difference of the scattering power of the atoms. The difference reflections in InSb, for example, are extremely weak (since In has Z = 49 and Sb has Z = 51), while in HgO, for example, these reflections are nearly as strong as those in which the two species scatter in phase. The observation of difference reflections is required to demonstrate site ordering. This is difficult to do in binary systems where the two atomic species have very similar scattering powers, and at HP because of the inevitable broadening of diffraction peaks.

8.4 Structures at high-pressure

β-Sn

The β-Sn structure is found in elemental Sn above 291 K at atmospheric pressure. The structure is shown in Figure 8.12. It is tetragonal, space-group $I4_1/amd$, with atoms on the 4(a) positions at (0, 0, 0), (0, 1/2, 1/4), etc.. The structure is centrosymmetric. The general reflection conditions are $h + k + \ell = 2n$ in $hk\ell$, h and $k = 2n$ in $hk0$,

$2h + \ell = 4n$, and $\ell = 2n$ in $hk\ell$. The location of the atoms on the 4(a) special positions gives the further condition $2k + \ell = 2n + 1$ or $4n$ in $hk\ell$.

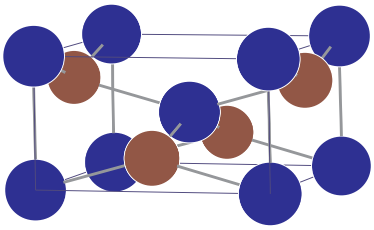

Figure 8.12: Diatomic β-Sn structure.

CsCl

The CsCl structure has not yet been found in any of the II-VI or III-V systems (except in InSb [170]), but, as seen, is expected to occur as a very high-pressure phase. It is centrosymmetric cubic, space-group $Pm3m$ with the two atomic species on the 1(a) and 1(b) sites at (0, 0, 0) and (1/2, 1/2, 1/2), respectively. The structure has perfect eight-fold coordination, with eight identical next-nearest neighbours, and it is shown in Figure 8.13. There are no reflection conditions, but reflections with $h + k + \ell \neq 2n$ are difference reflections.

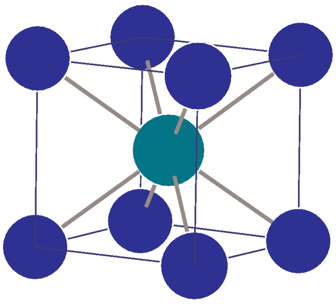

Figure 8.13: CsCl structure.

8.4.1 Orthorhombic structures

Cmcm

Cmcm is a structure that was previously unobserved in binary materials but that has become increasingly important in recent studies of semiconductors at HP. It, or a very similar structure, has been found so far in AlSb, GaP, GaAs, InP, InAs, ZnSe, ZnTe, CdS, CdSe, CdTe, HgSe, and HgTe. The *Cmcm* structure can be viewed as an orthorhombic distortion of NaCl with the two atomic species on 4(c) sites of space-group *Cmcm* at (0, y_1, 1/4) and (0, y_2, 1/4), respectively. The reflection conditions are $h + k = 2n$ in $hk\ell$, and h and $\ell = 2n$ in $h0\ell$. If $a = b = c$, $y_1 = 3/4$, and $y_2 = 1/4$, then the structure is identical to NaCl. The principal distortion from NaCl is a displacement along $\pm y$ of alternate $x - y$ NaCl planes. There is a second, smaller distortion if $\Delta y = y_1 - y_2 \neq 0.5$ which results in a $\pm(0.5 - \Delta y)/2$ zigzag along the x-axis chains. The *Cmcm* structure is shown in Figure 8.14. The way in which the coordination of the *Cmcm* structure differs from NaCl depends critically on the values of the lattice parameters and the variable atomic coordinates. The diffraction pattern of *Cmcm* differs from that of NaCl in two major respects:

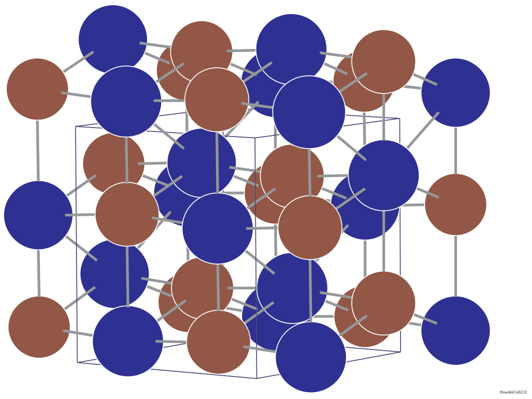

Figure 8.14: *Cmcm* structure: atomic positions [0, 0.65, 0.25]; [0, 0.18, 0.25].

1. The orthorhombic distortion results a splitting of the NaCl peaks — for example, the NaCl (200) splits into (200), (020), and (002) of *Cmcm*.

2. The displacement of the alternate NaCl layers along $\pm y$ result in the appearance of additional reflections — principally (021) and (221) — the intensity of which are directly related to the degree of displacement.

8.5 Overview of high pressure work on InAs

The model system we have examined to experimentally verify the prediction of the recent "dynamical" calculations, that is the absence of CsCl phase at HP and the presence of alternative structures like the InBi-type and the AuCd-type, is indium arsenide (InAs) because it is among the more ionic III-V semiconductors and has the lowest predicted transition pressure to CsCl.

8.5.1 Experimental studies

An overview of experimental HP work on InAs may be found in [10]. InAs has a ZB structure at ambient pressure with a = 6.0583 Å. The first work under pressure of InAs is a resistivity measurement of Minomura and Drickamer in 1962 [43]. According to this first study, in the low pressure region the rapid increase of the resistance with pressure is followed by a sharp decrease in resistance at the phase transition at $\sim$ 10 GPa. The resistivity of the HP phase is of the order of 10^{-4} Ω·cm and decreases slowly with increasing pressure up to 20 GPa. A subsequent resistivity study found the transition at P = 6.9(2) GPa [171]. In Raman scattering studies on single-crystal InAs under hydrostatic pressures [172], phonons are seen at 7 GPa but the Raman signal disappears abruptly at metallization at 7.15 GPa. The first structural study on InAs dates to the work of Jamieson in 1963 [157]. His diffraction study shows that this transition is to an NaCl structure with a volume collapse of 18.8%. HP study on InAs has been extended to 27 GPa by the work of Vohra *et al.* by using EDXRD in a diamond anvil cell using SR [173]. This study confirms the ZB → NaCl transformation at P = 7.0(2) GPa and finds a further transformation at P = 17.0(4) GPa to the β-Sn-type structure with increasing pressure. The ZB → NaCl phase transition, which is associated with metallization, is accompanied by a 17% volume collapse while the NaCl → β-Sn transformation has no volume discontinuity within the experimental errors. The β-Sn was found to be stable up to P = 27 GPa. Vohra *et al.* were unable to determine whether or not the NaCl and β-Sn structures were site-ordered. This work was the first observation of a ZB → NaCl → β-Sn structural sequence under HP on a III-V compound at that time. During the 90s there has been a re-investigation of the structural systematics of the core II-VI, III-V, and group IV semiconductors under pressure using the image-plate technique for ADXRD study with SR [164]. ADXRD studies on InAs of Nelmes *et al.* [166] report the transition to NaCl at P = 7 GPa, in agreement with the other studies. However, this phase seems to be stable up to only 9

GPa. The shoulder developed by the (200) NaCl reflection and other features appearing with increasing pressure are similar to those observed in the NaCl → *Cmcm* transitions found in CdTe and InP. Therefore, according to this work, InAs transforms to a *Cmcm* structure at 9 GPa. The issue of chemical ordering of the HP NaCl or *Cmcm* phase is not well addressed. Although the (111) and (311) difference reflections have been found to be present – showing the NaCl phase to be site-ordered – their relative intensities are a factor of 2 weaker than they should be.

8.5.2 Theoretical studies

The fundamental nature and technological importance of the elemental and binary semiconductors have made their HP behaviour one of the most active areas of HP research. The structural results that have followed these studies have prompted many computational studies, from which a general understanding of the main features of the structural systematics has developed. The first calculations done are based on the total energy approach. In 1978, Soma found that III-V semiconductors generally have stable NaCl and β-Sn structures at HP, and for InAs predicted a transition to the NaCl phase in a pressure interval between 1.1 and 1.5 GPa [174]. Zhang and Cohen also predicted this phase transition, but at the pressure of 8.4 GPa [159]. After the experimental discoveries of the 90s that showed the systematic absence of the NaCl (β-Sn) phase in the more covalent (ionic) compounds, the newly discovered orthorhombic phases were included in the theory. In this scenario, Mujica and Needs [163] showed that the structural sequence of stable phases for InAs is: ZB → NaCl → *Cmcm* → *Immm* → CsCl. The ZB → NaCl coexistence pressure is calculated to be 3.9 GPa. The *Cmcm* distortion of the rocksalt structure appears in the pressure range 3.0-4.5 GPa. From a synthesis of these data it is, therefore, difficult to say whether there is any region of stability for the rocksalt structure at all. The calculated transition from NaCl to *Cmcm* is predicted to be second order or extremely weakly first order. At higher pressures they predict transitions from *Cmcm* to *Immm* at about 24.0(2.5) GPa and then to the CsCl structure at 67.0(1.2) GPa. This theoretical approach was improved with the introduction of dynamic phonon calculations. Using this new approach, Kim *et al.* [12] have shown that for InAs, the CsCl-type structure has phonon instabilities that prevent its formation. From symmetry analysis of the soft phonon mode the authors propose two HP structures that replace the CsCl phase in the HP phase diagrams of III-V semiconductors:

i. the oP4 (AuCd structure-type) with space-group *Pmma*,

ii. the tP4 (InBi structure- type) with space-group *P4/nmm*.

8.6 Combined XRD and XAS study of InAs at room temperature

The aim of our study is two-fold:

i. In the unexplored pressure range: verify the non existence/existence of the HP CsCl structure and eventually, the existence/non-existence of the alternative structures proposed by recent theoretical calculations. The local structure in these different phases changes dramatically: from 8 *alike* nearest neighbours in the CsCl structure to 4 *unlike* and 4 *alike* in the InBi structure.

ii. In the whole pressure range: address properly the question of chemical ordering.

XAS can identify the local structure and the degree of short range chemical (site) ordering since it probes selectively the local environment of the absorber atom and it is sensitive to the nature of the surrounding atoms. Therefore XAS is, in principle, able to address both points. Neverthless, XRD is the principal tool for the identification of new symmetries. Therefore, we will demonstrate that the combination of XRD and XAS is essential to fully identify the HP phases.

8.6.1 XRD experiment

The XRD measurements have been carried out at the dedicated XRD beamline of ESRF for HP studies, ID30. The InAs sample consisted of a fine powder ground from 99.9999% purity polycrystalline stock (Alfa). The sample was loaded into a Chervin-type DAC fitted with 150 μm bevel-edged diamonds employing a stainless steel gasket. The pressure was measured with ruby chips using the fluorescence method [62]. The data have been recorded at room temperature and using two different PTM (Silicone oil and Nitrogen to improve hydrostaticity). The maximum pressure reached was 80 GPa for the run with Silicone oil, and 46 GPa for the run with Nitrogen. Wavelength selection was made using an Si (111) monochromator tuned to $\lambda = 0.3738(1)$ Å calibrated against the I K-edge (E = 33.169 keV). The beam was focused by Kirkpatrick-Baez mirrors, to a size of 15 μm x 15 μm FWHM. Patterns were recorded using a MAR345 image plate detector with 100 μm pixel resolution. The sample-detector distance was calibrated by an NBS Si-filled gasket at the same sample position. Two-dimensional image plate data were corrected for spatial distortion and integrated with FIT2D [175] to produce a 2θ-I pattern.

8.6.2 Results and discussion

Typical integrated XRD data collected using Silicone oil up to 80(20) GPa and using N_2 up to 46(3) GPa are shown in Figure 8.15. The data show the following structural sequence: ZB → NaCl → *Cmcm* → *"New phase of lower symmetry"*. This sequence is preserved for the two PTM, although the onsets of transitions are at slightly different pressures. The diffraction pattern obtained with Silicone oil are affected by a high non-hydrostatic conditions, leading to:

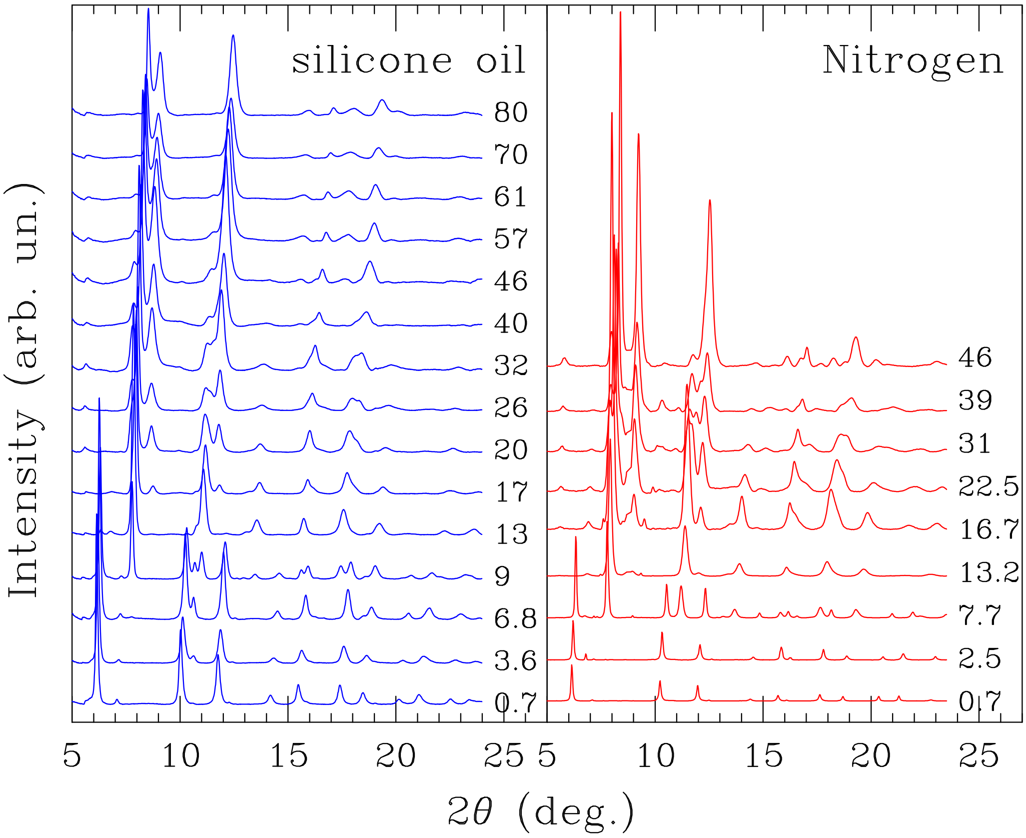

Figure 8.15: XRD patterns of InAs recorded with Silicone oil/Nitrogen (*left panel/right panel* respectively) as PTM at selected pressure points.

i. a broadening of the diffraction peaks;

ii. larger phase coexistence regions; and

iii. shifts in the pressure values for the transition onsets.

Zincblende → NaCl transition

InAs crystallizes with a zincblende structure at ambient pressure. According to previous studies, at $\sim$ 7 GPa it undergoes a phase transition to NaCl. However, this transition seems to be complex, and strongly depends on the PTM, which, as is well known, strongly influences the hydrostatic conditions in the cell. The data recorded using Silicone oil (Figure 8.16 a)) show the appearance of the NaCl (200) peak at 6.8(4) GPa and the NaCl (220) and (222) start to occur at 7.3(5) GPa. On the other hand, the profile using Nitrogen (Figure 8.16 b)) shows an approximately 50:50 ZB/NaCl mixture at 7.7(1) GPa.

NaCl → *Cmcm* transition

Figure 8.17 shows the transition from NaCl to *Cmcm*. In the data collected using Silicone oil (Figure 8.17, *upper panel*), at 12.8(7) GPa, besides the peaks attributed to ZB and NaCl, there is a reflection at $\sim$ 8.5 deg. that is indexed as the (021) peak of *Cmcm*. When the pressure is increased to 14(1) GPa the (021) of *Cmcm* increases and the (220) reflection of NaCl at $\sim$ 11.5 deg. develops a shoulder that is indexed as the *Cmcm* (221) reflection; however, at this pressure the ZB (111) peak is still present. In the data using Nitrogen (Figure 8.17, *lower panel*), we observe the co-existence of ZB and *Cmcm* at 9.2(1) GPa. Therefore, from these observations it is not sure that any single region of pure NaCl phase exists, and probably NaCl does not exist as a discrete phase at room temperature indicating the incipient instability of the NaCl TA(X) phonon [11]. This result is consistent with the results reported in [168].

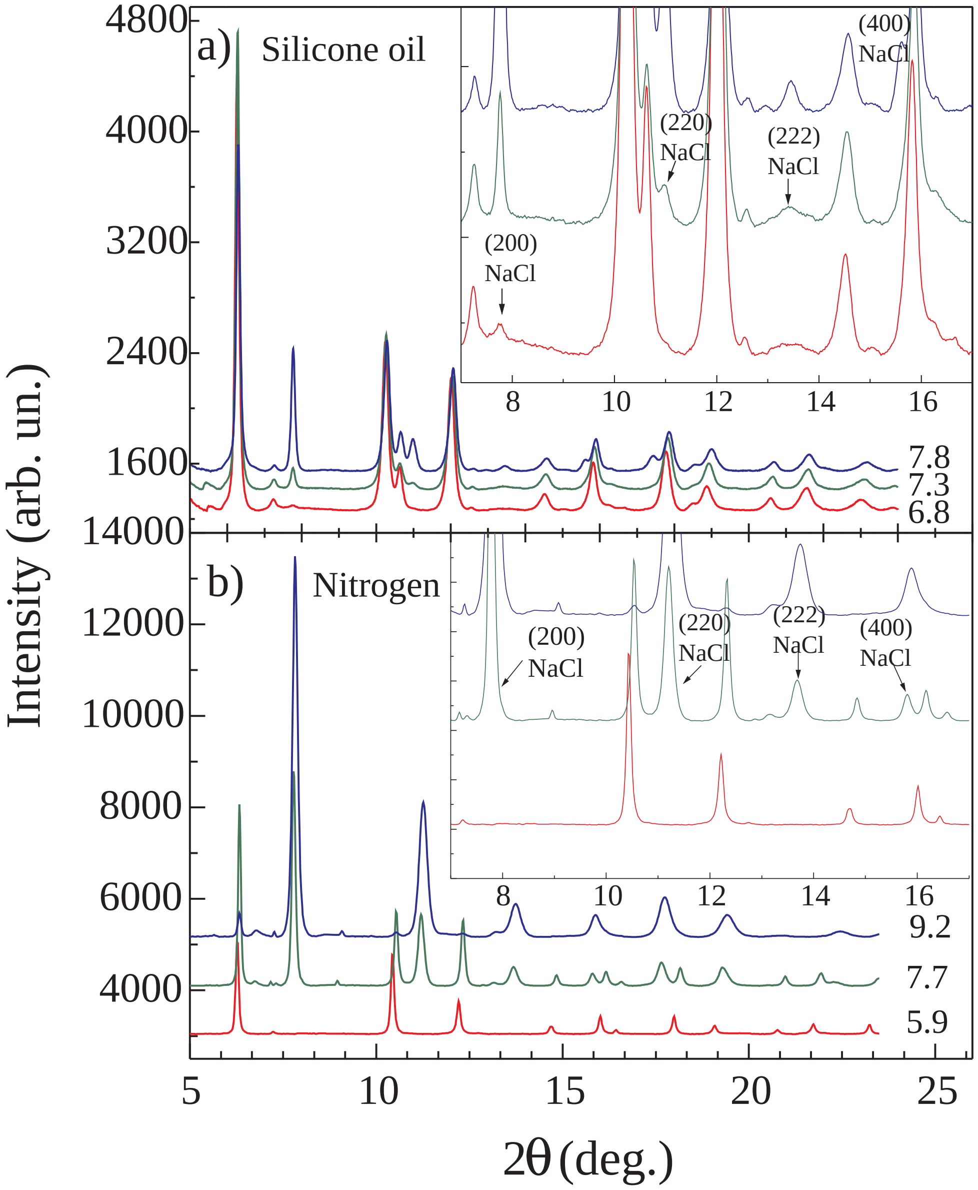

Figure 8.16: a) Transition from ZB to NaCl in the data recorded using Silicone oil as PTM. The inset shows the appearance of the NaCl (200) reflection at 6.8(4) GPa, of NaCl (220), and NaCl (222) at 7.3(5) GPa, and of NaCl (400) at 7.8(5) GPa. b) Transition from ZB to NaCl in the data recorded using Nitrogen as PTM. The pattern at 7.7(1) GPa shows an approximately 50:50 ZB/NaCl mixed phase.

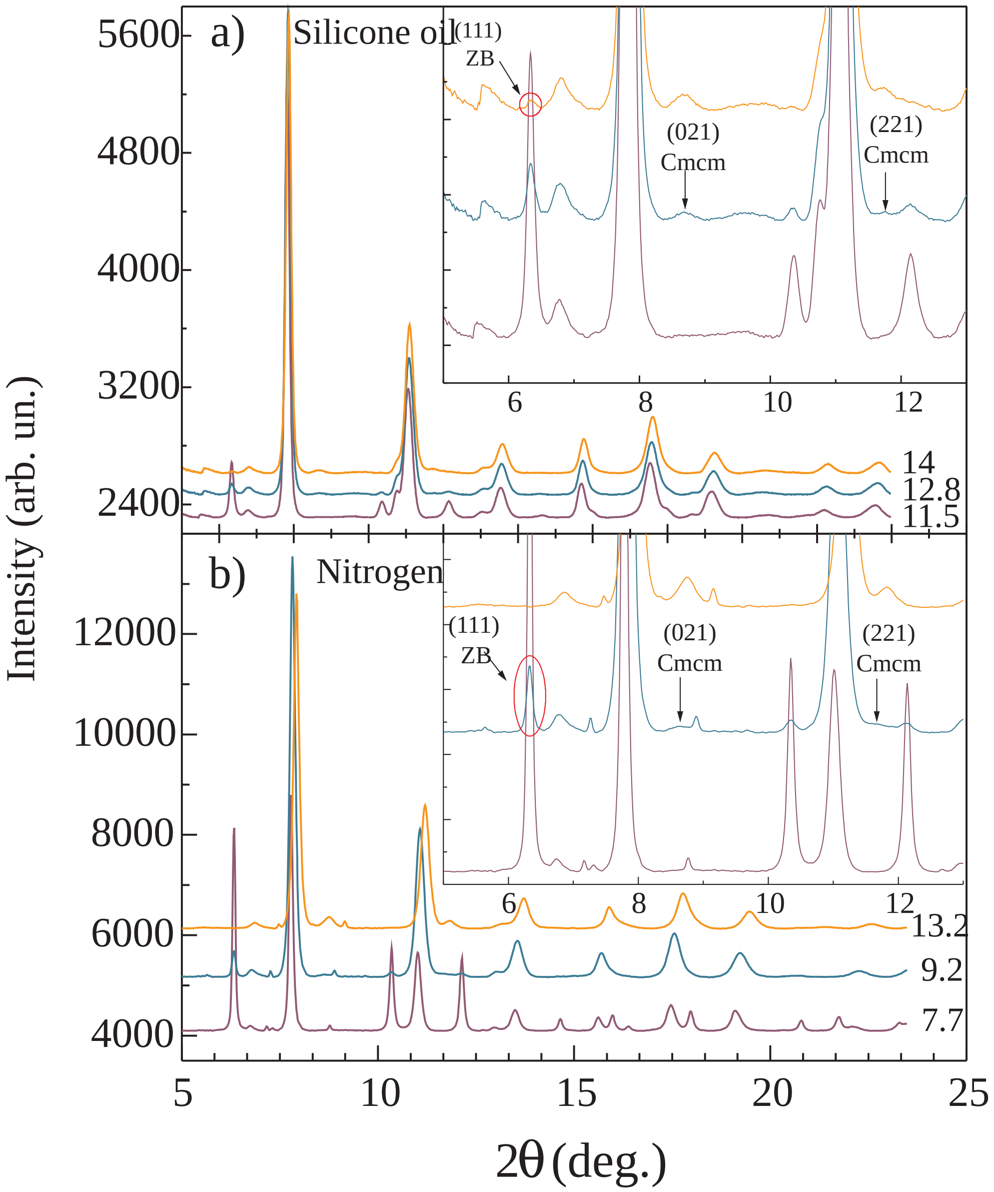

Figure 8.17: a) Transition from NaCl to *Cmcm* in the data recorded using Silicone oil as PTM. The inset shows the appearance of the (021) and (221) peaks of *Cmcm* at 12.8(7) GPa and the (111) reflection of ZB at 14(1) GPa. b) Transition from NaCl to *Cmcm* in the data recorded using Nitrogen as PTM. The inset shows at 9.2(1) GPa the co-existence of reflections attributed to the ZB and *Cmcm* phases.

Cmcm → *"New phase of lower symmetry"* transition

The left panel of Figure 8.18 shows XRD profiles of the Silicone oil data in the pressure range from 28 GPa to 80 GPa and the right panel shows the patterns from 25 to 46 GPa recorded using Nitrogen. Both datasets show a phase transition from the *Cmcm* phase to a *phase of lower symmetry.* This new phase presents new Bragg reflections at ~ 16, 17.5 and 20 deg., indicated by arrows in Figure 8.18, which are forbidden by the C-centering condition in *Cmcm* space-group. These new reflections are rather broad in the Silicone oil data because of the non-hydrostatic conditions in the cell volume, and are reasonably well defined and intense in the data recorded using Nitrogen.

We point out that since the trends in the previous *Cmcm* peaks are continued in the new phase, the most likely new phase is a subgroup of *Cmcm.* The simplest and most straightforward mechanism to produce a lower symmetry subgroup of *Cmcm* is to loose the C-centering condition. When the structure distorts such as to break the C-centering symmetry, the displacements involved in this transition will put intensity into "new reflections" that are forbidden by the C-centering condition. With this thesis in mind, we therefore tried to index this HP phase with the most likely phases obtainable by distortions of *Cmcm*, therefore belonging to subgroups of *Cmcm.* The best Le Bail results were obtained with *Pmma* symmetry[1]. We recall here that the *Pmma* was one of the proposed structures by the recent theories based on dynamical calculations.

In the data recorded using Silicone oil we can identify the new reflection at ~ 16 deg. at 33 GPa whereas in the data collected with Nitrogen the same peak is clearly visible at 35 GPa. The new reflections at ~ 17.5 deg. and at ~ 20 deg. in the data using Silicone oil are visible at 40 and 52 GPa respectively, whereas in the data recorded using Nitrogen the same two new reflections are both visible at 46 GPa. The peaks at ~ 16 and 17.5 deg. can be indexed as the (321) and (401) reflection of *Pmma* respectively, whereas the peak at ~ 20 deg. results from the superposition of (005), (421) and (332) *Pmma* reflections.

---

[1] Although the notation *Pmcm* (obtained through loss of C-centering of *Cmcm*) shows more directly the distortion from *Cmcm*, we have opted for the *Pmma* notation, which is the standard setting for space-group 51. It is identical to *Pmcm* after transforming a b c → b c a.

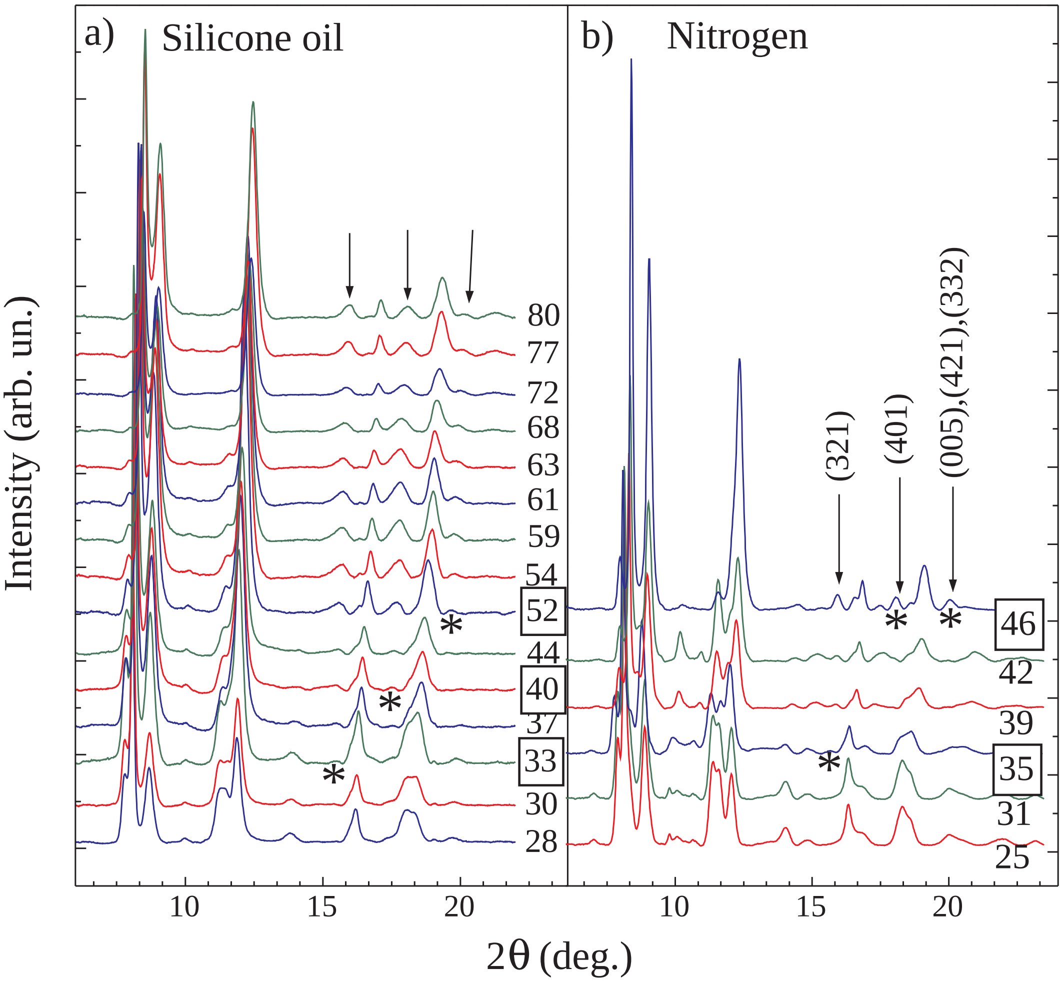

Figure 8.18: Transition from *Cmcm* to *Pmma* in the data collected using Silicone oil (*left panel*) and Nitrogen (*right panel*) as PTM. The arrows indicate the new reflections forbidden by the C-centering condition of the *Cmcm* space-group. In the data recorded using Nitrogen the new peaks are indexed. The stars indicate the appearance of the new *Pmma* peaks.

Quantitative analysis

All the data have been analyzed with the Rietveld method [152] using the GSAS package [176]. The high degree of non-hydrostaticity that affects the data recorded with Silicone oil at pressures above $\sim$ 40 GPa leads to a difficult refinement obtaining unstable cell parameters if they refine close to a tetragonal condition, which is the case for the *Cmcm* ($a \simeq c$) and for *Pmma* ($a \simeq b$) symmetries of InAs. For this reason, we report all the structural parameters relative to the data recorded using Nitrogen as PTM. The refinement variables include: background using the Chebyshev function of the first type, profile parameter using a pseudo-Voigt function [177, 178], scale factor, spherical harmonics preferred orientation [179], cell parameters and atomic positions (for *Cmcm* and *Pmma* symmetries).

Figure 8.19 shows the volume per unit cell as a function of pressure normalized to the volume at room pressure. In the first phase transition we observe a volume reduction of $\sim$ 18%, while no volume discontinuities are associated to the latter phase transitions.

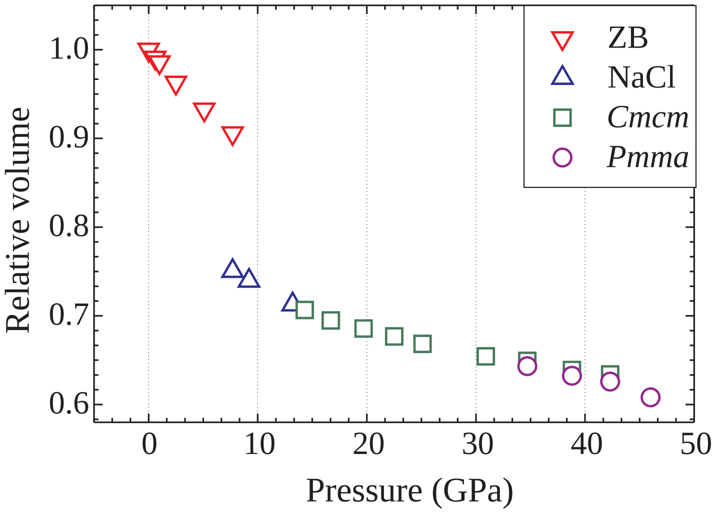

Figure 8.19: Relative volume of InAs versus pressure for Nitrogen data. A change in volume of $\sim$ 18% is associated to the ZB → NaCl transition. No obvious volume discontinuities are observed in the other phase transitions.

Figure 8.20 shows the cell parameters of InAs as a function of pressure. We point out that although the NaCl → *Cmcm* transition onset is at 9.2(1) GPa (as shown in Figure 8.17 b)) the (021) and (221) peaks are not fittable, so the pattern at 9.2 GPa has been fitted using NaCl symmetry. The best refinements from 13.5 GPa to 31 GPa result in an orthorhombic cell in space-group *Cmcm*. From 34 to 42 GPa we have fitted the data using a mixed *Cmcm* and *Pmma* phase. Only the data point at 46 GPa has been fitted using a pure *Pmma* phase.

As already discussed in paragraph 8.4.1, the *Cmcm* structure is an orthorhombic distortion on the NaCl structure. In fact, the best refinements for the data points at 13.5 and 16.7 GPa result in values of cell parameters close to those relative to a cubic symmetry. As the pressure increases, the orthorombic distortion becomes more evident with an increasing deviation of the cell parameters from the values relative to a cubic structure. The atomic positions of In and As in the *Cmcm* structure are (0, y_1, 1/4) and (0, y_2, 1/4) respectively. The deviation of y_1 and y_2 from 3/4 and 1/4 (values that correspond to the NaCl structure, see paragraph 8.4.1) is a further indication of the increase of the distortion of the *Cmcm* structure with respect to the NaCl as a function of pressure (Figure 8.21). The refinement of the data at 46 GPa required us to have a structurally disordered *Pmma* with four internal parameters not mutually coupled by symmetry (each atom must have lower symmetry in order to yield the correct density with respect to the multiplicity of each site). These effects are probably related or directly induced by a local chemical disorder, but we are not able to conclude on this point using XRD alone since Rietveld refinements based on a site-disordered model yields statistically equivalent fits. The structural parameters of the data at 46 GPa are: $a = 4.8931(18)$, $b = 5.1069(4)$, $c = 5.4117(9)$, and atomic positions at [In 2f: 1/4, 1/2, 0.1065(28)], [In 2e: 3/4, 0, 0.3735(20)], [As 2f: 1/4, 1/2, 0.5570(21)], [As 2e: 3/4, 0, 0.8776(25)]. Figure 8.22 shows the Rietveld refinement at 46 GPa.

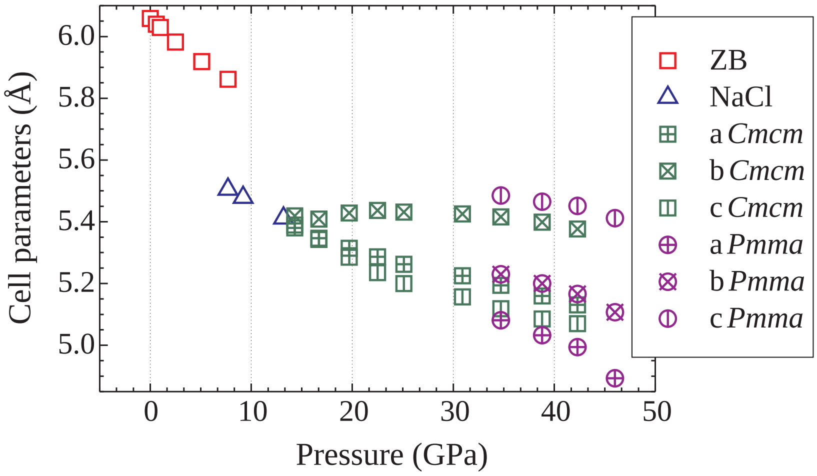

Figure 8.20: Cell parameters versus pressure of different phases of InAs.

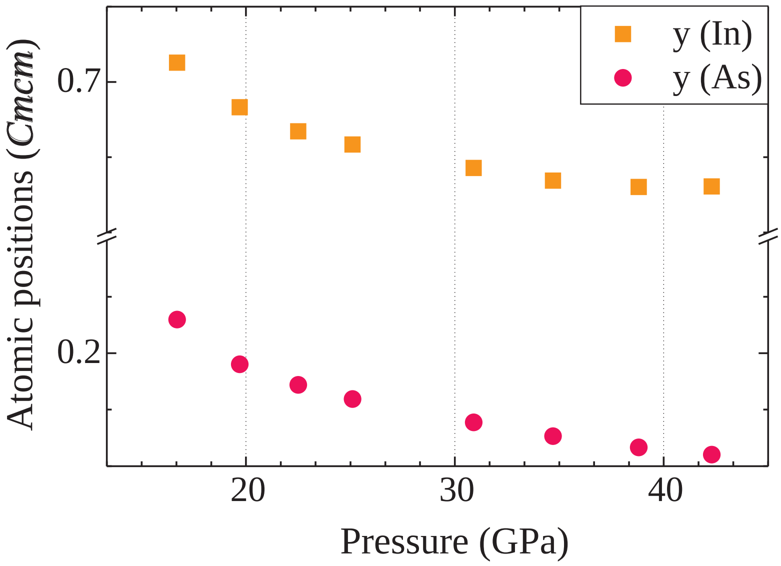

Figure 8.21: y values for In and As in *Cmcm* structure for InAs as a function of pressure.

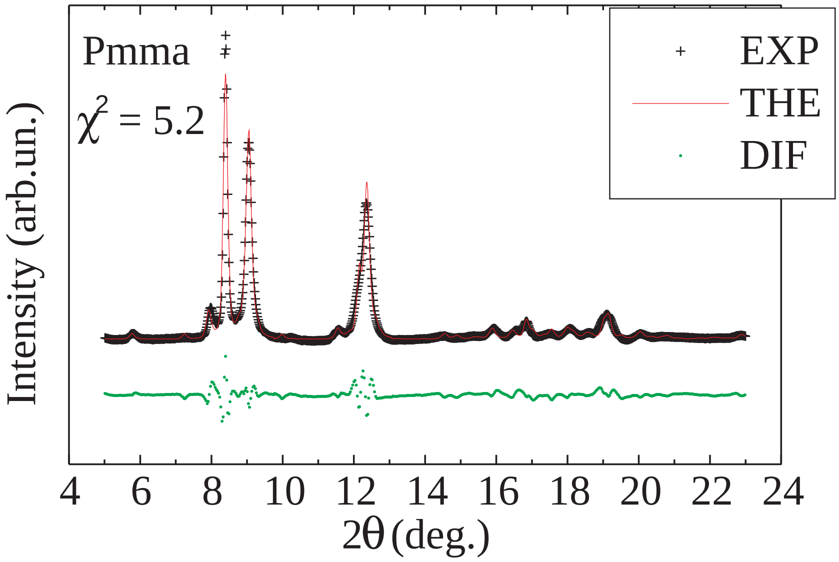

Figure 8.22: Rietveld refinement and normalized χ^2 value for the profile at 46 GPa: (EXP: data, THE: fit, DIF: difference).

8.6.3 XAS experiment

The XAS measurements have been carried out at the dispersive EXAFS beamline of ESRF, ID24. The InAs sample consisted of a fine powder ground from 99.9999% purity polycrystalline stock (Alfa). The sample was loaded into a Chervin-type DAC fitted with Standard Drukker diamonds with 320 μm flats. The pressure was measured with ruby chips using the fluorescence method [62]. The data have been recorded at room temperature using Silicone oil as PTM. The maximum pressure reached was 50 GPa. The thickness of the sample was $\sim$ 35 μm. The beam was focused on the sample of 150 μm of diameter. Figure 8.23 shows the horizontal profile of the focal spot using a Bragg polychromator crystal at the As K-edge (E = 11.867 keV). An important asymmetric tail arising from penetration depth effects is visible at high energies. This tail precludes the use of the Bragg geometry for very HP applications (P $\geq$ 50 GPa) at high energies (E $>$ 10 keV).

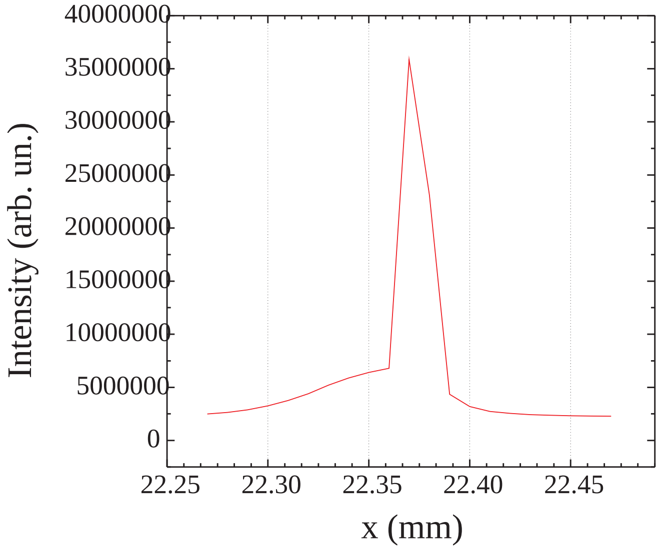

Figure 8.23: Horizontal profile of the focal spot obtained using the Bragg crystal at As K-edge (E = 11.867 keV).

8.6.4 Results and discussion

Qualitative description of data and evolution with pressure

Raw As K-edge XAS spectra corresponding to different local atomic arrangements (at 7, 11, 14, 20 and 50 GPa) are reported in Figure 8.24. The spectrum at 7 GPa is that of the

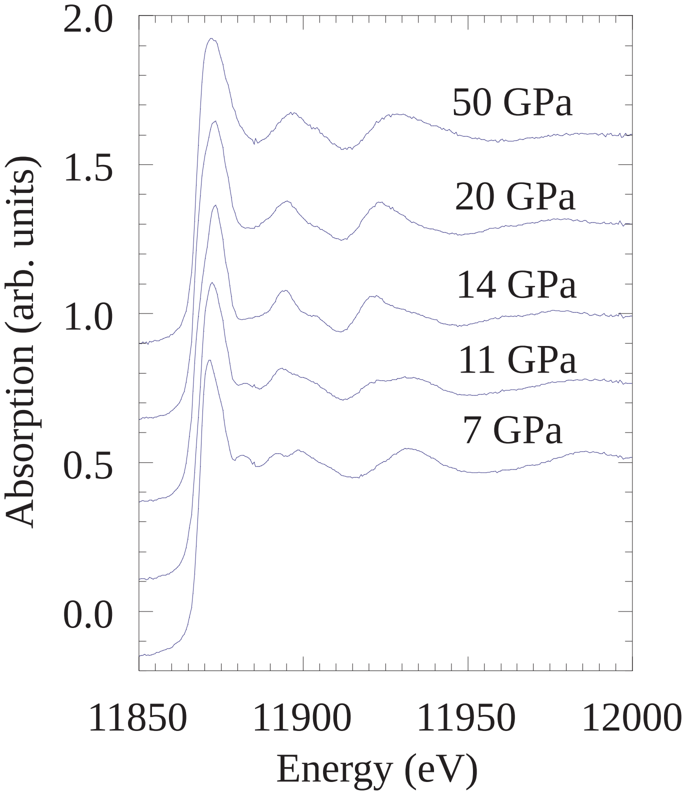

Figure 8.24: Raw As K-edge XAS spectra at different pressures.

semiconducting zincblende phase of InAs. At 14 GPa, the open four-fold coordinated structure has collapsed to a more compact and dense six-fold coordinated structure. The changes in the local environment of As are well reflected by the modifications of the EXAFS (Figure 8.25). The first shell signal has been extracted and analyzed using the FEFF7 code. *Ab initio* phases and amplitudes have been used to simulate the In-As interaction potential and scattering properties respectively. Results of the best fits are also shown in Figure 8.25. The first shell signals in the spectra at P = 7 GPa and at P = 15 GPa are well reproduced respectively by 4 In atoms at $R^{(sc)}_{As-In} \sim 2.5$ Å and 6 In atoms at $R^{(met)}_{As-In} \sim 2.7$ Å. At intermediate pressure (i.e. 11 GPa), the EXAFS signals can be well reproduced by a linear combination of these two configurations. Figure 8.26 reports the edge regions of the spectra (*left panel*) and their derivatives with respect to energy (*right panel*). A gradual but important ($\Delta E \sim -1.6(1)$ eV) shift in the onset of absorption (taken as the energy position corresponding to the maximum in the derivative and marked by an arrow in Figure 8.26 *right panel*) occurs between the

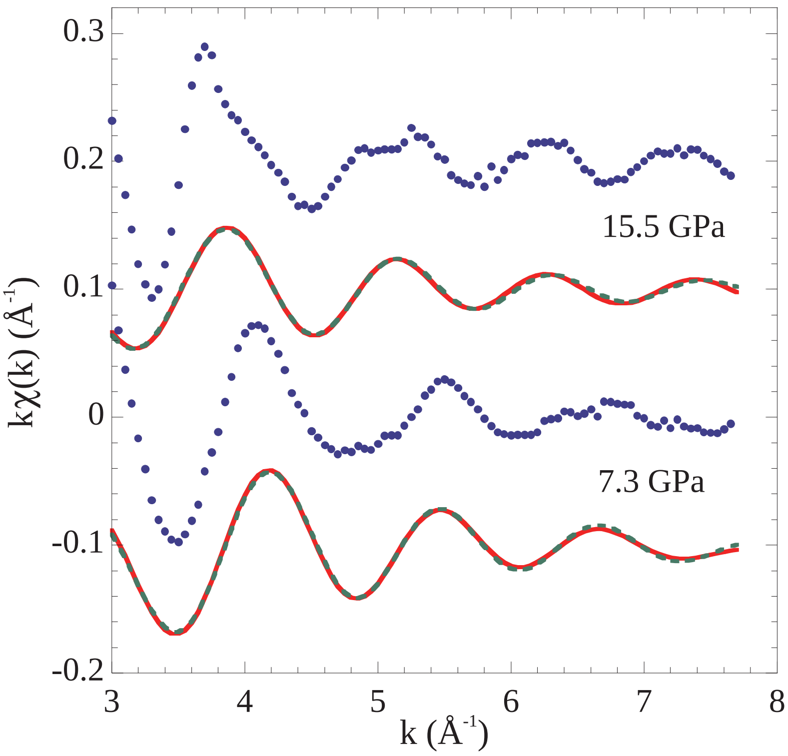

Figure 8.25: EXAFS (*dots*), first shell signal (*red lines*) and fit (*green dashes*) in the semiconducting (7.3(5) GPa) and metallic (15(1) GPa) phases respectively.

four-fold and the six-fold coordinated phases, indicating that the electronic structure of the HP phase has a metallic character, in agreement with previous findings. The value of ΔE as a function of pressure is reported in Figure 8.27. The evolution of ΔE with pressure can be used to identify three distinct pressure regions in which the electronic properties of InAs differ: P $<$ 9 GPa (light grey) semiconducting InAs, 9 GPa $<$ P $<$ 14 GPa (medium grey) coexistence of semiconducting and metallic InAs, P $>$ 14 GPa (dark grey) metallic InAs. After this phase transition, that XRD shows to be first order, the EXAFS shows only very subtle modifications (Figure 8.24), namely:

i. gradual loss of the high-energy shoulder on the first oscillation at $\sim$ 11.9 keV;

ii. a decrease of the main frequency;

iii. an overall broadening of the features; and

iv. an attenuation of the intensity of the oscillations.

However, the shape of the absorption edge (white line) and of the XANES region does continue to change at higher pressures, as illustrated in Figure 8.26 *left panel*. The white line in the metallic phase is characterized by a discontinuity in the first derivative (marked by a dot in Figure 8.26 *right panel*). At P ∼ 14 GPa, the discontinuity occurs at E ∼ 11.869 keV. This feature gradually disappears as pressure increases to give the broad and rounded shape of the white line at 50 GPa (Figure 8.26 *left panel*). The evolution with pressure of this region of the spectrum is highlighted by plotting the absorption at a fixed value of the energy as a function of pressure. We have chosen to plot, in Figure, 8.28 the evolution of the absorption at E ∼ 11.869 keV. Discontinuities in this curve may be qualitatively associated to phase transitions, and used to confine phase coexistence regions. These occur at 9.0(5) and 14.0(5) (associated to the semiconductor-metal phase coexistence region, in agreement with Figure 8.27 and at 16.5(5) and 18(1) GPa. A further gradual modification begins at around ∼ 30 GPa, indicating the onset of a new phase.

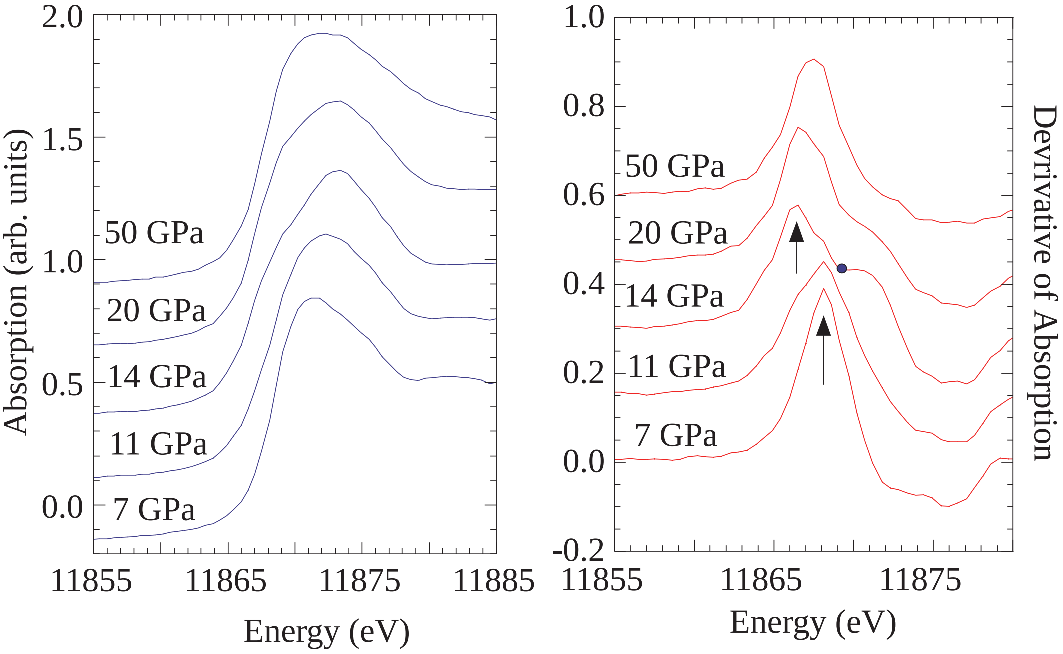

Figure 8.26: *Left panel*: edge region of the spectra. *Right panel*: derivative with respect to the energy. The blue dot indicates a discontinuity in the first derivative of the metallic phase. The arrows indicate a shift of the absorption edge from the semiconducting to the metallic phase.

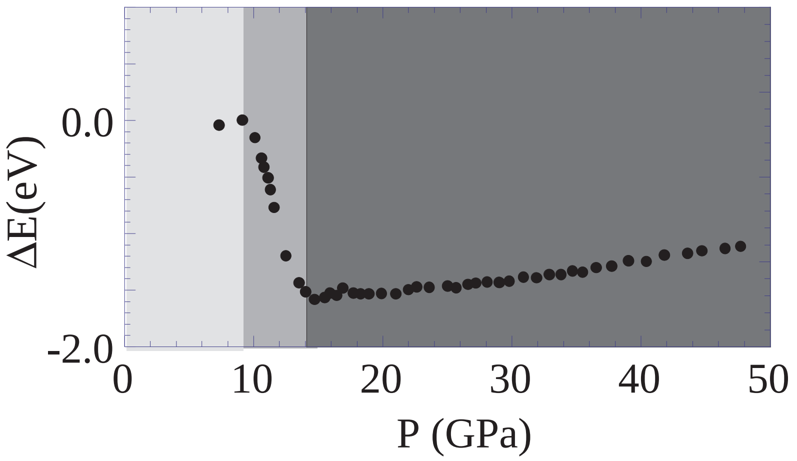

Figure 8.27: ΔE as a function of pressure. The evolution of ΔE with pressure can be used to identify three distinct pressure regions in which the electronic properties of InAs differ: P < 9 GPa (*light grey*) semiconducting InAs, 9 GPa < P < 14 GPa (*medium grey*) coexistence of semiconducting and metallic InAs, P > 14 GPa (*dark grey*) metallic InAs.

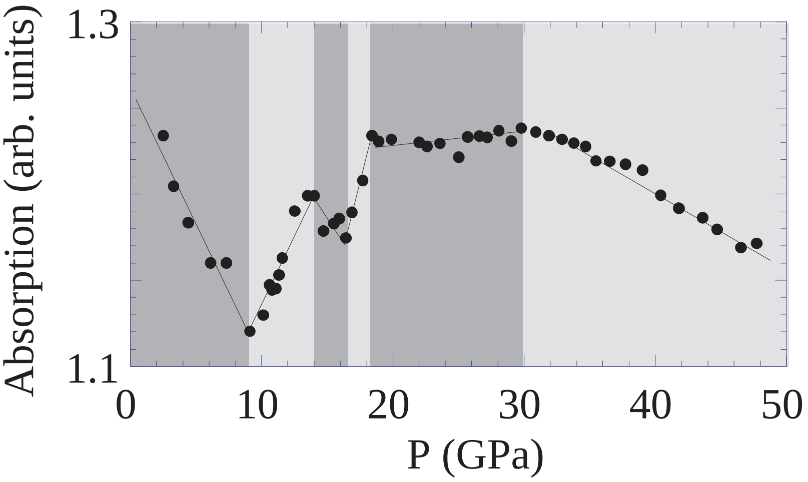

Figure 8.28: Evolution of the absorption at E ~ 11.869 keV. Discontinuities in this curve may be qualitatively associated to phase transitions, and used to confine phase coexistence regions.

XANES simulations: introduction

In principle, a complete recovery of the local geometry and site coordination around As could be obtained from the experimental XANES spectrum. However, the quantitative analysis of this region presents difficulties mainly related to the theoretical approximation in the treatment of the potential and the need for heavy time consuming algorithms to calculate the absorption cross section within the framework of a full multiple scattering approach. We have compared our data to *ab initio* simulations obtained by performing full multiple scattering calculations using the FEFF8 package [153]. We tested several potential models for the fine structure of the XANES, among which a ground state, a Dirac-Hara and a Hedin-Lundqvist potential. Best results were obtained using a self-consistent energy dependent exchange correlation Hedin-Lundqvist potential. For the background function, a ground state potential was used. Self-consistency was obtained by successively calculating the electron density of states, electron density and Fermi level at each stage of the calculation within a small cluster (SCF cluster) centered on the atom for which the density of states is calculated, and then iterating. Full multiple scattering XANES calculations up to a photoelectron wavevector value of $k = 6$ Å^{-1} (corresponding to a photoelectron energy E $\sim$ 130 eV) were carried out for a larger cluster of atoms (FMS cluster) centered on the absorbing atom: all multiple-scattering paths within this cluster were summed to infinite order. We performed simulations for the different observed/predicted phases for InAs in the pressure range up to 80 GPa. We built chemically ordered as well as chemically disordered clusters (`coc` and `cdc` respectively). In the former case the composition of each coordination shell is determined by the group symmetry and by the cell-internal site-occupation of each atom, as defined by a long-range site-ordered structure. In the latter case, a "chemically disordered" local environment around the absorber atom was approached by randomly mixing the chemical composition of each coordination shell in the `coc` clusters. Physically, the values of the first shell As–As and As–In that now appear in the `cdc` cluster ought to be different (see [180]). Unfortunately, it was not possible to have accurate values of the two first shell distances due to the limited k range of the XAS data in the *Cmcm* and *Pmma* phases, and therefore we had to use the only value possible, i.e. the average value obtained fron XRD. Besides the structural information defining the geometry of the cluster, the only external parameters used as input for the simulations were a small constant experimental broadening (`vi0`) and a small offset in the energy scale (`vr0`). No thermal or static disorder factor was added to the simulations.

XANES simulations for the hypothetical HP phase at 50 GPa: clusters obtained from tabulated structures (CsCl, InBi, AuCd phases), with appropriately scaled volumes

We first performed simulations for the proposed HP phases for our data at the highest pressure: the CsCl (*Pm3m*), the InBi (*P4/nmm*) and the AuCd (*Pmma*) phases. The clusters were built based on tabulated structural parameters [181]. The cell parameters a, b, and c were scaled in order to have approximately the same atomic density for InAs in the different phases ($\sim$ 60 atoms in a cluster of radius R = 6 Å). We show in Figure 8.29 the results of these simulations for the `cocs` (red lines) and `cdcs` (green lines). For these simulations, we used SCF and FMS clusters of $\sim$ 30 and $\sim$ 100 atoms respectively. No offset in the energy scale (`vr0` = 0) and a small constant experimental broadening (`vi0` = 0.5 eV) were used. By comparing the simulations in Figure 8.29 with the topmost spectrum in Figure 8.24, we conclude that the local environment around As at 50 GPa is not well described by the CsCl nor by the InBi clusters. However, a strong resemblance to the chemically disordered AuCd cluster can be observed.

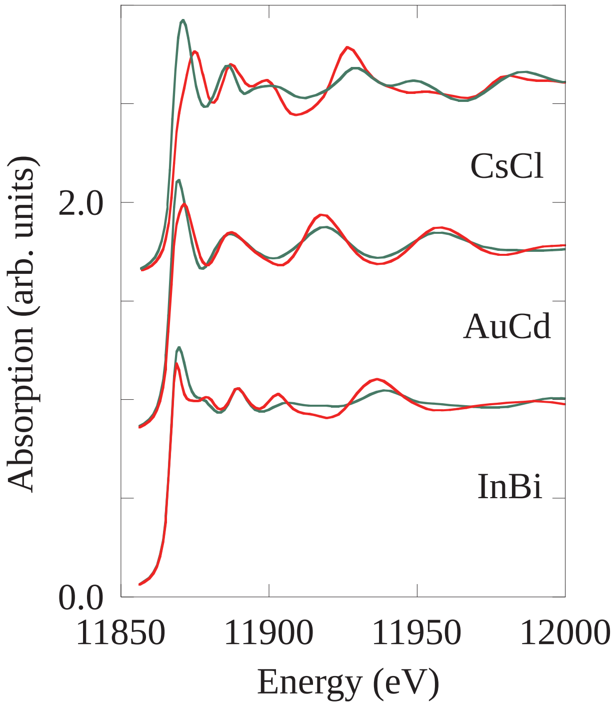

Figure 8.29: Simulated spectra based on the proposed HP phases for InAs: CsCl, AuCd and InBi. *Green/red* lines correspond to chemically-disordered/ordered clusters respectively.

XANES simulations for the observed phases: clusters obtained from Rietveld refinements of our XRD data

The structural parameters used to build the clusters were obtained from the Rietveld refinements of our XRD data. Calculations were performed for the zincblende at 7.3 GPa, the NaCl at 15 GPa, the *Cmcm* phase at 20, 25 GPa, and 40 GPa and for the *Pmma* phase at 40 GPa and at 60 GPa. For all phases, the simulations were performed for both `coc` and `cdc`. We show in Figure 8.30 the results of these simulations for the `cocs` (red lines) and `cdcs` (green lines) for NaCl at 15 GPa, *Cmcm* at 25 GPa, and *Pmma* at 40 GPa. In Figure 8.31 we show the simulations that best correspond to our data, which are, in order of increasing pressure:

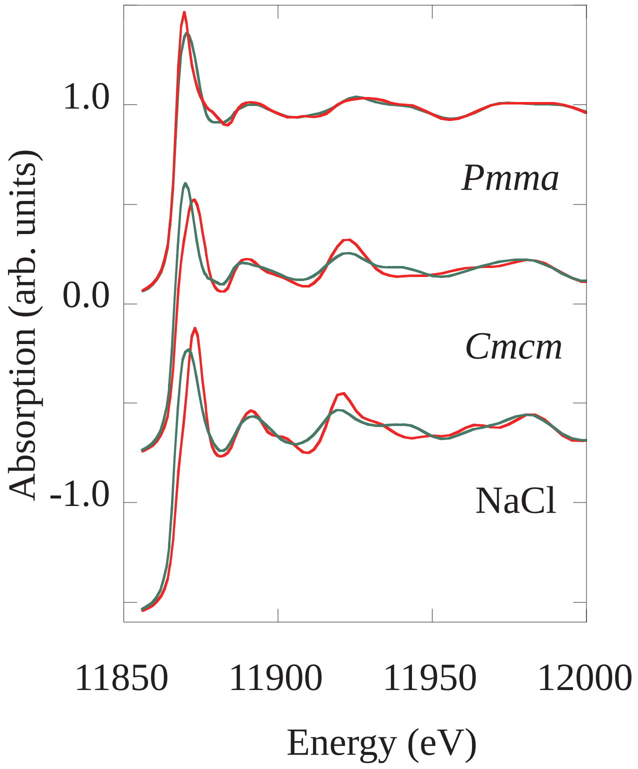

Figure 8.30: Simulated spectra of short-range chemically-ordered/disordered (*red/green lines*): NaCl at 15 GPa, *Cmcm* at 25 GPa, and *Pmma* at 40 GPa.

i. ZB at 7 GPa,

ii. short-range chemically-ordered (sr-co) NaCl at 15 GPa,

iii. short-range chemically-ordered (sr-co) *Cmcm* at 25 GPa,

iv. a 50% linear combination of short-range chemically-ordered (sr-co) *Cmcm* and short-range chemically-disordered (sr-cd) *Pmma* at 40 GPa.

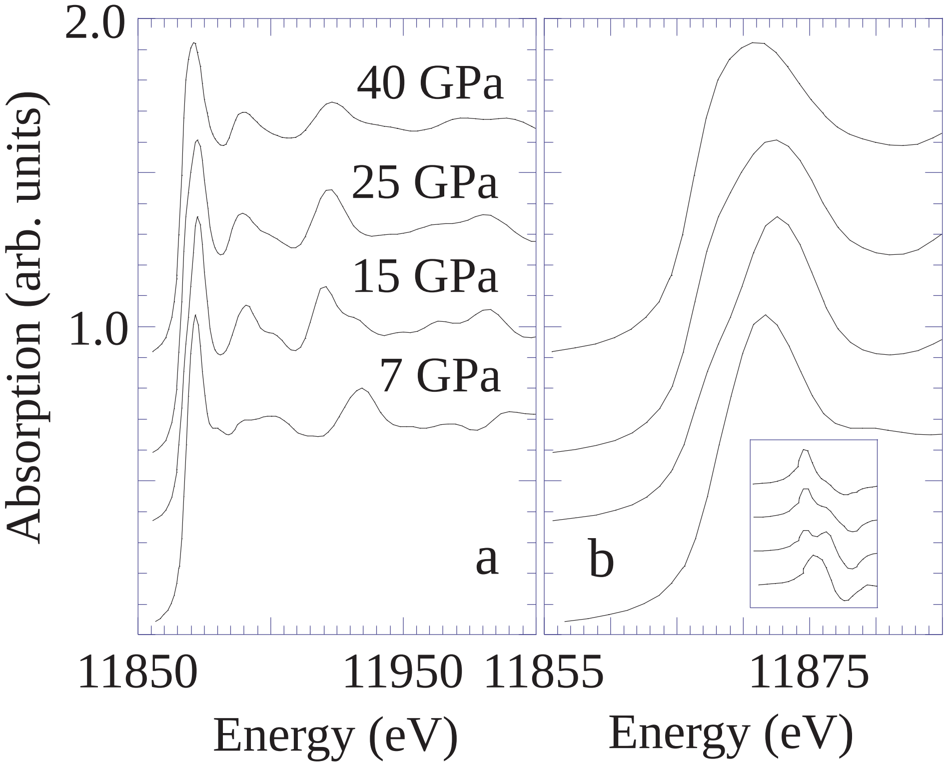

Figure 8.31: a) Simulations that best correspond to the data shown in Figure 8.24: ZB at 7 GPa, short-range chemically-ordered NaCl at 15 GPa, short-range chemically-ordered *Cmcm* at 25 GPa and 50% linear combination of short-range chemically-ordered *Cmcm* and short-range chemically-disordered *Pmma* at 40 GPa. b) Edge region: the inset shows the trend on the derivatives.

The overall good agreement between the calculated (Figure 8.31) and the measured spectra (Figures 8.24 and 8.26) is striking, considering the absence of adjustable parameters in the theory. The major features and their variation with pressure are correctly reproduced: the disappearance of the shoulder at $\sim$ 11.9 keV and the trend on the discontinuity in the first derivative (inset of Figure 8.31) and the evolution towards a broadened and rounded shape of the white line (Figure 8.31). The trends in the evolution of the XAS spectra can therefore be associated to the following structural sequence: ZB → sr-co NaCl → sr-co *Cmcm* → sr-cd *Pmma*.

8.6.5 Conclusions

We have performed a combined XRD and XAS study on one of the most ionic members of the group III-V compounds: InAs. Using the two techniques we demonstrate that InAs does not transform to the CsCl phase after the *Cmcm* phase as previously thought, but to a short-range chemically disordered *Pmma* phase, that persists at least up to 46 GPa. A structure with *Pmma* symmetry has recently been shown to be a direct consequence of a phonon instability of CsCl. Although we cannot exclude the presence, at higher pressures, of a *Pmma*-distorted CsCl-like structure, this finding suggests that the high-simmetry cubic CsCl phase is likely not to occur as a HP phase in InAs. The mechanism responsible for the *Cmcm* → *Pmma* transition is not yet clear, but calculations are underway to suggest what it is. The CsCl phonon instability that leads to *Pmma* is predicted to set in after 135 GPa [12]. However, we must make clear that the observed transition is from the orthorhombic *Cmcm* phase rather than from the cubic CsCl phase, so the much lower transition pressure value is not surprising: other work [182] has shown that phonon softening in distorted phases sets in at much lower pressures than in closely-related high-symmetry phases.

This finding has important implications for the structural systematics of semiconductors: InAs is the first of the III-V semiconductors for which the existence of a structure derived from phonon instability considerations is verified a posteriori, leaving the experimental examination of the remaining systems foreseen to have a similar behaviour, InP, GaP and GaAs, still to be carried out.

8.7 HP and HT XRD study of InAs

The bulk of HP experimental data available on $A^NB^{(8-N)}$ compounds refers to RT measurements. The P-T phase diagram remains therefore largely unexplored. Moreover, temperature can play a major role in reducing kinetic barriers at the onset of phase transitions and uniaxial strain effects caused by non-hydrostatic conditions. We have performed combined HT/HP EDXRD measurements up to 630 K and 30 GPa on InAs. As we reported in paragraph 8.6.2, it seems that NaCl phase for InAs does not exist as a discrete phase at RT and a common feature of independent works seemed to be the rather narrow stability range observed for the NaCl phase. The goal of these measurements was to investigate the role of temperature in the ZB → NaCl phase transition and to explore the structural sequence at higher pressures and temperatures. Our data show that the structural sequence observed at RT is preserved only up to T = 470 K, but not at T ∼ 600 K [16].

8.7.1 Experimental details

EDXRD measurements were carried out at LURE, on the wiggler station DW11 of DCI. The polychromatic X-ray beam was collimated down to 150 μm × 50 μm and the diffraction angle was fixed at $2\theta = 12.4$ deg.. The collimated diffracted beam was detected with a liquid Nitrogen cooled solid state Ge detector. High pressure and temperatures were generated using a resistive heated Chervin membrane DAC [57]. We used standard Drukker diamonds with 400 μm flats. The InAs sample consisted of a fine powder ground to the micron particle size from 99.9999% polycrystalline InAs (Alfa). The PTM used were Silicone oil (T < 500 K) and LiF (T > 500 K). The pressure was measured using the fluorescence emission of ruby [62] and/or $SrB_4O_7:Sm^{2+}$ [73]. EDXRD measurements were performed up to 30 GPa. The temperature of the back side of the diamonds, T_{dia}, was measured using a K-type thermocouple. The sample temperature T is slightly higher than T_{dia}; its value is estimated to be within T_{dia} and the setpoint temperature, $T_{set} = T_{dia} + 20$ K. Throughout the discussion we shall refer to the values of T_{dia}.

8.7.2 Results and discussion

Table 8.1 summarizes the different runs of measurements carried out. The sample was newly charged at each run. The first three runs were carried out at fixed temperature (T_{dia} = 400 K, 470 K and 600 K). The structural sequence observed in Run 1 and Run 2 are identical, with minor differences in phase transition onsets and phase coexistence

Run	Type of run	T_{dia}	P_{max} (GPa)	PTM	$P_{calibration}$
1	Fixed T, Variable P	400	30	Silicone oil	Ruby, $SrB_4O_7:Sm^{2+}$
2	Fixed T, Variable P	470	30	Silicone oil	Ruby, $SrB_4O_7:Sm^{2+}$
3	Fixed T, Variable P	600	17	LiF	LiF, $SrB_4O_7:Sm^{2+}$
4	Variable T, P	630	7	LiF	LiF, $SrB_4O_7:Sm^{2+}$

Table 8.1: Summary of the values of the thermodynamic variables P and T covered during the 4 runs of measurements. Column 5 and 6 report the PTM used and the method for pressure calibration respectively.

regions. The data clearly reproduce the two phase transitions observed at RT. The behaviour of InAs at $T_{dia} \sim 600$ K (Run 3) was found to differ from that at lower temperatures. Due to strong thermal constraints at this temperature, it was not possible to increase the pressure above 17 GPa. The cell also experienced a sudden pressure jump between 10 and 15 GPa, making this pressure region impossible to measure on the upstroke series. While the profiles at $P > 15$ GPa are consistent with the occurrence of a *Cmcm* phase, as observed at lower temperatures, the behaviour at $P < 10$ GPa differs from that observed at lower temperatures (Figure 8.32).

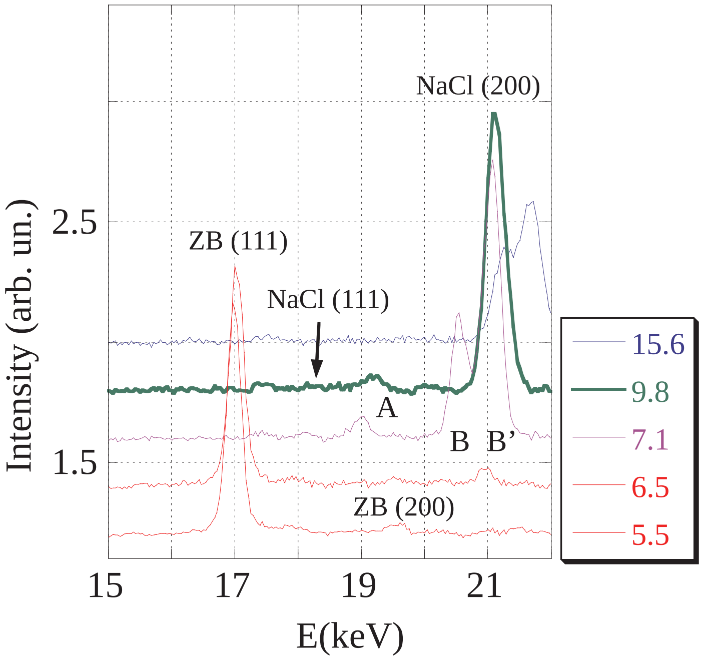

Figure 8.32: Some of the profiles obtained during Run 3. The behaviour at $P < 10$ GPa differs from that observed at lower temperatures: new features A, B and B' appear at $P \sim 7.1$ GPa.

The profile at $P = 7.1$ GPa shows:

i. the disappearance of the ZB (111) reflection at $E \sim 17$ keV,

ii. the appearance of new features: a single peak (A) at $E \sim 19$ keV, and a double peak (B and B') at $E \sim 21$ keV.

The double peak merges into a single peak in the profile at $P = 9.8$ GPa (bold line), where it could be indexed on the NaCl (200) reflection. We have marked the expected

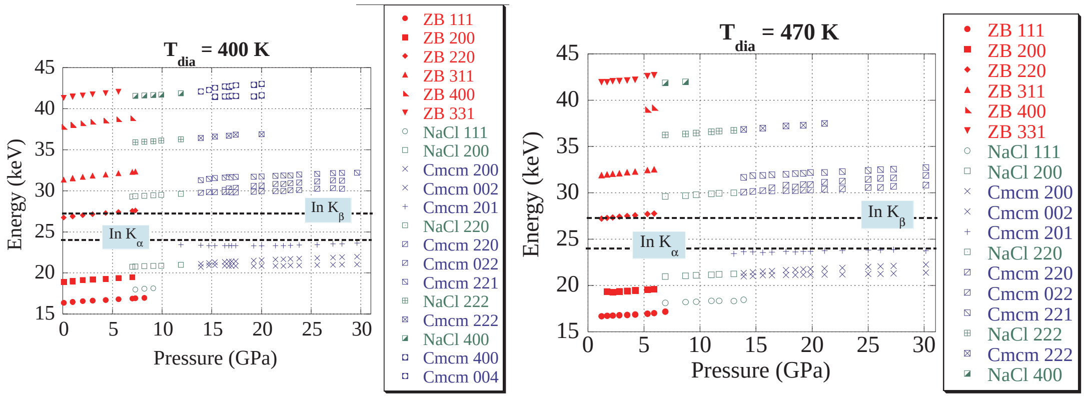

Figure 8.33: Evolution of the energy positions of all the observed peaks for the first two runs: Run 1 (*left panel*), Run 2 (*right panel*). The two run are qualitatively similar, and the structural sequence remains identical to that observed at room temperature.

position of the NaCl (111) reflection at P = 9.8 GPa, which is absent. Peaks at higher energies (at E ∼ 30 keV, ∼ 36 keV and ∼ 42 keV) are also visible on this data, but due to their low intensity it is not possible to evaluate whether they correspond to split peaks (similar to B and B′) or to single peaks indicative of a pure NaCl phase contribution (the NaCl (220), (222) and (400) reflections respectively) in this pressure region.

In Figure 8.33 we illustrate the evolution of the energy positions of all the observed peaks for the first two runs. The behaviour of InAs observed in Run 1 (*left panel*) and Run 2 (*right panel*) is qualitatively similar: with respect to the room temperature data using Silicone oil as pressure transmitting medium, phase coexistence regions and phase transition onsets are reduced, a consequence of the reduced kinetic barrier in similar hydrostatic conditions, but the structural sequence remains identical.

The situation is different for Run 3, as shown in Figure 8.34, where we mark the energy positions of the new features A, B and B’, and the expected position for the NaCl (111) reflection (dashes at E ∼ 18 keV), not observed in the data. In order to further investigate the behaviour of InAs in this temperature and pressure region, we performed a fourth run (Run 4) where pressure and temperature were both varied up to a maximum of T_{dia} = 630 K and P = 7 GPa. Some of the profiles relative to Run 4 are plotted in Figure 8.35. At T_{dia} ∼ 590 K, together with ZB reflections, we clearly observe the onset of features A, B and B′ at P ∼ 5.9 GPa. Their intensity increases with pressure, up to 6.7 GPa as for the data of Run 3, it is difficult to say whether a

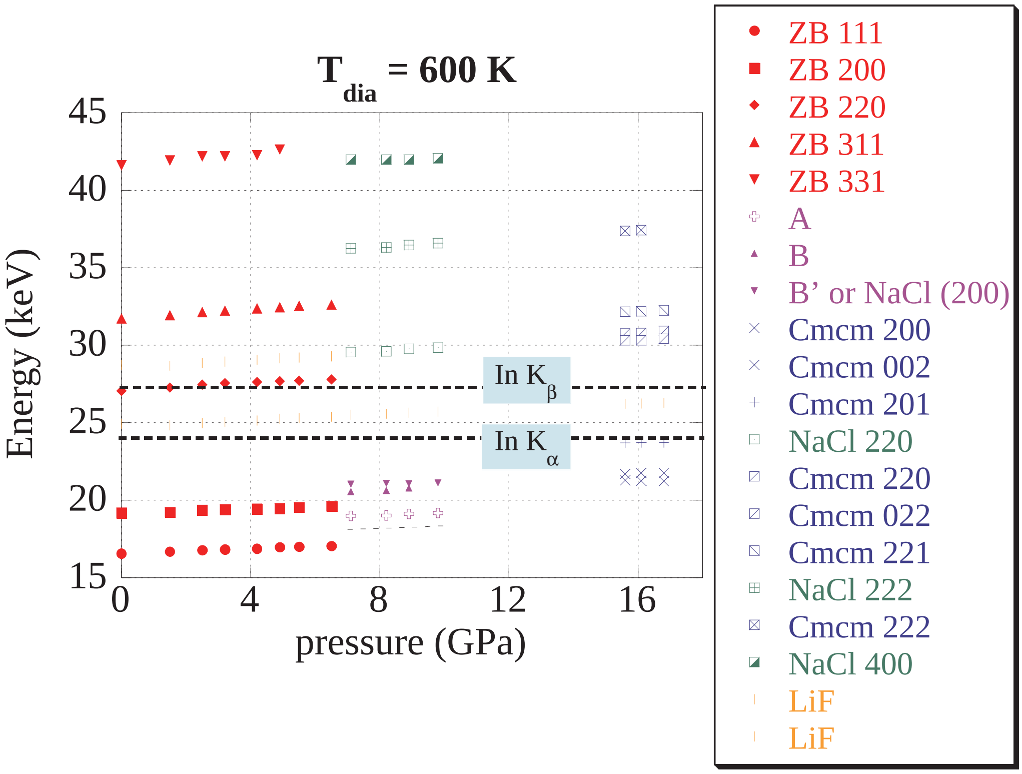

Figure 8.34: Evolution of the energy positions of all the observed peaks for Run 3. The energy positions of the new features A, B and B′ and the expected position for the NaCl (111) reflection (dashes at E ∼ 18 keV) not observed in the data are marked.

contribution of the NaCl phase can be detected in this pressure and temperature region. On temperature and pressure release, all these peaks persist with the same intensity down to about room temperature and $P < 3$ GPa. At this pressure, very wide ZB reflections appear, indicating that the sample (or a large portion of it) has transformed back to its initial symmetry, although the recovered phase is characterized by a large degree of structural disorder. It is not possible to determine, from this data, whether an amorphisation has occurred or whether mechanical stress in the DAC has lead to a strong reduction of the nanoparticle sizes.

To summarize, we show in Figure 8.36 the structural behaviour of InAs in P,T space, as it emerges from the measurements performed in this work and in previous RT experiments. It is not possible, with these measurements alone, to identify the nature of the new phase, if any, observed in InAs at $T_{dia} \sim 590$ K and above. We have recently undertaken a more detailed high pressure ADXRD study in order to be able to perform a complete structural refinement. A preliminary analysis of this data set confirms this behaviour also in the absence of LiF, enabling us to exclude that the new features are a consequence of a reaction with LiF in Runs 3 and 4. The observed effect on InAs is similar in some aspects to that seen at the onset of the cinnabar phase in a number of II-VI binary although we do not infer that we do observe this phase in InAs.

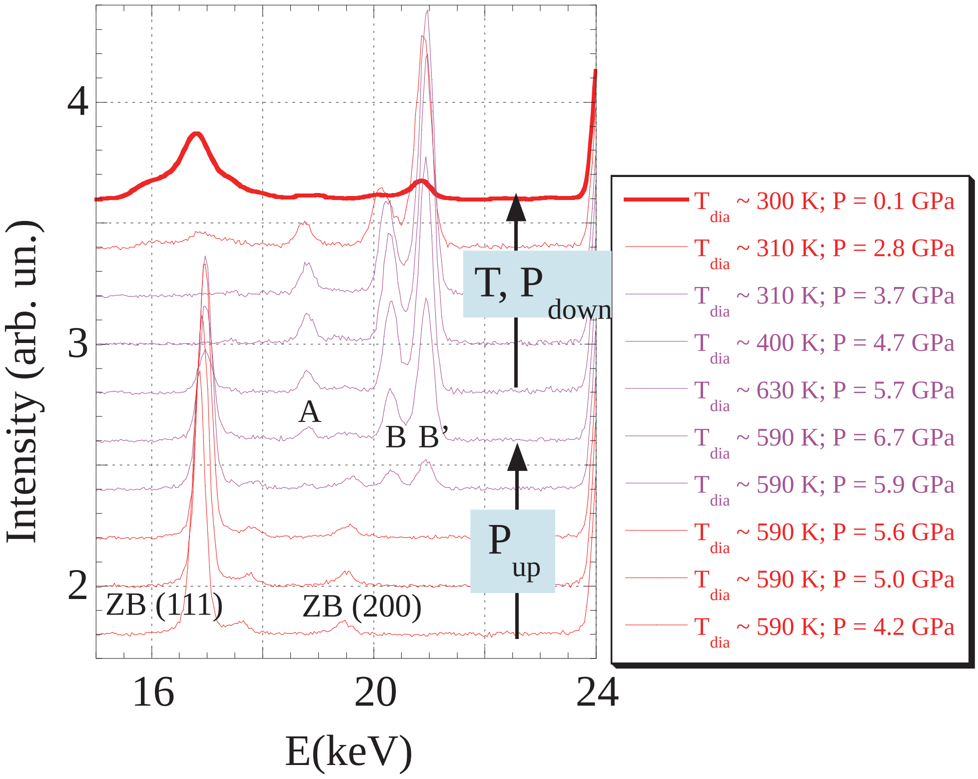

Figure 8.35: Some of the profiles relative to Run 4. At $T_{dia} \sim 590$ K, we clearly observe the onset of features A, B and B′ at $P \sim 5.9$ GPa. On temperature and pressure release, these peaks persist with the same intensity down to about RT and $P < 3$ GPa. At this pressure, very wide ZB reflections appear. At ambient condition (in bold) peaks B and B′, although very weak and large, are still detectable.

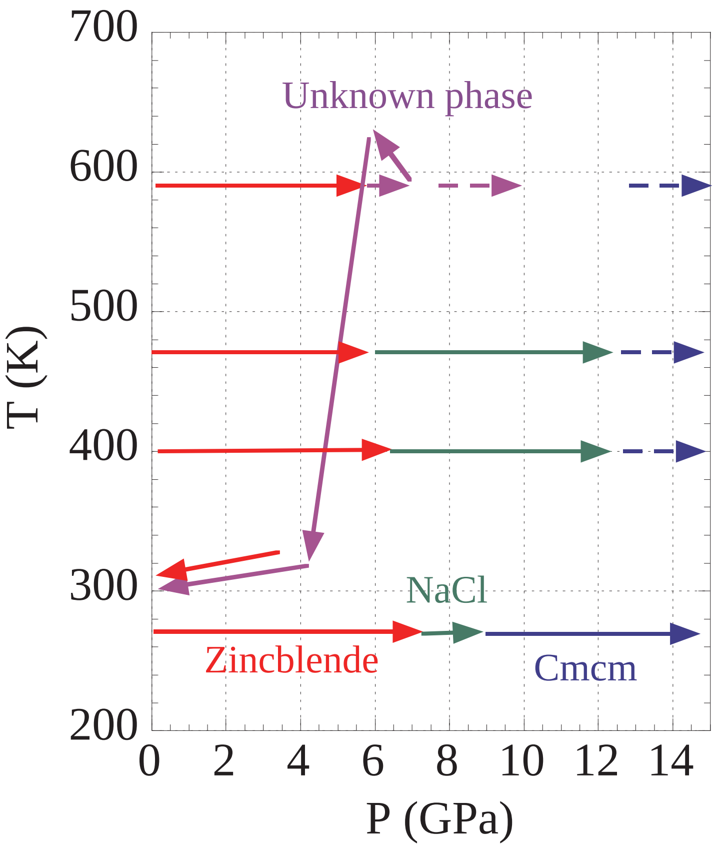

Figure 8.36: Structural behaviour of InAs in P,T space, as it emerges from the measurements performed in this work and in previous room temperature experiments.

8.7.3 Conclusions

We have carried out HP and HT EDXRD measurements on InAs. Our data show that the room temperature structural sequence is not preserved at $T_{dia} \sim 600$ K. At this temperature and at ~ 6 GPa we observe the appearance of an as yet unidentified phase, that persists down to ambient conditions upon release of pressure and cooling.

Conclusions

This Thesis concerns the development of two different applications of energy-dispersive XAS at the ESRF: TR studies pushed to the microsecond time resolution and HP studies at the limit of the Megabar pressures. The work has been developed in two distinct parts and, keeping in mind its strong experimental character, the underlying theme has been the exploitation of the capabilities of an X-ray absorption spectrometer in dispersive geometry on a third generation synchrotron source.

We have improved many technical aspects of beamline operation, from the synchronization technique, to the characterization of the behaviour of scintillator screens for TR studies. We have extended the possibilities for HP studies, from feasibility tests for XAS below 8 keV to the implementation of a system for combined absorption and diffraction measurements. In addition, we have undertaken the commissioning of several instruments, which are now part of the standard equipment of beamline ID24, such as the UV-VIS spectrometer, the nanosecond Nd:YAG laser, the liquid Helium cryostat, and also the heated DAC. All the above has been part of my work of the last three years, in collaboration with other staff of beamline ID24 and ESRF. This instrumental work has given us the opportunity to face several scientific challenges leading us, sometimes, to address issues that had not been taken into consideration at the beginning. These have often prompted further investigations, leaving in some cases open points that we could not answer in this Thesis, but that could offer occasion for future work.

For TR studies, to push the technique to the microsecond time resolution, we have chosen to study the $Pt_2(P_2O_5H_2)_4{}^{4-}$ system. The aim was to determine the structure of the triplet excited state of this complex following a laser excitation. This sample was, based on previous results, a good candidate to test a technique in principle capable of determining the structure of matter in its metastable excited state, which is of crucial importance for many chemical and biological processes. The result of our experiment was “negative”, in the sense that we were not able to detect any difference between the structure of the ground state and the structure of the excited state. This, on one hand, has been frustrating because it has, in fact, prevented us to establish the microsecond TR XAFS on ID24. On the other hand, it has pushed us to search for the reasons that led to this result. So, other tests have been performed on $\mathrm{Pt_2(P_2O_5H_2)_4}^{4-}$ and in particular we have examined the effect of the X-ray beam on the sample. We have found, using a UV-VIS spectrometer, that X-rays induce the transition to the triplet excited state to which the structural modifications are linked. This means that our probe behaves as a pump itself interfering with the sample in a way to prevent us from detecting any difference signal. We also found that this effect becomes more important with the increase of the intensity of the beam. We have simulated the XAFS signal of $\mathrm{Pt_2(P_2O_5H_2)_4}^{4-}$ in its ground and in its triplet excited state and have verified that the $k\chi_{exp}(k)$ of the absorption spectrum recorded on ID24 presents the typical features of $k\chi_{m(x)}(k)$ defined as a linear combination of ground and excited state XAFS signals. These experimental evidences explain our negative results, but are embarrassing since one of the experimental requirements for TR experiments below the millisecond time resolution is the high flux in order to be able to collect a complete dataset in a reasonable time having a good statistics. This explanation also reopens the troublesome question of “radiation damage”, which is a known problem difficult to overcome especially in the case of biological samples [183]. To summarize, we demonstrated that the sample of choice was not a good candidate to pinpoint our microsecond XAFS technique and other samples have to be looked for. However, after this work the investigation of the structure of the triplet excited state of $\mathrm{Pt_2(P_2O_5H_2)_4}^{4-}$ remains an intriguing problem. A possible way to address this question using XAS is by performing a pump/probe experiment on a standard EXAFS beamline with a reduced flux, for example, synchronizing the laser to the X-ray bursts.

At the beginning of this Thesis, the experimental conditions on beamline ID24 were such that the characteristics of the energy dispersive XAS spectrometer could be exploited for HP studies using DACs. The suitability of energy dispersive XAFS spectrometers for such kind of studies had already been demonstrated by the large number of works performed at the dispersive EXAFS beamline D11 at LURE. The improved beam stability, thanks to the implementation of a local feedback on the ID24 straight section, has led to an improvement of the quality of the data especially for non-homogeneous samples such as powders, besides being essential in the case of small samples. The reduced vertical spot size has led to an important increase in flux. The increased flux has allowed us to perform XAS measurements under HP conditions at absorption edges of energies where the absorption of the diamonds is important, such as the Fe K-edge. The vertical focusing has allowed us to achieve spot sizes of the order of $20 \times 20\ \mu\text{m}^2$ allowing to reach pressures of the order of Megabar. The combination of the two have allowed us to successfully perform a HP experiment at Fe K-edge up to one Megabar. This achievement opens important opportunities in the fields of geophysics, where the knowledge of the oxidation states and structure of transition metal oxides at Megabar pressures is of fundamental importance.

In the framework of the structural studies of matter at HP, XRD is by far the most common X-ray technique. Furthermore, it is well known that XAS and XRD are complementary for the structural investigation. Recent studies have demonstrated that the combination of the two techniques is essential to fully describe new HP phases and have prompted us to implement a system for combining absorption and diffraction on ID24. Therefore, in addition to the XAS data acquisition routinely performed on ID24, we equipped the beamline with a MAR345 image plate to record diffraction patterns. Using our newly commissioned heated DAC, we performed combined XAS and XRD at HP/HT on the model system $ZnCl_2$. Even in this case, the model system chosen gave us hints for further investigation on its HP phase, both performing diffraction measurements at a dedicated beamline, and extracting more information from our absorption data by performing structural fitting (constrained by XRD results), hopefully soon possible, of the XANES region.

The most extensive scientific part of this Thesis concerns the study of InAs under pressure. This research falls within the framework of the study of the structural properties of semiconductors at HP, one of the most fertile topics for HP research since the first works of Jamieson in the early 60s. The combination of X-ray absorption and diffraction proved again to be essential to fully describe the new phase. Measurements using the two techniques on InAs revealed the presence of a HP short-range chemically disordered *Pmma* structure and showed no evidence of the CsCl phase, in agreement with recent phonon dynamics calculations. This finding demonstrates the power of recent theoretical calculations that are able not only to identify instabilities in "statically" stable phases, but also able to predict the occurrence of alternative structures. The present work concerns the first experimental verification of the inclusion of phonon instability effects in the theoretical description of the HP behaviour in III-V semiconductors. A first combined study at HT and HP on InAs has also been carried out using EDXRD to investigate the role of temperature in the zincblende → NaCl transition. The data have shown that the room temperature structural sequence is not preserved at 600 K where we observed the appearance of an as yet unidentified phase. Recent measurements at HT and HP, still to be analyzed, have been performed using ADXRD. We also have planned to record HT-HP EXAFS data using our combined XRD and XAS setup and our newly commissioned heated DAC. The work already performed on InAs in addition to that still to be carried out will give us a new perspective on the behaviour of this compound in the unexplored (P, T) space. Experimental examination of the remaining systems foreseen to have a similar behaviour, such as GaP, has already started.

At the end of this Thesis work we can affirm that ID24 is an unique instrument in the world that offers the opportunity to perform HP studies up to Megabar pressures using XAS. This is possible at absorption edges unaccessible until very recently, and also in combination with HT in order to explore new regions of (P, T) space. Furthermore, the combination of XRD as well as theoretical advances in the description of the near edge region with soon the possibility to perform structural fitting of the XANES region, will lead to a higher exploitation of the XAS data, allowing to properly address difficult issues related to the determination of the structure of matter at HP.

Appendix A

Principle of dispersive optics and beamline ID24

A.1 Dispersive optics

X-ray absorption spectroscopy using energy dispersive optics has been widely exploited to study dynamical processes as well as very small samples in restrictive environments, thanks to the parallel data collection and to the small and stable focal spot respectively. Moreover, the mechanical stability of the optics during acquisition drastically reduces the sources of noise, thereby opening the way to the study of very small signals, such as those encountered in X-ray Magnetic Circular Dichroism [184].

The geometrical arrangement of the energy dispersive optics is given in Figure A.1. A quasi-parallel and polychromatic beam, supplied by a SR source, is energy-dispersed and focused by an elliptically curved crystal. Because the incident X-rays strike the crystal at slightly different angles along its length, the bent crystal acts as a polychromator diffracting a different energy at each point. This energy-dispersed beam converges to a focus at the sample position. The beam, transmitted through the sample position, then diverges towards a PSD. The position of the beam, incident in the detector, can be directly correlated to energy. By measuring the spatial X-ray intensity distribution in the presence (I_1) and absence (I_0) of the sample, a familiar X-ray absorption spectrum can be consequently be obtained by taking the logarithm of the ratio of I_0 data and I_1 data.

Considering a cylindrically bent crystal, which is a good approximation for an ellipse, the source to crystal distance p is large compared to the radius of curvature R of the crystal. R is related to the source to crystal distance p, crystal to focal point q, and Bragg angle θ for the central X-ray beam, through the equation of cylindrical optics:

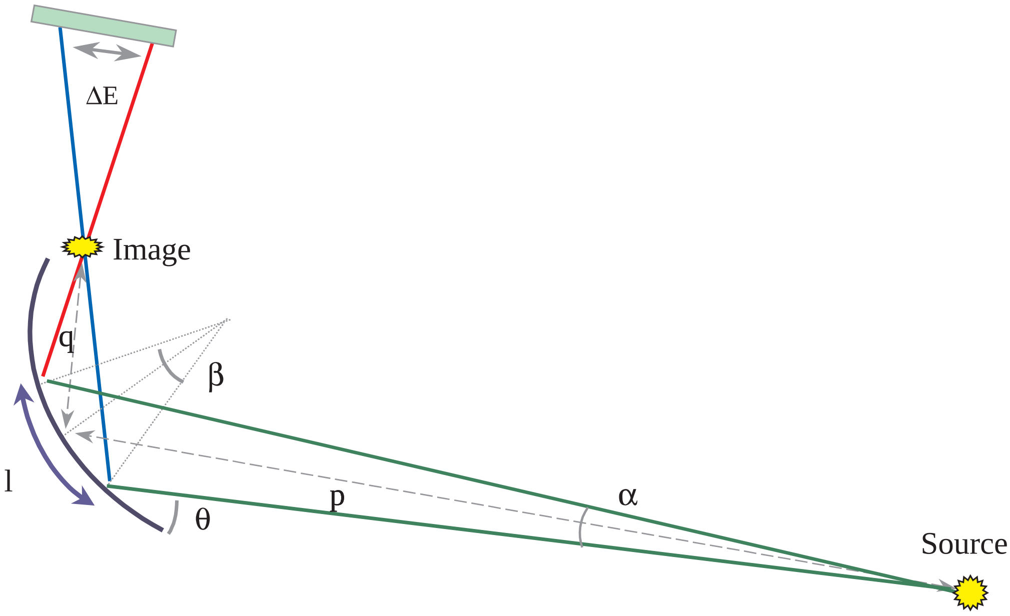

Figure A.1: Geometrical arrangement of the energy dispersive X-ray absorption spectrometer.

$$\frac{1}{q}+\frac{1}{p}=\frac{2}{R\sin\theta_B}. \tag{A.1}$$

The angular dispersion $\Delta\theta$ is:

$$\Delta\theta=\beta-\alpha=\frac{l}{R}-\frac{l\sin\theta_B}{p}, \tag{A.2}$$

where l is the illuminated length of the crystal. The diffracted energy range is given by

$$\Delta E=E_H-E_L=E_0\cot\theta\Delta\theta=E_0\cot\theta\left(\frac{l}{R}-\frac{l\sin\theta_B}{p}\right), \tag{A.3}$$

where E_H and E_L are the highest and the lowest energies respectively, E_0 is the energy of the central beam. The energy resolution δE is obtained from the derivative of Bragg's law:

$$\delta E=E_0\cot\theta\delta\theta, \tag{A.4}$$

where $\delta\theta$ is the overall angular resolution. δE is a function of several parameters, among which:

i. source size;

ii. intrinsic energy resolution of polychromator (Darwin width);

iii. distance between sample and PSD;

iv. PSD pixel size/spatial resolution;

v. X-ray penetration depth in polychromator crystal.

A.2 Beamline ID24

Beamline ID24 is the ESRF XAS beamline with parallel detection of the whole spectrum made possible by energy dispersive highly focusing X-ray optics [6, 7]. This beamline is the first of its kind to be installed on a third generation SR source.

The radiation source consists of two low K tapered undulators in a high β section of the ring. The undulators are 1.6 m long with 42 periods of 40 mm per period. A magnetic field of 0.37 T at 20.3 mm minimum gap leads to a radiated power of 1 kW at 150 mA stored current. In the center of the high horizontal β straight sections, at the source point, the rms (root mean square) beam sizes is σ_x = 402 μm and σ_z = 7.9 μm and divergence is σ'_x = 10.7 μrad and σ'_z= 3.2 μrad (http://www.esrf.fr/Accelerators/Performance). The energy range of operation is 5 – 27 keV. The spectral characteristics required for experiments at selected absorption edges are obtained by gap tuning and tapering of the undulators. The central cone of the undulators is selected by the primary slits with a typical aperture of 1.5 mm (H) × 1.0 mm (V). The choice of an undulator is unusual taking into account that all other operating dispersive XAS beamlines worldwide are installed on bending magnet or wiggler sources. The latter sources naturally yield the large horizontal divergence (typically a few mrads) necessary to obtain, with reasonable radii of curvature of the polychromator crystal, an energy dispersion making it possible to cover a whole XANES or EXAFS spectrum. However, the choice of an undulator has clear advantages [5]:

i. the possibility to match the bandwidth of emission of the undulators and the acceptance of the polychromator by optimizing the gap, the taper and the radius of curvature of the polychromator crystal. This results in a reduction of heat load on the optics;

ii. a substantial reduction of unwanted harmonics;

iii. higher brightness and lower vertical divergence; and

iv. low monochromatic divergences (horizontal and vertical), which allow the optimal exploitation of the properties of quarter wave plates to tune the helicity of incoming photons.

Figure A.2 shows the present optical scheme, which is an upgraded version of the original one [7]. The coupling optics are of Kirkpatrick-Baez type. The two Kirkpatrick-Baez mirrors reflect the beam at a fixed grazing angle of 3 mrad and ensure efficient harmonic rejection in the whole energy range of operation. Both mirrors are manifactured of a 0.3 mm thin layer of SiC deposited on high density graphite. A slope error of 5 μrad rms and a micro-roughness of 5 Å rms have been measured. They are installed under vacuum, a typical base pressure of 2×10^{-8} mbar is achieved with beam. The mirrors are coated with two 20 mm wide strips of Rh and Pt. At a fixed incident angle of 3 mrad, the critical energies for total reflection are 22 keV and 28 keV for Rh and Pt respectively. The central 16 mm wide strip is not coated, which yields a critical energy of 12 keV. The first mirror, placed at 30 m from the source, is in a quasi 1:1 configuration and

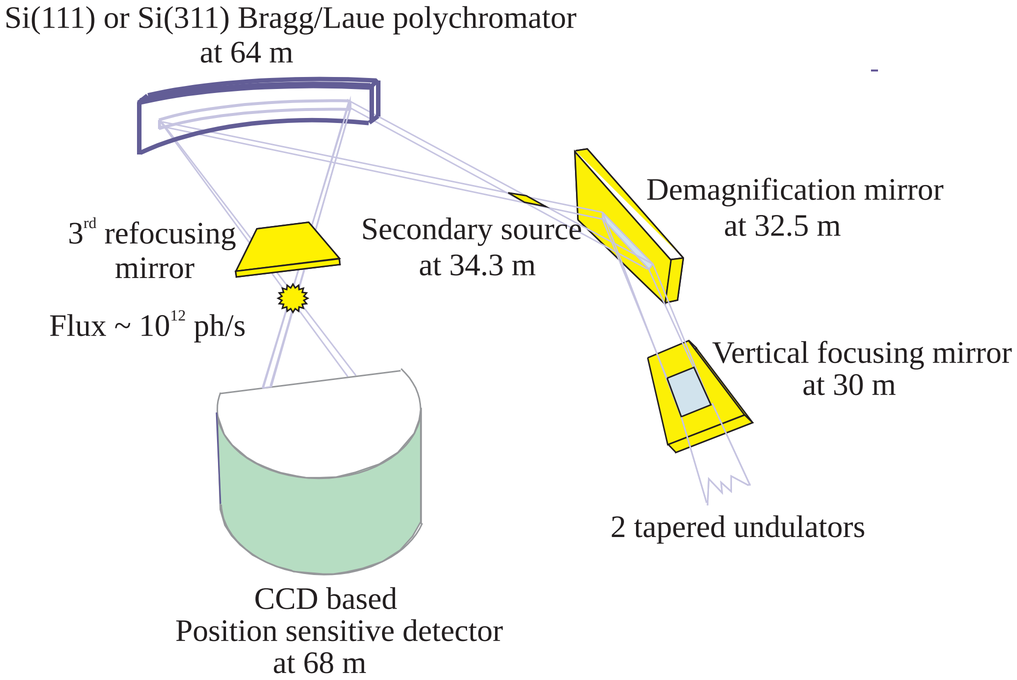

Figure A.2: Present optical layout of beamline ID24. The polychromator is coupled to two undulators through a Kirkpatrick-Baez optical system. The third refocusing mirror was added to the original configuration in 2000.

vertically focuses the beam on the detector through a pneumatic bender mechanism. The radius of curvature is $\sim$ 11 km. Due to the quality of the reflecting surface and to the large mirror-sample distance (36 m), the vertical dimensions of the focal spot are about an order of magnitude larger than the source size ($\sim$ 300 μm FWHM). For experiments requiring a small focal spot, such as HP experiments using DACs, a third mirror to refocus the beam in the vertical direction at the sample position is added to the optical configuration, and is described in section 7.1. The horizontal divergence necessary to obtain the requested energy bandwidth (ΔE) after diffraction from the polychromator is produced by the second mirror. Placed at 32.5 m from the source, this strongly focusing mirror creates a horizontally-demagnified image of the source that becomes the effective source S$'$ for the polychromator crystal, 1.8 m downstream (34.3 m from the source), and leads to a horizontal divergence of 1 mrad. The present mirror has a cylindrical shape, leading to a strongly spherically aberrated effective source. An elliptical mirror will soon substitute it. This improvement is expected to lead to an aberration free effective source, and therefore to a smaller horizontal spot size on the focal point.

The spectrometer consists of a Θ - 2Θ goniometer with the monochromator on the Θ axis and an optical bench oriented at 2Θ with the sample and the position sensitive detector on it. The polychromator vessel is located 64 m from the undulator source. The distance to the effective source S$'$ amounts to 29.7 m. The polychromator consists in a curved Si crystal in a Bragg [185] or Laue [186] geometry. The beam is focused at $\sim$ 1.5 m from the polychromator crystal at the sample position leading to a horizontal divergence of $\sim$ 20 mrad. Si(111) and Si(311) crystals are used to match the energy resolution/energy bandwidth requirements for the specific applications. In the Bragg geometry, X-ray penetration depth effects at high energies introduce extended asymmetric tails in the reflectivity curve and in the focal spot distribution, which limit the use of this geometry to the energy range $\sim$ 5-13 keV. Above these energies, a curved asymmetric ($\alpha = -6°$) Laue crystal is used. Recently, the focalization properties of the Bragg crystal have been improved by refining the profiled shape of the crystal [187]. FWHM values are now generally below 20 μm at all energies covered by the Bragg crystal, but the presence of the asymmetric tail limits the usefulness of the Bragg geometry at very HP ($P \geq 50$ GPa) in the high energy range ($E > 10$ keV). Figure A.3 illustrates typical horizontal profiles of the focal spot obtained using the Bragg crystal at the Fe K-edge (7.112 keV) and at the Ga K-edge (10.367 keV). The $\alpha = -6°$ Laue geometry yields symmetric profiles at all energies, but characterized by larger FWHM

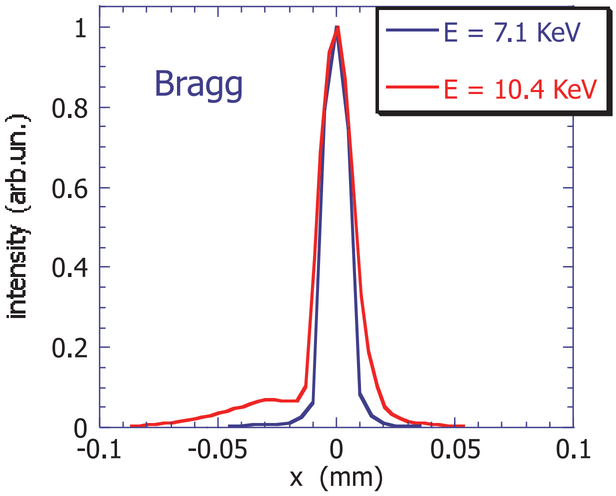

Figure A.3: Horizontal profiles of the focal spot obtained using the Bragg crystal at the Fe K-edge (7.112 keV) and at the Ga K-edge (10.367 keV). An important asymmetric tail arising from penetration depth effects is visible at high energies. This tail precludes the use of the Bragg geometry for very HP applications (P $\geq$ 50 GPa) for high energies (E $>$ 10 keV).

values ($\sim$ 80 - 100 μm). In order to extend the energy range for very HP applications, the possibility of exploiting the focusing properties of curved asymmetric Laue crystals [188] to improve the horizontal distribution of the focal spot at energies above $\sim$ 10 - 11 keV is being investigated [187].

The polychromatic fan of radiation is intercepted by a position sensitive detector [24] placed at $\sim$ 68 m from the source, that transforms the energy-direction correlation into an energy-position correlation, (a more complete description of the detector of ID24 is given in section 2.2) and allows to acquire in parallel all the data points in the energy range ΔE diffracted by the polychromator. ΔE is directly proportional to the footprint of the beam on the polychromator crystal and to the cotangent of the Bragg angle [3], as seen in the previous paragraph. The latter factor severely limits ΔE at low energies. Typical values for ΔE/E range between 5% to 15% at low and high energies respectively.

Appendix B

Local feedback on ID24 straight section

The ESRF storage ring generates X-rays from insertion devices installed on 5 m long straight sections. In the center of the high horizontal β straight sections, at the source point, the rms (root mean square) beam sizes is $\sigma_x = 402$ μm and $\sigma_z = 7.9$ μm and divergence is $\sigma'_x = 10.7$ μrad and $\sigma'_z = 3.2$ μrad. The parasitic motion of the beam due to slow drifts or high frequency vibrations of the support girders of the quadrupoles must be kept at low enough values to avoid spoiling this emittance figure. Two kinds of motions are observed: very slow drifts and vibrations. The spectrum of these vibrations is shown on Figure B.1. The amplitude of these vibrations at the ends of the straight sections

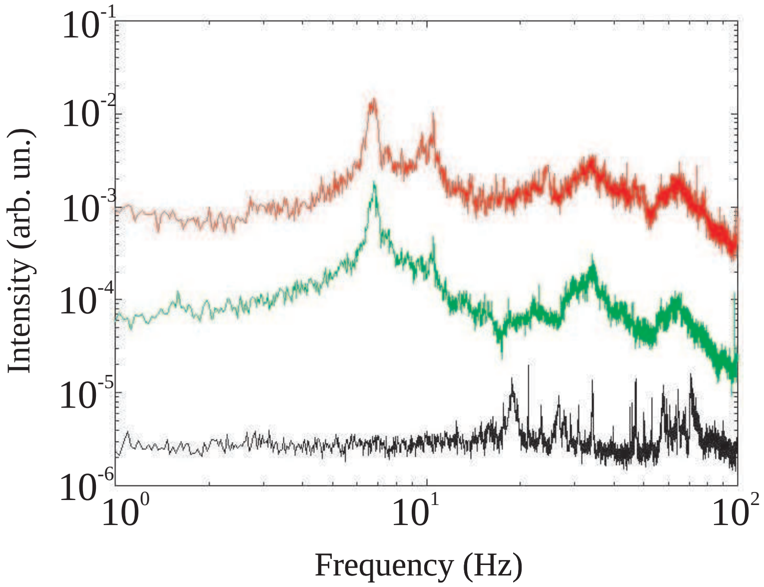

Figure B.1: Frequency spectra of the motion of: the X-ray beam on the sample (*red line*), the electron beam at the source (*green line*), the first mirror on ID24 (*black line*).

is 10 μm rms horizontally and 2 μm rms vertically. The slow drifts are corrected every 30 seconds using measurements made over the whole machine by 224 BPMs of a closed orbit measurement system. Fast correction systems have also been implemented to damp the vibrations in the 0.1 to 100 Hz frequency range, in the vertical and horizontal plane. Since the amplitude of the fast orbit distortion compared to the natural beam size was larger in the vertical plane than in the horizontal plane, it was assumed that the vertical motion was the most detrimental to the machine performance and a vertical correction system [189] was initially installed. The operation of this system resulted in a reduction by a factor of 2 of the amplitude of the fast vertical orbit distortion. This improvement was measured on the machine as well as on beamlines with a high speed intensity monitoring capability like ID24 and ID26. However, it soon became clear that, due to the specificity of their horizontal optics, some beamlines were far more sensitive to the horizontal electron beam motion. For this reason, fast horizontal orbit local correction systems were then also implemented.

The extremely small source size and the length of beamline ID24 introduce a very high sensitivity to electron beam instabilities [190]. This high sensitivity arises from the fact that, since the spectra are obtained from two-dimensional images, they are affected from image distortions due to phase contrast phenomena (or “speckle”) associated with imperfections in the optics and in the sample, and which appear as irregular fringes on the image. The effect of electron beam instabilities is amplified by such spatial modulation and becomes dramatic in the dispersive geometry where the incoming and the transmitted beam are not measured simultaneously. Improvements in the signal to noise ratio have been obtained by using an alternative data acquisition method based on a step by step energy scanning technique [191]. This method however, conserves only part of the advantages of dispersive optics, namely those related to the size and stability of the focal spot.

Since the beginning of operation (1996), beam instabilities have strongly limited the performance of ID24. Typical values for the intensity fluctuations [I(t)-I(0)]/I(0) ranged around 5%-10% (Figure B.2). Such levels of non-statistical noise are not acceptable in general, and in particular on an XAS beamline were the quantity to be measured is a 1 to 10% modulation of the absorption coefficient, requiring a signal to noise ratio well beyond 10^3. To address these problems, the first step consisted in performing a detailed analysis of the amplitudes and frequencies of beam instabilities. Towards the end of 1997 a detailed investigation of the origin of such instabilities started. Vibration frequency spectra were measured on all optical elements, and compared to those measured on the X-ray beam at the sample and on the electron beam at the source (Figure B.1).

Figure B.3 illustrates (on the left) the setup used to measure the beam horizontal movements on the sample: two fast PIN photodiodes (A and B) were positioned just in front of the focal spot, and the current difference I_A - I_B was recorded as a function of time. Panel **a** shows that the beam performs large oscillations with a dominant frequency of a few Hz. The Fourier transform of the oscillations shown in Figure B.3a yields the frequency spectrum shown in Figure B.1 (top curve). The frequency spectrum of the motion of the electron beam is also shown (middle curve). The bottom curve is obtained from the motion of the first mirror of ID24, and is representative of the contribution from the optics of the beamline. From Figure B.1 it appears evident that the main source of the instabilities observed on the sample position is the electron beam itself, and not the optics along the beamline. The amplitude of the effect on the horizontal plane turned out to be much stronger than that on the vertical plane.

The layout of the local feedback is shown in Figure B.4: electron beam positions are measured using capacitive electrodes installed at both ends of the straight section. A closed bump cancelling any position deviation at the BPM locations, and leaving the orbit unchanged outside the bump, is then applied using four corrector magnets. The position measurement and correction rate is 4.4 kHz and the feedback bandwidth is 100 Hz. The operation of the local horizontal feedback started in December 1998 and its effect was immediately evident: the initial electron beam motion observed at the BPM locations was reduced from 7 μm rms down to 1 μm rms by the feedback. Its effect on the frequency spectra measured on the sample position is shown in Figure B.5. The strongest damping is obtained below 10 Hz: an amplitude reduction of up to 30 dB was measured for the peak component at around 6-7 Hz (see also Figure B.3b). A comparable effect was also measured on the CCD detector for the ratio [I(t)-I(0)]/I(0) (Figure B.2b).

The installation of the local horizontal feedback on ID24 has improved in a remarkable way the stability of the beam on the sample. Besides the dramatic improvement in the quality and reliability of the data (in particular for the time-resolved experiments), this development opened the possibility to perform new experiments which take advantage of the high stability of the dispersive XAS scheme. Following the success of the implementation of the horizontal feedback on ID24, the same system was implemented on two other ESRF beamlines: ID14 (Protein Crystallography) and ID21 (X-ray Microscopy) with similar beneficial effects.

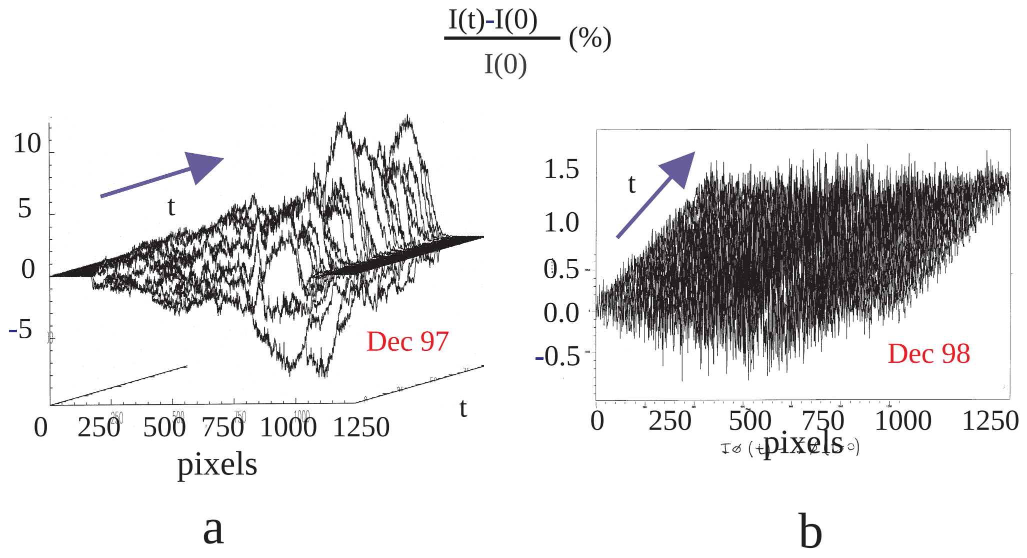

Figure B.2: Relative intensity variations [I(t)-I(0)]/I(0) measured on the CCD detector as a function of time: a) before and b) after installation of the local feedback.

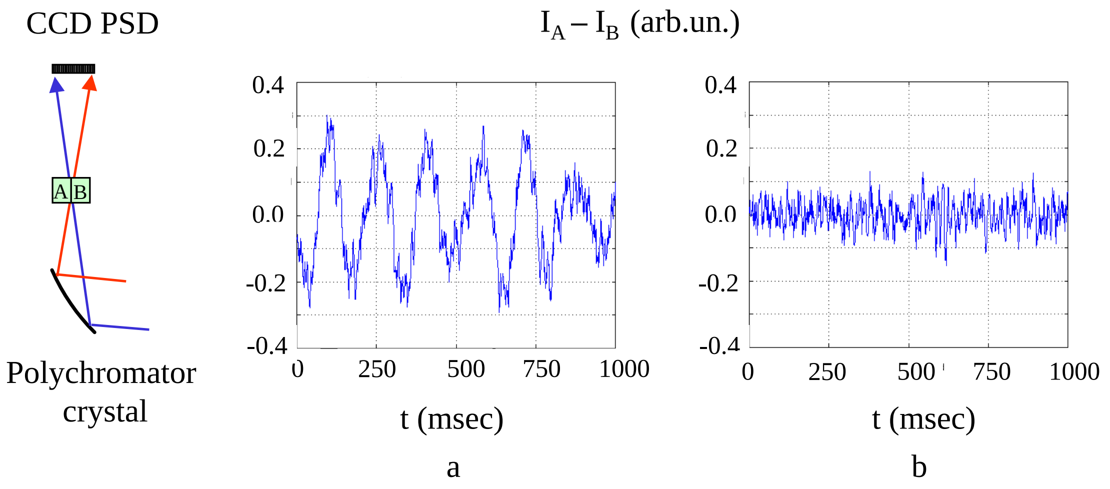

Figure B.3: Time evolution of the current difference I_A - I_B from fast PIN photodiodes A and B positioned just in front of the sample, as shown on the left of the figure. a) before and b) after activation of the local horizontal feedback.

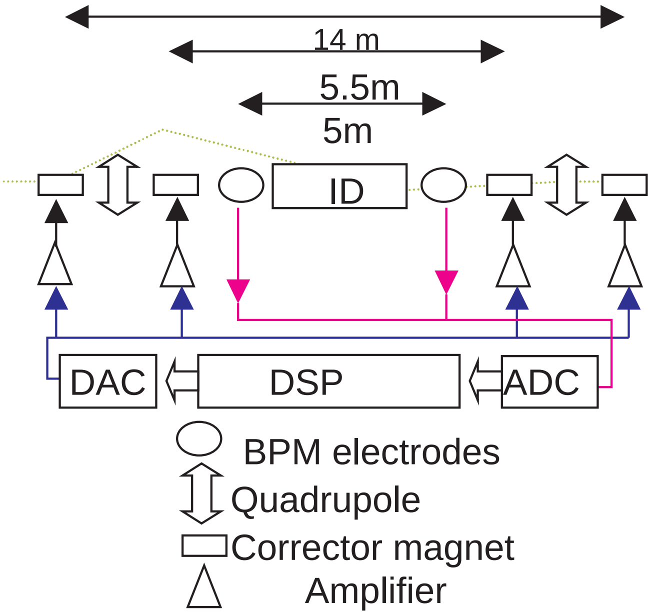

Figure B.4: Layout of the local feedback system.

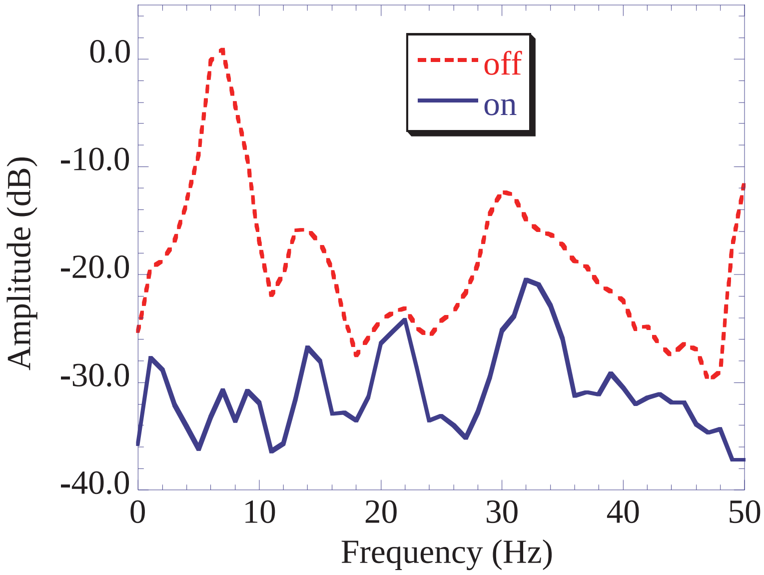

Figure B.5: Frequency spectra of the beam oscillations measured in front of the sample: without (*dotted line*) and with (*continuous line*) activation of the local horizontal feedback.

Bibliography

[1] Y. Cauchois, Conferences-Rapports sur les recherches récentes en physique **5**, (CNRS, 1948).

[2] T. Matsushita and R. P. Phizakerley, Jpn. J. Appl. Phys. **20**, 2223 (1981).

[3] R. P. Phizackerley, Z. U. Rek, G. B. Stephenson, S. D. Conradson, K. O. Hodgson, T. Matsushita, and H. Oyanagi, J. Appl. Cryst. **16**, 220 (1983).

[4] J. P. Itié, F. Baudelet, E. Dartyge, A. Fontaine, H. Tolentino, and A. San Miguel, High Press. Res. **8**, 697 (1992).

[5] A. Fontaine and J. Goulon, ESRF Internal Report on Source Specifications for BL8AF-JG/XAS/ESRF/02-91 (1991).

[6] M. Hagelstein, A. Fontaine, and J. Goulon, Jpn. J. Appl. Phys. **32**, 240 (1993).

[7] M. Hagelstein, A. San Miguel, A. Fontaine, and J. Goulon, J. Phys. IV, Colloque C2 **7**, C2 303 (1997).

[8] D. T. Thiel, P. Līviņš, E. A. Stern, and A. Lewis, Nature (London) **362**, 40 (1993).

[9] J. C. Phillips, in *Bond and Bands in Semiconductors*, edited by A. M. Alper and A. S. Nowic (Academic Press, New York and London, 1973).

[10] R. J. Nelmes and M. I. McMahon, in *Semiconductors and Semimetals* (Academic Press, London, 1998), Vol. 54, Chap. 3.

[11] V. Ozoliņš and A. Zunger, Phys. Rev. Lett. **82**, 767 (1999).

[12] K. Kim, V. Ozoliņš, and A. Zunger, Phys. Rev. B **60**, 8449 (1999).

[13] S. Pascarelli, G. Aquilanti, W. A. Crichton, T. Le Bihan, S. De Panfilis, E. Fabiani M. Mezouar, J. P. Itié, and A. Polian, High Press. Res. **222**, 331 (2002).

[14] G. Aquilanti, W. A. Crichton, T. Le Bihan, and S. Pascarelli, Nucl. Instrum. Methods B **200**, 90 (2003).

[15] S. Pascarelli, G. Aquilanti, W. A. Crichton, T. Le Bihan, M. Mezouar, S. De Panfilis, J. P. Itié, and A. Polian, Europhys. Letters **61**, 554 (2003).

[16] S. Pascarelli, G. Aquilanti, P. Munsch, and J. P. Itié, Nucl. Instrum. Methods B **200**, 439 (2003).

[17] V. Brückner, K.-H. Feller, and U.-W. Grummt, *Applications of Time-Resolved Optical Spectroscopy* (Elsevier, Amsterdam–Oxford–New York–Tokyo, 1990).

[18] D. M. Mills, A. Lewis, A. Harootunian, J. Huang, and B. Smith, Science **223**, 811 (1984).

[19] L. X. Chen, M. K. Bowman, Z. Wang, P. A. Montano, and J. R. Norris, J. Phys. Chem. **98**, 9457 (1994).

[20] L. X. Chen, Z. Wang, J. K. Burdett, P. A. Montano, and J. R. Norris, J. Phys. Chem. **99**, 7958 (1995).

[21] E. M. Scheuring, W. Clavin, M. D. Wirt, L. M. Miller, R. F. Fischetti, Y. Lu, N. Mahoney, A. Xie, J. Wu, and M. R. Chance, J. Phys. Chem. **100**, 3344 (1996).

[22] L. X. Chen, P. L. Lee, D. Gosztola, W. A. Svec, P. A. Montano, and M. R. Wasielewski, J. Phys. Chem. B **103**, 3270 (1999).

[23] L. X. Chen, W. J. H. Jäger, G. Jennings, D. J. Gosztola, A. Munkholm, and J. P. Hessler, Science **292**, 262 (2001).

[24] M. Koch, M. Hagelstein, A. San Miguel, A. Fontaine, and T. Ressler, Proc. SPIE **2416**, 85 (1996).

[25] R. P. Sperline, M. K. Dickson, and D. M. Roundhill, J. Chem. Soc., Chem. Comm. 62 (1977).

[26] M. A. Filomena Dos Remedios Pinto, P. J. Sadler, S. Neidle, M. R. Sanderson, A. Subbiah, and R. Kuroda, J. Chem. Soc., Chem. Comm. 13 (1980).

[27] W. A. Fordyce, J. G. Brummer, and G. A. Crosby, J. Am. Chem. Soc. **103**, 7061 (1981).

[28] C. M. Che, L. G. Butler, and H. B. Gray, J. Am. Chem. Soc. **103**, 7796 (1981).

[29] S. F. Rice and H. B. Gray, J. Am. Chem. Soc. **105**, 4571 (1983).

[30] C. M. Che, L. G. Butler, H. B. Gray, R. M. Crooks, and W. H. Woodruff, J. Am. Chem. Soc. **105**, 5492 (1983).

[31] P. Stein, M. K. Dickson, and D. M. Roundhill, J. Am. Chem. Soc. **105**, 3489 (1983).

[32] J. R. Peterson and K. Kalyanasundaram, J. Phys. Chem. **89**, 2486 (1985).

[33] D. M. Roundhill, H. B. Gray, and C. M. Che, Acc. Chem. Res. **22**, 55 (1989).

[34] A. Filipponi, A. Di Cicco, and C. R. Natoli, Phys. Rev. B **52**, 15122 (1995).

[35] A. Bianconi, D. Jackson, and K. Monahan, Phys. Rev. B **17**, 2021 (1978).

[36] J. Goulon, P. Tola, J. C. Brochon, M. Lemonnier, J. Dexpert-Ghys, and J. Guilard, in *EXAFS & Near Edge Structure III*, edited by K. O. Hodgson, B. Hedman, and J. E. Penner-Hahn (Springer-Verlag, New York, 1984), p. 490.

[37] A. Rogalev and J. Goulon, J. Phys. IV, Colloque C2 **7**, C2 (1997).

[38] R. J. Hemley and N. W. Ashcroft, Physics Today **51-8**, 26 (1998).

[39] Y. B. Zeldovich and Y. P. Raizer, *Physics of shock waves and high temperature hydrodynamic phenomena* (Academic Press, New York, 1967), Vol. 1 and 2.

[40] R. A. Graham, *Solids under high-pressure shock compression: mechanics, physics, and chemistry* (Springer-Verlag, New York, 1993).

[41] M. P. Pasternak, G. Kh. Rozenberg, G. Yu. Machavariani, O. Naaman, R. D. Taylor, and R. Jeanloz, Phys. Rev. Lett. **82**, 4663 (1999).

[42] M. Bastea, A. C. Mitchell, and W. J. Nellis, Phys. Rev. Lett. **86**, 3108 (2001).

[43] S. Minomura and H. G. Drickamer, J. Phys. Chem. Solids **23**, 451 (1962).

[44] F. P. Bundy, J. Chem. Phys. **41**, 3809 (1964).

[45] B. Welber, C. K. Kim, M. Cardona and S. Rodriguez, Solid State Commun. **17**, 1021 (1975).

[46] M. C. Gupta and A. L. Ruoff, J. Appl. Phys. **51**, 1072 (1980).

[47] J. Z. Hu, L. D. Merkle, C. S. Menoni, and I. L. Spain, Phys. Rev. B **34**, 4679 (1986).

[48] E. V. Zarochentsev and E. P. Troitskaya, Phys. of the Solid State **44**, 1370 (2002).

[49] V. V. Struzhkin, H. K. Mao, J. Hu, M. Schwoerer-Böhning, J. Shu, R. J. Hemley, W. Sturhahn, M. Y. Hu, E. E. Alp, P. Eng, and G. Shen, Phys. Rev. Lett. **87**, 255501 (2001).

[50] E. Gregoryanz, V. V. Struzhkin, R. J. Hemley, M. I. Eremets, H. K. Mao, and Y. A. Timofeev, Phys. Rev. B **65**, 64504 (2002).

[51] J.-W. G. Bos, B. B. Van Aken, and T. T. M. Palstra, Chem. Mater. **13**, 4804 (2001).

[52] M. Citroni, M. Ceppatelli, R. Bini, and V. Schettino, High Press. Res. **22**, 507 (2002).

[53] M. I. Eremets, *High Pressure Experimental Methods* (Oxford University Press, Oxford, 1996).

[54] C. E. Wier, E. R. Lippincott, A. Valkenburg, and E. N. Bunting, Journal of Research, National Bureau of Standards **63A**, 55 (1959).

[55] A. Jayaraman, Rev. of Mod. Phys. **55**, 65 (1983).

[56] J. A. Xu, H. K. Mao, and P. M Bell, Science **232**, 1404 (1996).

[57] J. C. Chervin, B. Canny, J. M. Besson, and Ph. Pruzan, Rev. Sci. Instrum. **66**, 2595 (1995).

[58] R. Le Toullec, J. P. Pinceaux, and P. Loubeyre, High Pressure Res. **1**, 77 (1988).

[59] A. Van Valkenburg, Conference Internationale Sur-les-Hautes Pressions, LeCreusot, Saone-et-Loire, France (1965).

[60] H. K. Mao and P. M Bell, Science **200**, 1145 (1978).

[61] G. J. Piermarini, S. Block, and J. S. Barnett, J. Appl. Phys. **44**, 5377 (1973).

[62] R. A. Forman, G. J. Piermarini, J. D. Barnett, and S. Block, Science **176**, 284 (1972).

[63] J. D. Barnett, S. Block, and G. J. Piermarini, Rev. Sci. Instrum. **44**, 1 (1972).

[64] G. J. Piermarini, S. Block, J. D. Barnett, and R. A. Forman, J. Appl. Phys. **46**, 2774 (1975).

[65] G. J. Piermarini and S. Block, Rev. Sci. Instrum. **46**, 973 (1975).

[66] H. K. Mao and P. M Bell, Science **191**, 851 (1976).

[67] H. K. Mao, P. M Bell, J. W. Shaner, and D. J. Steinberg, J. Appl. Phys. **49**, 3276 (1978).

[68] A. L. Ruoff, in *High Pressure Science and Technology*, edited by K. D. Timmerhaus and M. S. Barber (Plenum, New York, 1979), Vol. 1, p. 754.

[69] H. K. Mao, in *Simple molecular systems at very high density*, edited by P. L. A. Polian and N. Boccara (Plenum Press, New York, 1989), Chap. Static compression of simple molecular systems in the megabar range, pp. 221–236.

[70] W. L. Vos and J. A. Schouten, J. Appl. Phys. **69**, 6744 (1991).

[71] A. Lacam and C. Chateau, J. Appl. Phys. **66**, 366 (1989).

[72] J. M. Leger, C. Chateau, and A. Lacam, J. Appl. Phys. **68**, 2351 (1990).

[73] F. Datchi, R. Le Toullec, and P. Loubeyre, J. Appl. Phys. **81**, 3333 (1997).

[74] R. Ingalls, G. A. Garcia, and E. A. Stern, Phys. Rev. Lett. **40**, 334 (1978).

[75] R. Ingalls, E. D. Crozier, J. E. Whitmore, A. J. Seary, and J. M. Tranquada, J. Appl. Phys. **51**, 3158 (1980).

[76] J. M. Tranquada and R. Ingalls, Phys. Rev. B **34**, 4267 (1986).

[77] J. Freund, R. Ingalls, and E. D. Crozier, Phys. Rev. B **39**, 12537 (1989).

[78] J. Freund, R. Ingalls, and E. D. Crozier, Phys. Rev. B **43**, 9894 (1991).

[79] I. E. Stekhin, A. V. Soldatov, and R. Ingalls, Physica B **208&209**, 286 (1995).

[80] A. V. Soldatov, I. E. Stekhin, and R. Ingalls, J. Phys.: Condens. Matter **8**, 7829 (1996).

[81] S. Kelly, R. Ingalls, F. Wang, B. Ravel, and D. Haskel, Phys. Rev. B **57**, 7543 (1998).

[82] A. Yoshiasa, T. Nagai, K. Murai, T. Yamanaka, O. Kamishima, and O. Shimomura, Jap. J. Appl. Phys. **37**, 728 (1998).

[83] A. Yoshiasa, K. Murai, T. Nagai, and Y. Katayama, Jap. J. Appl. Phys. I **40**, 2395 (2001).

[84] A. Yoshiasa, M. Okube, O. Ohtaka, O. Kamishima, and Y. Katayama, Jap. J. Appl. Phys. I **39**, 6747 (2000).

[85] S. De Panfilis, A. Di Cicco, A. Filipponi, and M. Minicucci, High Press. Res. **22**, 349 (2002).

[86] J. P. Itié, V. Briois, D. Martínez-García, A. Polian, and A. San-Miguel, Phys. Stat. Sol. (b) **211**, 323 (1999).

[87] E. Dartyge, C. Depautex, J. M. Dubuisson, A. Fontaine, A. Jucha, and G. Tourrillon, Nucl. Instrum. Methods **246**, 452 (1986).

[88] H. Tolentino, E. Dartyge, A. Fontaine, and G. Tourrillon, J. Appl. Phys. **21**, 15 (1988).

[89] S. Pascarelli, O. Mathon, and G. Aquilanti, submitted.

[90] J. P. Itié, A. Polian, C. Jauberthie-Carillon, E. Dartyge, A. Fontaine, H. Tolentino, and G. Tourillon, Phys. Rev. B **40**, 9709 (1989).

[91] J. M. Besson, J. P. Itié, A. Polian, G. Weill, J. L. Mansot, and J. Gonzalez, Phys. Rev. B **44**, 4214 (1991).

[92] P. Perlin, C. Jauberthie-Carillon, J. P. Itié, A. San Miguel, I. Grzegory, and A. Polian, Phys. Rev. B **45**, 83 (1992).

[93] A. G. Lyapin, V. V. Brazhkin, S. C. Bayliss, A. V. Sapelkin, J. P. Itié, A. Polian, and S. M. Clark, Phys. Rev. B **54**, 14242 (1996).

[94] A. San-Miguel, A. Polian, M. Gauthier, and J. P. Itié, Phys. Rev. B **48**, 8683 (1993).

[95] V. Briois, Ch. Brouder, Ph. Sainctavit, A. San Miguel, J. P. Itié, and A. Polian, Phys. Rev. B. **57**, 5866 (1997).

[96] J. Pellicer-Porres, A. Segura, V. Muñoz, and J. Zúñiga, J. P. Itié, A. Polian, and P. Munsch, Phys. Rev. B **65**, 12109 (2002).

[97] J. M. Besson, R. J. Nelmes, G. Hamel, J. S. Loveday, G. Weill, and S. Hull, Physica B **180/181**, 90 (1992).

[98] P. Grima, A. Polian, M. Gauthier, J. P. Itié, M. Mezouar, G. Weill, and J. M. Besson, J. Chem. Solids **56**, 525 (1995).

[99] M. Mezouar, J. M. Besson, G. Syfosse, J. P. Itié, D. Häusermann, and M. Hanfland, Phys. Status Solidi (b) **198**, 403 (1996).

[100] Y. Katayama, M. Mezouar, J. P. Itié, J. M. Besson, P. Le Fevre, and A. Di Cicco, J. Phys. IV, Colloque C2 **7**, C2 (1997).

[101] M. Okube, A. Yoshiasa, O. Ohtaka, H. Fukui, Y. Katayama, and W. Utsumi, Solid State Commun. **121**, 235 (2002).

[102] U. Buontempo, A. Filipponi, D. Martínez-García, P. Postorino, M. Mezouar, and J. P. Itié, Phys. Rev. Lett. **80**, 1912 (1998).

[103] L. Comez, A. Di Cicco, J. P. Itié, and A. Polian, Phys. Rev. B **65**, 14114 (2001).

[104] H. Hoshino, T. Miyanaga, H. Ikemoto, S. Hosokawa, and H. Endo, J. Non-Cryst. Solids **205-207**, 43 (1996).

[105] Y. Soldo, J. L. Hazermann, D. Aberdam, M. Inui, K. Tamura, D. Raoux, E. Pernot, J. F. Jal, and J. Dupuy-Philon, Phys. Rev. B **57**, 258 (1998).

[106] Y. Katayama, K. Tsuji, H. Oyanagi, and O. Shimomura, J. of Non-Cryst. Solids **232-234**, 93 (1998).

[107] Y. Katayama, O. Shimomura, and K. Tsuji, J. of Non-Cryst. Solids **250-252**, 357 (1999).

[108] Y. Katayama, J. Synchrotron Rad. **8**, 182 (2001).

[109] J. P. Itié, A. Polian, G. Calas, J. Petiau, A. Fontaine, and H. Tolentino, Phys. Rev. Lett. **63**, 398 (1989).

[110] A. Polian, J. P. Itié, E. Dartyge, A. Fontaine, and G. Tourillon, Phys. Rev. B **39**, 3369 (1989).

[111] M. Fischer, B. Bonello, J. P. Itié, A. Polian, E. Dartyge, A. Fontaine, and H. Tolentino, Phys. Rev. B **42**, 8494 (1990).

[112] M. P. Pasternak, R. D. Taylor, M. B. Kruger, R. Jeanloz, J. P. Itié, and A. Polian, Phys. Rev. B **72**, 2733 (1994).

[113] A. Di Cicco, A. Filipponi, J. P. Itié, and A. Polian , Phys. Rev. B **54**, 9086 (1996).

[114] C. B. Vanpeteghem, R. J. Nelmes, D. R. Allan, M. I. McMahon, A. V. Sapelkin, and S. C. Bayliss, Phys. Stat. Sol. (b) **223**, 405 (2001).

[115] A. V. Sapelkin, S. C. Bayliss, D. Russell, S. M. Clark, and A. Dent, J. Synchrotron Rad. **7**, 257 (2000).

[116] K. Miyauchi, M. Shojiya, Y. Kawamoto, and N. Kitamura, J. Phys. Chem. Solids **62**, 2039 (2001).

[117] K. Miyauchi, J. Qiu, M. Shojiya, Y. Kawamoto, and N. Kitamura, J. Non-Cryst. Sol. **279**, 186 (2001).

[118] Y. Katayama, H. Kanda, O. Shimomura, and H. Oyanagi, Physica B **209**, 265 (1995).

[119] Y. Katayama, K. Tsuji, O. Shimomura, and H. Oyanagi, J. Non-Cryst. Solids **205-207**, 199 (1996).

[120] B. Houser, N. Alberding, R. Ingalls, and E. D. Crozier, Phys. Rev. B **37**, 6513 (1988).

[121] J. Freund, R. Ingalls, and E. D. Crozier, J. Phys. Chem. **96**, 1087 (1990).

[122] B. Houser, R. Ingalls, and J. J. Rehr, Physica B **208&209**, 323 (1995).

[123] A. I. Frenkel, F. M. Wang, S. Kelly, R. Ingalls, D. Haskel. E. A. Stern, and Y. Yacobi, Phys. Rev. B **56**, 10869 (1997).

[124] F. M. Wang and R. Ingalls, Phys. Rev. B **57**, 5647 (1998).

[125] A. Sahiner, E. D. crozier, D. T. Jiang, and R. Ingalls, Phys. Rev. B **59**, 3902 (1999).

[126] B. Houser and R. Ingalls, Phys. Rev. B **61**, 6515 (2000).

[127] O. Ohtaka, A. Yoshiasa, H. Fukui, K.-I. Murai, M. Okube, Y. Katayama, W. Utsumi, and Y. Nishihata, J. Synchrotron Rad. **8**, 791 (2001).

[128] H. Kitagawa, M. Fujishima, Y. Kubozono, S. Emura, T. Uruga, Y. Takabayashi, and S. Fujiki, SPring-8 User Experiment Report **5**, 15 (2000A).

[129] S. Tsuduki, N. Ishimatsu, O. Shimomura, and A. Onodera, SPring-8 User Experiment Report **5**, 7 (2000A).

[130] G. Faraci, A. R. Pennisi, and J. L. Hazermann, Phys. Rev. B **56**, 12553 (1997).

[131] Y. Calzavara, V. Simonet, J. L. Hazermann, R. Argoud, O. Geaymond, and D. Raoux, J. Synchrotron Rad. **8**, 178 (2001).

[132] J. Röhler, J. P. Kappler, and G. Krill, Nucl. Instrum. Methods Phys. Res. **208**, 647 (1983).

[133] G. Kaindl, G. Schmiester, E. V. Sampathkumaran, and P. Wachter, Phys. Rev. B **38**, 10174 (1988).

[134] O. Shimomura, T. Fukamachi, T. Kawamura, S. Hasoya, S. Hunter, and A. Bienenstock, Jap. J. Appl. Phys. **17**, Suppl. 17 (1978).

[135] O. Hignette, G. Rostaing, P. Cloetens, W. Ludwig, and A. Freund, Proc. SPIE **4499**, 105 (2001).

[136] R. D. Shannon and C. T. Prewitt, J. Sol. State Chemistry **2**, 134 (1970).

[137] Y. Syono, A. Ito, S. Morimoto, T. Suzuki, T. Yagi, and S. Akimoto, Solid State Commun. **50**, 97 (1984).

[138] V. Briois, Ch. Cartier dit Moulin, Ph. Sainctavit, Ch. Brouder, and A.M. Flank, J. Am. Chem. Soc. **117**, 1019 (1995).

[139] B. S. Clausen, G. Steffesen, B. Fabius, J. Villadsen, R. Feidenhans'l, and H. Topsœ, J. Catal. **132**, 524 (1991).

[140] B. S. Clausen, K. Graback, G. Steffesen, P. L. Hansen, and H. Topsœ, Catal. Lett. **20**, 23 (1993).

[141] B. S. Clausen and H. Topsœ, Synchrotron Radiat. News **7**, 32 (1994).

[142] A. J. Dent, M. P. Wells, R. C. Farrows, C. A. Ramsdale, G. E. Derbyshire, G. N. Greaves, J. W. Couves, and J. M Thomas, Rev. Sci. Instrum. **63**, 903 (1992).

[143] A. Filipponi, M. Borowski, D. T. Bowron, S. Ansell, A. Di Cicco, S. De Panfilis and J. P. Itié, Rev. Sci. Instrum. **71**, 2422 (2000).

[144] G. Aquilanti, W. A. Crichton, and S. Pascarelli, submitted.

[145] R. J. Nelmes, M. I. McMahon, and S. A. Belmonte, Phys. Rev. Lett. **79**, 3668 (1997).

[146] S. Yu, I. L. Spain, and E. F. Skelton, Solid State Commun. **25**, 49 (1978).

[147] M. Baublitz and A. L. Ruoff, J. Appl. Phys. **53**, 6179 (1982).

[148] J. Z. Hu,D. R. Black, and I. L. Spain, Solid State Commun. **51**, 285 (1984).

[149] D. Donohue, *The structures of the Elements* (Wiley, New York, 1974).

[150] B. Brehler, Z. Krystallogr. **115**, 373 (1961).

[151] M. Sakai, N. Kuroda, and Y. Nishina, J. Phys. Soc. Jpn. **54**, 4081 (1985).

[152] H. M. Rietveld, Acta Cryst. **22**, 151 (1967).

[153] A. L Ankudinov, B. Ravel, J. J. Rehr, and S. D. Conradson, Phys. Rev. B **58**, 7565 (1998).

[154] M. Benfatto, A. Congiu-Castellano, A. Daniele, and S. Della Longa, J. Synchrotron Rad. **8**, 267 (2001).

[155] M. Benfatto and S. Della Longa, J. Synchrotron Rad. **8**, 1087 (2001).

[156] J. C. Jamieson, Science **139**, 762 (1963).

[157] J. C. Jamieson, Science **139**, 845 (1963).

[158] S. Froyen and M. L. Cohen, Phys. Rev. B **28**, 3258 (1983).

[159] S. B. Zhang and M. L. Cohen, Phys. Rev. B **35**, 7604 (1987).

[160] A. Garcia and M. L. Cohen, Phys. Rev. B **47**, 6751 (1993).

[161] A. Mujica, R. J. Needs, and A. Muñoz, Phys. Rev. B **52**, 8881 (1995).

[162] P. Rodriguez-Hernandez, A. Muñoz, and A. Mujica, Phys. Status Solidi (b) **198**, 455 (1996).

[163] A. Mujica and R. J. Needs, Phys. Rev. B **55**, 9659 (1997).

[164] R. J. Nelmes and M. I. McMahon, J. Synchrotron Rad. **1**, 69 (1994).

[165] M. I. McMahon and R. J. Nelmes, J. Phys. Chem. Solids **56**, 485 (1995).

[166] R. J. Nelmes, M. I. McMahon, N. G. Wright, D. R. Allan, H. Liu, and J. S. Loveday, J. Phys. Chem. Solids **56**, 539 (1995).

[167] R. J. Nelmes, M. I. McMahon, N. G. Wright, and D. R. Allan, J. Phys. Chem. Solids **56**, 545 (1995).

[168] M. I. McMahon and R. J. Nelmes, Phys. Status Solidi (b) **198**, 389 (1996).

[169] S. Baroni, P. Giannozzi, and A. Testa, Phys. Rev. Lett. **58**, 1861 (1987).

[170] C. A. Vanderborgh, Y. K. Vohra, and A. L. Ruoff, Phys. Rev. B **40**, 12450 (1989).

[171] G. D. Pitt and M. K. R. Vyas, J. Phys. C: Solid State Phys. **6**, 274 (1973).

[172] K. Aoki, E. Anastassakis, and M. Cardona, J. Phys. Chem. Solids **30**, 681 (1984).

[173] Y. K. Vohra, S. T. Weir, and A. L. Ruoff, Phys. Rev. B **31**, 7344 (1985).

[174] T. Soma, J. Phys. C: Solid State Phys. **11**, 2669 (1978).

[175] A. P. Hammersley, S. O. Svensson, A. Thompson, H. Graafsma, Å. Kvick, and J. P. Moy, Rev. Sci. Instrum. **66**, 2729 (1995).

[176] A. C. Larson and A. C. Von Dreele, Los Alamos National Laboratory Report **LAUR 86-748**, (1994).

[177] B. Van Laar and W. B. Yelon, J. Appl. Cryst. **17**, 47 (1984).

[178] L. W. Finger, D. E. Cox, and A. P. Jephcoat, J. Appl. Cryst. **27**, 892 (1994).

[179] R. B. Von Dreele, J. Appl. Cryst. **30**, 517 (1997).

[180] J. C. Mikkelsen, Jr., and J. B. Boyce, Phys. Rev. Lett. **49**, 1412 (1982).

[181] *Smithells Metals Reference Book*, edited by E. A. Brandes and G. B. Brook (Butterworth Heinemann, Oxford, 1999).

[182] M. A. Saitta, D. Alfè, S. De Girocoli, and S. Baroni, Phys. Rev. Lett. **78**, 4958 (1997).

[183] F. Champloy, K. Gruber, G. Jogl, and C. Kratky, J. Synchrotron Rad. **7**, 267 (2000).

[184] S. Pizzini, A. Fontaine, C. Giorgetti, E. Dartyge, J.-F. Bobo, M. Piecuch, and F. Baudelet, Phys. Rev. B **74**, 1470 (1995).

[185] J. Pellicer Porres, A. San Miguel, and A. Fontaine, J. Synchrotron Rad. **5**, 1250 (1998).

[186] A. San Miguel, M. Hagelstein, J. Borrel, G. Marot, and M. Renier, J. Synchrotron Rad. **5**, 1396 (1998).

[187] O. Mathon *et al.*, in preparation.

[188] C. Schulze, U. Lienert, M. Hanfland, M. Lorenzen, and F. Zontone, J. Synchrotron Rad. **5**, 77 (1998).

[189] E. Plouviez, DIPAC99, Chester (1999).

[190] S. Pascarelli, T. Neisius, S. De Panfilis, M. Bonfim, S. Pizzini, K. Mackay, S. David, A. Fontaine, A. San Miguel, J. P. Itié, M. Gauthier, and A. Polian, J. Synchrotron Rad. **6**, 146 (1999).

[191] S. Pascarelli, T. Neisius, and S. De Panfilis, J. Synchrotron Rad. **6**, 1044 (1999).

La Thèse s'articule en deux parties distinctes, autour de l'exploitation des caractéristiques exceptionnelles d'une ligne de lumière d'absorption X en géométrie dispersive dans un synchrotron de troisième génération. La première partie décrit la possibilité d'effectuer des études de spectroscopie d'absorption X résolues en temps avec une résolution temporelle de l'ordre de la microseconde. L'étude de la structure de l'état excité du composé $Pt_2(P_2O_5H_2)_4{}^{4-}$ a été choisi pour mettre au point cette technique. Dans la deuxième partie, l'adéquation entre les possibilités offertes par une ligne d'absorption X en dispersion d'énergie et les expériences à très hautes pressions obtenues dans les cellules à enclumes de diamants est mise en évidence. Outre les développements instrumentaux, cette dernière technique est illustrée par une étude combinée par diffraction et par absorption des rayon X du composé InAs sous pression.